An Investigation into Vacuum Drying of Spent AGR Fuel through Failed Cladding

Thomas Oliver Bainbridge

Submitted in accordance with the requirements for the degree of Master of Philosophy

The University of Leeds

School of Chemical and Process Engineering

August 2024

I confirm that the work submitted is my own, except where work which has formed part of jointly authored publications has been included. My contribution and the other authors to this work has been explicitly indicated below. I confirm that appropriate credit has been given within the thesis where reference has been made to the work of others.

Work featured in all chapters of this thesis has appeared in the following publication: *Vacuum Drying of AGR Fuel through Cracked Cladding by Thomas O. Bainbridge, Carlos de la Fontaine, Nicole Hondow and Bruce C. Hanson in the Proceedings of Waste Management 2023.* The work featured in this publication was conducted by myself with the other authors acting in a supervisory capacity.

This copy has been supplied on the understanding that it is copyright material and that no quotation from the thesis may be published without proper acknowledgement

The right of to be identified as Author of this work has been asserted by Thomas Oliver Bainbridge in accordance with the Copyright, Designs and Patents Act 1988.

© 2024 The University of Leeds and Thomas Oliver Bainbridge

Acknowledgements

The work which is completed here would not have been possible without the funding provided by TRANSCEND and the NDA.

Firstly, I would like to extend a heartfelt thank you to my supervisors, Professor Bruce Hanson, Dr Nicole Hondow and Dr Carlos De La Fontaine for their invaluable assistance and guidance throughout the course of this work. It was a pleasure to work with you and I will look back on my time in Leeds fondly. To the Nuclear Engineering Group and everyone I met at the University of Leeds, thank you for making the office and the time in Leeds enjoyable as it was and for the help and assistance given throughout the project.

The SCaPE staff have provided valuable experience and learning with Chris Bulman, Alex Holsworth, Rob Simpson and Bob Harris in particular contributing to the enjoyment of my time in Leeds but also providing expertise and training in various aspects of the work such as the microscopy suite and the assembly of pipework for the rigs.

To Alana Prior and Matthew Lovett, thank you for the immense amount of effort and hard work you put into your research projects. It was a pleasure to help supervise you for the project and I hope I was able to provide some assistance. Your contributions to this work were invaluable.

Outside of SCaPE, the staff of the mechanical and electrical workshops deserved to be recognised for the work they have performed to build and re-work components of the corrosion rigs as they corroded under testing. In particular I would like to thank Ed Woodhouse for his efforts to facilitate the work through the challenges presented by COVID and the related set-backs. Thank you also to Alice Macente who conducted the CT scans of the samples on my behalf.

Beyond the University of Leeds, Dr James Goode of UKNNL provided useful insight into the operation of the vacuum drying rig and previous corrosion work undertaken for this work.

My friends, both those I met during the course of with work at various conferences and those whom I knew prior to starting with Leeds, and my family. Thank you for your support throughout this process.

Abstract

In the United Kingdom the spent nuclear fuel produced by the Advanced Gas-cooled Reactors (AGR) is stored underwater at Sellafield awaiting a decision on the final disposal. Currently it is considered best practice to continue with the wet storage of the spent fuel however dry storage is being researched as an alternative should it be deemed necessary. There is also an acknowledgement that prior to the disposal of spent fuel in any future Geological Disposal Facility (GDF) will likely require the spent fuel to be dried. The preferred approach for conducting this drying process is called vacuum drying.

The vast majority of the spent fuel is expected to remain intact and not pose an impediment in the transition from wet interim storage to dry interim storage or disposal. However, under reactor conditions, the cladding can be rendered more vulnerable to corrosion. If the cladding was to corrode and fail then water from the pond can ingress into the fuel pin and become trapped. With the failure of the cladding providing a route for the water to enter the pin, it was suggested that this should also be a route by which the water could be removed. It is important to remove this water as the radiation from the spent fuel can cause the trapped water to undergo radiolysis which can produce hydrogen gas, hydrogen peroxide and other species which are a detriment to the safe, long-term storage or disposal of the spent fuel.

This thesis presents the results of an investigation into the vacuum drying process and the production of a model which can be used to provide insight into the conditions required for the drying. To achieve this representative cracks were required for the water and water vapour to pass through during the vacuum drying tests. An adapted form of the drop evaporation technique was used to produce these cracks in stainless steel. In addition to this work, the flow of air through various defects (pinholes, slits and cracks) was studied using the fluid flow set up with the results from these experiments presented in this thesis. Additionally a method to determine the dimensions (length and average width) of a defect is presented and the data acquired from this process used to validate the vacuum drying model.

Table of Contents

Acknowledgements 3

Abstract 4

List of Figures 9

List of Tables 18

Glossary 20

Nomenclature 22

1 Introduction 25

1.1 Management of AGR Fuel 26

1.2 Vacuum Drying of Spent Fuel 28

1.3 Dry Storage and Disposal of Spent Nuclear Fuel 29

2 Thesis Structure, Aims and Objectives 31

3 Literature Review 33

3.1 The UK's Nuclear History 33

3.2 The Advanced Gas-cooled Reactor 34

3.2.1 The Fuel Assembly 35

3.2.2 Cladding Material 35

3.2.3 Failure Mechanisms of AGR Fuel Cladding 36

3.3 Storage of Nuclear Waste 37

3.3.1 Wet Storage of Nuclear Fuel 37

3.3.2 Dry Storage of Nuclear Fuel 38

3.3.3 Geologic Disposal of Nuclear Fuel 40

3.4 Stainless Steels 41

3.4.1 Overview 41

3.4.2 Sensitisation of Stainless Steels 41

3.4.3 Radiation Induced Segregation 42

3.5 Corrosion 43

3.5.1 Overview 43

3.5.2 Forms of Corrosion 43
3.5.3 Generation of Representative Corrosion Defects 48
3.5.4 Analysis Techniques 53
3.6 Fluid Flow 58
3.6.1 Flow Regimes 59
3.6.2 Types of Flow Models 61
3.6.3 Other Approaches 67
3.7 Water in the Vacuum Drying Process 68
3.7.1 Boiling and Evaporation 68
3.8 Summary 68
4 Corroding Stainless Steel Samples 70
4.1 Experimental Work 70
4.1.1 Test Material 70
4.1.2 Drop Evaporation Technique 72
4.1.3 Potassium Tetrathionate 78
4.2 Results and Discussion 79
4.2.1 Potassium Tetrathionate 79
4.2.2 Automated Drop Evaporation Technique 80
4.2.3 Manual Drop Evaporation Technique 88
4.3 Summary 101
5 Image Analysis of Defects 104
5.1 Computational Work 104
5.1.1 Approach to Image Analysis 104
5.1.2 Determination of the Dimensions of Defects from Literature 105
5.2 Validation of the Image Analysis Code 106
5.2.1 Drawn Defects 106
5.2.2 Defects from Literature 109
5.3 Application to Corroded Samples 112

5.4 Summary 113
6 Simplified Fluid Flow Testing 114
6.1 Overview 114
6.2 Experimental Work 115
6.3 Results and Discussion 117
6.3.1 Pinhole Discs 117
6.3.2 Slit Discs 118
6.3.3 Perspex Samples 119
6.3.4 Corroded Samples 120
6.4 Summary 120
7 Vacuum Drying Through Defects 122
7.1 The Vacuum Drying Rig 122
7.1.1 First Generation Rig 122
7.1.2 Second Generation Rig 123
7.2 Methodology 125
7.2.2 Testing 127
7.2.3 Analysis 129
7.3 Results and Discussion 130
7.3.1 Large Defect Sample 130
7.3.2 Pinhole Discs 132
7.3.3 Commissioning of the Upgraded Drying Rig 137
7.3.4 Corroded Samples 141
7.4 Summary 146
8 Modelling of the Vacuum Drying Process 149
8.1 Theory 149
8.1.1 Bomelburg Fluid Flow 149
8.1.2 Taggart & Budden Fluid Flow Model 150
8.1.3 Beck Fluid Flow Model 152

8.2 Computational Work 154
8.2.1 Fluid Flow Modelling 154
8.2.2 Incorporation of Evaporation 154
8.3 Results 155
8.3.1 Comparing Flow Models 155
8.3.2 Comparison to Initial Evacuation of the Vessel 156
8.3.3 Comparison to Peaks in the Vacuum Drying Process 157
8.4 Summary 160
9 Conclusions 162
9.1 Experimental Work 162
9.1.1 Production of Defects 162
9.1.2 Vacuum Drying Process 164
9.1.3 Analysis of Defects 165
9.2 Computational Work 165
9.2.1 Determination of Defect Dimensions 165
9.2.2 Modelling Fluid Flow 165
9.3 Key Findings 166
10 Future Work 168
10.1 Production of Defects 168
10.2 Simplified Fluid Flow Testing 168
10.3 Vacuum Drying Process 168
10.4 Analysis of Defects 169
10.5 Fluid Flow Modelling 169
Publications and Conference Presentations 170
References 172

List of Figures

Figure 1: Cutaway of an AGR fuel pin showing the uranium dioxide fuel pellets inside (10). 26
Figure 2: Cutaway of an AGR element showing the graphite sleeve, stainless steel brace and fuel pins (11) 26
Figure 3: The nuclear fuel cycle. Top: closed fuel cycle. Bottom: open fuel cycle. Adapted from the World Nuclear Association (13) 26
Figure 4: Thermal Oxide Reprocessing Facility (THORP) Receipt and Storage pond hall at Sellafield which will be the final storage location of the AGR fuel pending disposal (15). 27
Figure 5: An example of failed AGR cladding. Image from (19) 28
Figure 6: Dry storage cask used for the dry storage of spent LWR fuel in the USA. Image taken from (28) 30
Figure 7: A schematic of the core of an AGR. From Ref (39). 34
Figure 8: An example of carbonaceous deposit which has built up on AGR cladding. Taken from Ref (38) 35
Figure 9: A schematic of an AGR fuel element showing the pins, stainless-steel brace and graphite sleeve (41). 35
Figure 10: A vacuum rebound test performed as part of the vacuum drying tests. 39
Figure 11: Conceptual computer generated image of a GDF. Taken from (65). 41
Figure 12: Time-Temperature-Transformation (TTT) diagram for 304 stainless steel. Taken from (72) 42
Figure 13: Types of pitting corrosion as set out by ASTM G46 (79) 44
Figure 14: A schematic of the autocatalytic cell which develops in a pit. 45
Figure 15: Schematic of crevice corrosion. Adapted from Ref (47). 45
Figure 16: The galvanic series. Taken from Ref (84) 46
Figure 17: Conditions required for stress corrosion cracking to occur. 46
Figure 18: A vulnerable grain boundary. Adapted from Ref (92). 48
Figure 19: The immersion test set up used by Drugli and Steinsmo (94). 49
Figure 20: The modified four-point bend test rig used by Pereira et al to induce stress on the samples. 50
Figure 21: The typical surface temperature of a sample undergoing the drop evaporation technique. Adapted for clarity from (104) 52
Figure 22: Schematic showing different planes used to create a z-stack. 55

Figure 23: Schematic showing the difference between where backscatter and secondary electrons are produced during imaging by an SEM. Simplified from (108).....56
Figure 24: The difference between backscattered electrons and secondary electrons. Image from (109).....56
Figure 25: An illustration of the interaction between incident electrons and two materials of different density showing how the more dense material scatters a higher proportion of electrons back at the detector. Simplified and adapted from (108).....57
Figure 26: A illustration showing how an x-ray is emitted from an atom to then be detected by EDS.....58
Figure 27: Schematic showing the principles behind the x-ray computed tomography set up (114).....58
Figure 28: Laminar flow in a pipe shown schematically. Image from Bronkhorst (118). 59
Figure 29: Turbulent flow in a pipe shown schematically. Image from Bronkhorst (118). 60
Figure 30: Transition regime flow shown schematically highlighting the changes in direction that occur in this regime while the overall flow remains fairly linear. 60
Figure 31: Different multiphase flow types. Adapted from (122).....61
Figure 32: Key parameters of the crack shown in isometric and top down cross sectional views. 61
Figure 33: Schematic of a sharp edged orifice in a pipe.....62
Figure 34: Schematic of the set-up used by Pereira et al (143). Adapted from the reference for clarity.....72
Figure 35: Schematic of the rig used for the drop evaporation work conducted for this thesis.....73
Figure 36: A photograph of the finished drop evaporation rig used for this work.....73
Figure 37: Diagram of the set up used to heat the sample for the drop evaporation tests conducted in the rig.....74
Figure 38: The build-up of salt on and around the rig after during operation of the DET rig after 7 days, 14 days and 21 days.....76
Figure 39: Corrosion of one of the pylons found on the first generation drop evaporation rig. Acquired on the stereomicroscope using the 1.25x lens for a total magnification of 12.5x.....76
Figure 40: A portion of the unknown brown sludge which formed during one of the drop evaporation tests conducted using the automated rigs.....77

Figure 41: An image of a sample undergoing corrosion testing using the constantly wetted approach. 78
Figure 42: One of the falcon tubes containing a sample of sensitised 304 stainless steel being exposed to the 0.1 M potassium tetrathionate which has been acidified to pH 2 with the addition of sulphuric acid. 79
Figure 43: Corrosion damage to the samples of mild steel exposed to the 0.1 M potassium tetrathionate which had been acidified to pH 2 with sulfuric acid. a) 24 hours b) 72 hours c) 144 hours d) 192 hours e) 240 hours. 80
Figure 44: Samples of 304 stainless steel thermally treated at 650C for 48 hours and left to furnace cool. These samples were also hand sanded to remove the oxide layer that had formed prior to immersion in the acidified potassium tetrathionate for: a) 72 hours b) 144 hours c) 192 hours d) 240 hours 80
Figure 45: Sample C1 which was held under stressed conditions for 168 hours with 35 g/L NaCl dripped onto the sample from 09:00 to 17:00 for a week producing a 50 µm diameter pit shown here. 82
Figure 46: a 3D view of the pits generated in sample S1 found in the region around the loading point. The data was gathered using the 50x magnification, 0.6 lens on the CLSM. 83
Figure 47: A 2D topographic view of the same region shown in Figure 46. 83
Figure 48: A z-stack of the sample P1showing the edge of one of the centre punch marks found near the loading points. Taken using the 10x magnification 0.4 lens on the CLSM. 84
Figure 49: The topographic scan and depth profile of the corrosion pits which formed on the edge of sample P1. 84
Figure 50: A series of pictures showing the build-up of NaCl on the rig over the course of an experiment after: a) 7 days b) 14 days and c) 21 days. 84
Figure 51: EDS analysis of the mystery material showing the distribution of the main elements detected. 85
Figure 52: Sample ID:1 after gentle cleaning in deionised water. The significant corrosion damage is visible with a crack circled. 86
Figure 53: Images of cracks near the failure surface of sample ID:1 showing the corrosion damage. Taken at 10x magnification on the Olympus BX51 microscope. 87
Figure 54: SEM images of microcracks detected on the sample 1 after nine days exposure to 35g/L MgCl2. a) Crack from the surface through the depth. b) Trans-

granular crack from the failure edge. c) A crack initiated in a local corrosion region. d) Part of a crack network from the surface through the material. 87
Figure 55: Sample ID:2a showing the pit which had developed on the surface after 1080 hours of exposure and which had not been observed after observation at 672 hours. This image was taken at the end of the test (1776 hours) using the 10x magnification, 0.4 lens on the CLSM. The right hand image was acquired using the same lens on the CLSM to obtain a topographic profile which was then levelled against the surface of the sample. 91
Figure 56: SEM image of the pit shown in Figure 55. (L) An image taken using a 15kV accelerating voltage using backscatter electron mode and under 200 times magnification. (R) The same location imaged using the secondary electron mode but with the same accelerating voltage and magnification. 91
Figure 57: The CT scan results of the pit imaged by CLSM (Figure 55) and SEM (Figure 56) showing two slices. A) shows the pit splitting into two lowest points with cracks propagating from each. B) shows a longer crack propagating from a shallower location on the pit. 92
Figure 58: Sample ID:5a after 1344 hours of corrosion without interruption for examination. (L) Optical image taken using the 20x 0.4 lens on the CLSM. (R) The topographic scan of the same area also using the 20x 0.4 lens. 93
Figure 59: The extracted topographic profile pass through the lowest point measured by the CLSM scan of a pit on sample ID:5a. 93
Figure 60: Corrosion located in and around the site where a Dremel was used to remove material. This image shows sample ID:3a after the further 1344 hours of corrosion and is a composite, tiled image taken using the CLSM. 96
Figure 61: Images taken of four thinned regions of sample ID:11 on both the side where the Dremel was applied and the reverse location where initial corrosion was observed. 97
Figure 62: A CT image of disc one in the "upper" portion of the disc. a) The plan view. b) A slice looking along the red line in (a). c) A slice looking along the blue line in (a). 98
Figure 63: A CT image of disc one in the "central" portion of the disc. a) The plan view. b) A slice looking along the red line in (a). c) A slice looking along the blue line in (a). 98

Figure 64: A CT image of disc one in the "lower" portion of the disc. a) The plan view. b) A slice looking along the red line in (a). c) A slice looking along the blue line in (a). 98
Figure 65: A CT image of disc two in the "upper" portion of the disc. a) The plan view. b) A slice looking along the red line in (a). c) A slice looking along the blue line in (a). 99
Figure 66: A CT image of disc two in the "central" portion of the disc. a) The plan view. b) A slice looking along the red line in (a). c) A slice looking along the blue line in (a). 99
Figure 67: A CT image of disc two in the "lower" portion of the disc. a) The plan view. b) A slice looking along the red line in (a). c) A slice looking along the blue line in (a). 99
Figure 68: A CT image of disc three in the "upper" portion of the disc. a) The plan view. b) A slice looking along the red line in (a). c) A slice looking along the blue line in (a). 100
Figure 69: A CT image of disc three in the "central" portion of the disc. a) The plan view. b) A slice looking along the red line in (a). c) A slice looking along the blue line in (a). 100
Figure 70: A CT image of disc three in the "lower" portion of the disc. a) The plan view. b) A slice looking along the red line in (a). c) A slice looking along the blue line in (a). 100
Figure 71: A CT image of disc four in the "upper" portion of the disc. a) The plan view. b) A slice looking along the red line in (a). c) A slice looking along the blue line in (a). 101
Figure 72: A CT image of disc four in the "central" portion of the disc. a) The plan view. b) A slice looking along the red line in (a). c) A slice looking along the blue line in (a). 101
Figure 73: A CT image of disc four in the "lower" portion of the disc. a) The plan view. b) A slice looking along the red line in (a). c) A slice looking along the blue line in (a). 101
Figure 74: A crack caused by PCMI. Image taken from (38). 103
Figure 75: (L) The original image of a crack taken from Ref (15) (R) The cleaned up version of the crack used in the image analysis code..... 104
Figure 76: (L) The original image of the defect to be analysed. (R) The skeleton produced by the MATLAB code overlayed with the original image. 104

Figure 77: The skeleton of the channel overlayed on an image of the channel with the coordinate locations highlighted. 105
Figure 78: A diagram showing how the length of the cracks in literature was calculated. 106
Figure 79: An example of a crack from literature where widths are provided. Image of the defect taken from Ref (145). 106
Figure 80: Attempted analysis of the produced cracks showing the skeleton produced by the code overlayed on the original image provided. 112
Figure 81: A schematic for the simplified fluid flow rig. 114
Figure 82: Examples of (L) a pinhole disc test piece and (R) a slit test piece. Images from (154) and (155) respectively. 115
Figure 83: The components in the order of assembly to hold a sample, in this case a corroded disc, in place for both the simplified fluid flow rig and later the vacuum drying rig. Left to right: one half of a Swagelok fitting, a Swagelok ferrule with tubing to form a seal, the first O-ring, the sample to be tested and the final O-ring to seal against the base of the fitting. 115
Figure 84: The assembled fitting using the components shown in Figure 82. A similar assembly was used in the vacuum drying rig. 116
Figure 85: A photograph of the simplified fluid flow testing rig showing the sample mounting location, pressure chamber and vacuum pump. 117
Figure 86: The time taken for the sample tank to reach atmospheric pressure from a starting pressure of approximately 0.1 BarA through discs featuring various sizes of pinholes. 118
Figure 87: Average results from three tests of each of the slit discs in the simplified fluid flow rig. 118
Figure 88: A representation of how the Perspex strips were cracked. 119
Figure 89: A stereomicroscope image of one of the Perspex samples produced 119
Figure 90: The results of the return to atmospheric tests undertaken using the discs featuring the corroded crack discs. 120
Figure 91: Schematic of the vacuum drying rig. 123
Figure 92: The first generation vacuum drying rig built by J. Goode. 123
Figure 93: A schematic of the second generation of vacuum drying rig used for this work. 124
Figure 94: The second generation of the vacuum drying rig featuring the upgrades made by M. Jackson and M. Lovett with consultation from myself. 124

Figure 95: The first generation of loose sample constructed by M. Jackson featuring a 227 µm diameter pinhole drilled into a section of AGR cladding. 126
Figure 96: The second version of the loose sample design used to hold the pinhole discs purchased from Edmund Optics featuring an araldite seal. 126
Figure 97: An example plot from a vacuum drying test with regions highlighted for discussion. 128
Figure 98: A test conducted at 60°C using the large defect sample (shown in Figure 94) using 7g of water and the first generation drying rig. 131
Figure 99: A cropped section of Figure 97 showing the period from 50 minutes to 80 minutes in detail. 131
Figure 100: A graph showing the pressure, dew point, sample temperature and flow rate for a test conducted using the first generation of pinhole disc samples. The 1 micron diameter pinhole disc was used with the vessel temperature set to 60°C 132
Figure 101: A graph of the pressure, dew point, temperature and flow rate of a test conducted using the second generation of pinhole disc samples. The 10 micron diameter pinhole disc was used with the vessel temperature set to 60°C 133
Figure 102: A graph of the pressure, dew point, temperature and flow rate of a test conducted using the second generation of pinhole disc samples. The 20 micron diameter pinhole disc was used with the vessel temperature set to 60°C 133
Figure 103: A graph of the pressure, dew point, temperature and flow rate of a test conducted using the second generation of pinhole disc samples. The 50 micron diameter pinhole disc was used with the vessel temperature set to 60°C 134
Figure 104: A graph of the pressure, dew point, temperature and flow rate of a test conducted using the second generation of pinhole disc samples. The 100 micron diameter pinhole disc was used with the vessel temperature set to 50°C 134
Figure 105: A graph of the pressure, dew point, temperature and flow rate of a test conducted using the second generation of pinhole disc samples. The 100 micron diameter pinhole disc was used with the vessel temperature set to 70°C 134
Figure 106: A graph of the pressure, dew point, temperature and flow rate of a test conducted using the second generation of pinhole disc samples. The 100 micron diameter pinhole disc was used with the vessel temperature set to 80°C. The first run with these conditions. 135
Figure 107: A graph of the pressure, dew point, temperature and flow rate of a test conducted using the second generation of pinhole disc samples. The 100 micron

diameter pinhole disc was used with the vessel temperature set to 80°C. The second run with these conditions. 135
Figure 108: Schematic of two of the different sample designs used. (L) The large defect sample shown in Figure 94 with the defect located on the side of the tube. (R) The sample design used for the pinhole discs. 136
Figure 109: A scatter plot showing the mass of water remaining in a second generation pinhole disc sample over the duration of a test. This test was undertaken using the 20 µm diameter pinhole and 2 g of water. 137
Figure 110: Testing of a sample loaded with 2g of water left to rest loose in the bottom of the vessel. The vessel was set to 100 °C. The pressure recorded in this test is the pressure in the vessel. 138
Figure 111: A test of the 227 micron diameter defect sample attached to the lid of the vessel in the style that would be used going forward with the rig. The vessel was set to 80 °C. 139
Figure 112: A bleed test conducted by M. Lovett. The vessel temperature is set at 100 °C and 2 g of water had been loaded into the sample. The grey shaded region denotes the period where the leak was introduced. 140
Figure 113: A multi-bleed test undertaken with the vessel temperature set to 100 °C and 2 g of water loaded into the sample. The grey shaded regions denote the periods where the bleed leak of air was in progress. 140
Figure 114: A schematic showing the set-up of the sample attached to the lid of the vessel. The sample to be tested is located in the right hand portion of the T-junction. 141
Figure 115: A vacuum drying test conducted with 2 g of water, disc 1 and the sample attached to the vessel lid. The vessel was set to a temperature of 70°C. 142
Figure 116: A vacuum drying test conducted with 2 g of water, disc 1 and the sample attached to the vessel lid. The vessel was set to a temperature of 120°C. 143
Figure 117: A vacuum drying test conducted with 2 g of water, disc 2 and the sample attached to the vessel lid. The vessel was set to a temperature of 70°C. 143
Figure 118: A vacuum drying test conducted with 2 g of water, disc 2 and the sample attached to the vessel lid. The vessel was set to a temperature of 120°C. 144
Figure 119: A vacuum drying test conducted with 2 g of water, disc 3 and the sample attached to the vessel lid. The vessel was set to a temperature of 70°C. 145
Figure 120: A vacuum drying test conducted with 2 g of water, disc 3 and the sample attached to the vessel lid. The vessel was set to a temperature of 120°C. 145

Figure 121: A vacuum drying test conducted with 2 g of water, disc 4 and the sample attached to the vessel lid. The vessel was set to a temperature of 70°C. 146
Figure 122: A vacuum drying test conducted with 2 g of water, disc 4 and the sample attached to the vessel lid. The vessel was set to a temperature of 120°C. 146
Figure 123: Simplified diagram showing the parameters for the model presented by Taggart and Budden. Simplified to show the variables used in the work. Original graphic from (136). 151
Figure 124: An schematic of a crack showing how the number of turns is determined. 151
Figure 125: A schematic of an idealised section of crack showing the parameters. Adapted from (135)..... 152
Figure 126: Comparison of the three main models with the experimental data gathered. In addition the average of the models proposed by Beck et al. and Taggart & Budden models is presented. 155
Figure 127: A plot of the computationally determined pressure against the experimentally determined pressure for the two different models and the average of both models. 156
Figure 128: Comparison between the average Taggart & Budden model and the Beck et al model, compared pressure recorded during the initial pump down at 40°C. 156
Figure 129: Comparison between the average Taggart & Budden model and the Beck et al model, compared pressure recorded during the initial pump down at 50°C. 157
Figure 130: A representation of an evacuation trace and how the conditions and sections of graph were chosen for analysis in this section..... 158
Figure 131: Comparison between the Beck, Taggart & Budden and the average approaches along with the evacuation from a peak in the pressure during a test of a 10 micron pinhole at 60°C. 158
Figure 132: Comparison between the Beck, Taggart & Budden and the average approaches along with the evacuation from a peak in the pressure during a test of a 20 micron pinhole at 60°C. 159
Figure 133: Comparison between the Beck, Taggart & Budden and the average approaches along with the evacuation from a peak in the pressure during a test of disc 2 at 120°C..... 159
Figure 134: Comparison between the Beck, Taggart & Budden and the average approaches along with the evacuation from a peak in the pressure during a test of disc 3 at 120°C..... 160

List of Tables

Table 1: Composition of common stainless steels and AGR cladding (20/25/Nb). Compositions taken from (44; 45; 46). 36
Table 2: The ISO standard for the drop evaporation technique and the adaptations made by Hinds and Turnbull 51
Table 3: Overview of techniques used to analyse corrosion test samples. 53
Table 4:The Reynolds number and range for the different flow regimes (117). 59
Table 5: Refence compositions of 304 and 316 stainless steel taken from Thyssenkrupp Materials along with the composition of supposed 304 stainless steel purchased from RS-Pro (44) (45). 71
Table 6: Summary of experimental conditions for the NaCl tests using the automated rig. 81
Table 7: Summary of the experimental conditions for the MgCl2 tests conducted on the automated rig 85
Table 8: Summary of experimental conditions for the $MgCl_2$ tests corroded using the constantly wetted method 89
Table 9: Summary of the experimental conditions for the sample of 304 stainless steel in the drying cabinet set up. 94
Table 10: Conditions experienced by the samples post thinning with a Dremel. 95
Table 11: The results from testing the image analysis code against drawn straight channels where the length was varied. 107
Table 12: The results from testing the image analysis code for drawn cracks where the width was varied. 108
Table 13: Results from testing the image analysis code against more complex drawn defect pathways. 109
Table 14: Results from testing the image analysis code against cracks presented in literature. 110
Table 15: Length and average width of the defects in Disc 1 as determined using a pixel/mm scale and the image analysis code 112
Table 16: A summary of the tests undertaken using the large defect sample (Figure 94) detailing the temperature of the test, the mass of water added, the duration of the test and the drying rate determined 131
Table 17: Summary of tests undertaken to commission the upgraded drying rig. Tests designed and undertaken in conjunction with M. Lovett (157). 138

Table 18: Friction factor coefficients. Information contained in this table was sourced from (136) 152

Glossary

Term	Definition
#P	Number of punch marks
AGR	Advanced Gas-cooled Reactor
AISI	American Iron and Steel Institute
AR	As Received
ASTM	American Society for Testing and Materials
BEPO	British Experimental Pile Operation
BWR	Boiling Water Reactor
CANDU	CANada Deuterium Uranium
CFD	Computational Flow Dynamics
CLSM	Confocal Laser Scanning Microscope
COD	Crack Opening Displacement
CT	Computed Tomography
DET	Drop Evaporation Technique
EDF	Électricité de France
EDS	Energy Dispersive X-ray Spectroscopy
EDX	Energy Dispersive X-ray
ET	Etched
FGD	Flowed Gas Drying
GDF	Geologic Disposal Facility
GLEEP	Graphite Low Energy Experimental Pile
HS	Hand Sanded
IAEA	International Atomic Energy Authority
IGA	InterGranular Attack
IGC	InterGranular Corrosion
IGSCC	InterGranular Stress Corrosion Cracking
ISO	International Organization for Standardization
LBB	Leak Before Break
LWR	Light Water Reactor
ND	Not Detected
NDA	Nuclear Decommissioning Authority
NRC	Nuclear Regulatory Commission
ODE	Ordinary Differential Equation

ONR	Office for Nuclear Regulation
PBI	Pellet Brace Interaction
PCMI	Pellet Clad Mechanical Interaction
PWR	Pressurised Water Reactor
RIS	Radiation Induced Segregation
SB	Shot Blasted
SCC	Stress Corrosion Cracking
SEM	Scanning Electron Microscope
THORP	THermal Oxide Reprocessing Plant
UK	United Kingdom
USA	United States of America
XCT	X-ray Computed Tomography

Nomenclature

Symbol	Definition	Unit
A	Area	m^2
C	Constant	
D	Hydraulic diameter	m
E	Young's modulus	$N\ m^{-2}$
F	Fraction of molecules assumed absorbed and re-emitted diffusely	
G	Gap between the tips of the crack surface	
K	Knudsen number	
L	Material thickness	m
M	Mach number	
N	Number of turns	
P	Pressure	Pa
Q	Flow rate	
R	Ideal gas constant	$J\ K^{-1}\ mol^{-1}$
T	Temperature	K
V	Volume	m^3
a	Constant	
b	Constant	
c	Constant	
f	Friction factor	
g	Gravity	$m\ s^{-2}$
h	Crack height	m
k	Conductivity	
l	Crack length	m
ℓ	Length of arc of flow around a crack tip	
m	Mass	kg
n	Moles	
r	Crack radius	m
t	Time	S
v	Velocity	$m\ s^{-1}$
w	Crack width	m
z	Crack depth	m

α	Area correction factor	
β	Diameter ratio	
Γ	Half angle of curvature	
γ	Ratio of specific heats	
ε	Expansion factor	
θ	Average flow direction	
λ	Mean free path	m
μ	Viscosity	N s m^{-2}
Ξ	Perpendicular height of the grain	
π	Pi	
ρ	Density	Kg m^{-3}
σ	Stress	N m^{-1}
ψ	Complete momentum accommodation coefficient	
R_a	Roughness	m
c_p	Specific heat at constant pressure	J kg^{-1} k^{-1}
c_v	Specific heat at constant volume	J kg^{-1} k^{-1}
h_{fg}	Latent heat of vaporisation	J kg^{-1}
C_d	Discharge coefficient	
C_f	Flow coefficient	
S_y	Yield strength	Pa
M_w	Molecular weight	
COD	Crack Opening Displacement	

Subscripts

Symbol	**Definition**	**Unit**
eff	Effective	
exp	Losses due to fluid expansion	
m	Mass	
v	Volumetric	
ev	Evaporated	
ms	Mole/s flow rate	
max	Maximum	
hoop	Hoop stress	
o	Outlet	

i	Inlet
inertial	Losses due to inertial forces
1	Initial
s	Stagnation
fan	Fanning
F	Fluid
visc	Losses due to fluid viscosity

Other

Symbol	**Definition**	**Unit**
$\overline{}$	Average	

1 Introduction

In 1942 at the University of Chicago, the Chicago Pile 1 reactor achieved the first sustained nuclear fission reaction with the technology then being used to inform the design of larger reactors at Hanford and Oak Ridge. These reactors would be utilised by the Manhattan Project in order to supply the uranium and plutonium necessary for the atomic bombs (1). After the second world war, while the production of nuclear weapons was still a priority, the possibility of using the fission process for more peaceful purposes was investigated with Eisenhower saying in his famous "Atoms for Peace" speech in 1953 that the technology behind the creation of nuclear weapons needs to be "*put into the hands of those who will know how to strip its military casing and adapt it to the arts of peace*" such as "*to provide abundant electrical energy"* (2).

In 1956, the world's first commercial nuclear reactor station – Calder Hall – began supplying electricity to the public (3). Calder Hall and the rest of the Magnox fleet built upon the experience gained from operating the Windscale Pile reactors. In the pile reactors, natural uranium was encased in an aluminium cladding which was then inserted into a graphite moderator with the reactor being cooled by drawing in air and passing it over the fuel (4; 5). For the Magnox reactor, natural uranium was still used however the aluminium cladding had been swapped out for a magnesium-aluminium non-oxidising alloy which is where the name Magnox arose from (6). These reactors operated at higher temperatures than the Windscale Piles which necessitated the change in cladding material. In addition, to limit the radioactive material being released into the atmosphere a closed system was operated and the less corrosive CO_2 was used to cool the core and heat the secondary circuit which produced steam. However, despite these changes, graphite was still used as the moderator.

While most other countries chose to follow the Light Water Reactor (LWR) design philosophy, the United Kingdom opted to pursue the gas cooled reactors further with the Advanced Gas-cooled Reactors (AGR). Following further refinement of the Magnox design and now having the ability to enrich uranium, the fuel was changed to a uranium dioxide enriched to up to 3.5% and formed into pellets (7). 64 of these pellets are then stacked to form a fuel pin clad in 20-25-Nb stainless steel , as shown in Figure 1 (8; 9). 36 of these pins are then placed into a stainless steel brace and a graphite sleeve which acts as the moderator in the reactor – the full fuel element arrangement is shown in Figure 2.

Figure 1: Cutaway of an AGR fuel pin showing the uranium dioxide fuel pellets inside (10).

Figure 2: Cutaway of an AGR element showing the graphite sleeve, stainless steel brace and fuel pins (11).

1.1 Management of AGR Fuel

In 2012, the decision was taken that would see the UK cease the reprocessing of spent nuclear fuel once the contracted quantities had been processed (12). For the AGR fuel, this was achieved in 2018. As a result of this, the UK moved from a closed fuel cycle to an open fuel cycle as far as the AGR fuel is concerned, as shown in Figure 3.

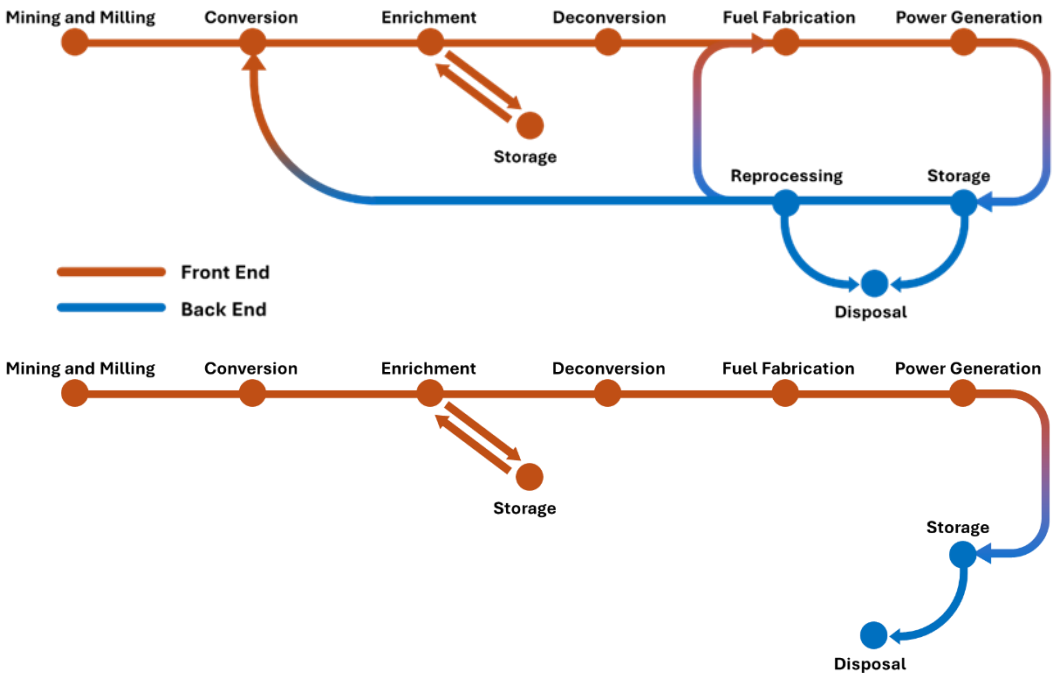

Figure 3: The nuclear fuel cycle. Top: closed fuel cycle. Bottom: open fuel cycle. Adapted from the World Nuclear Association (13).

This change in strategy has necessitated a change in strategy. Instead of storing the fuel for a relatively short period of time prior to reprocessing, the spent fuel will now need to be stored until the high heat generating portion of a Geological Disposal

Facility (GDF) is ready to receive the fuel should it be classified as a waste. This is expected to be in 2075 at the earliest (14). The current storage strategy is to continue with the wet interim storage of the spent fuel in the ponds at Sellafield (such as is shown in Figure 4) owing to the decades of experience gathered using this approach.

Figure 4: Thermal Oxide Reprocessing Facility (THORP) Receipt and Storage pond hall at Sellafield which will be the final storage location of the AGR fuel pending disposal (15).

To help ensure that the cladding does not fail during the interim storage at Sellafield, the pond chemistry is carefully controlled and dosed to pH 11.4 with sodium hydroxide (also referred to as caustic) to inhibit corrosion (16). However, under reactor conditions the cladding can become sensitised rendering it more vulnerable to corrosion as a result of the thermal and radiological conditions (17). Historically, the failures observed in AGR fuel was attributed to intergranular stress corrosion cracking and detected due to the release of radionuclides into the pond (18). An example of a failure in AGR cladding is shown in Figure 5.

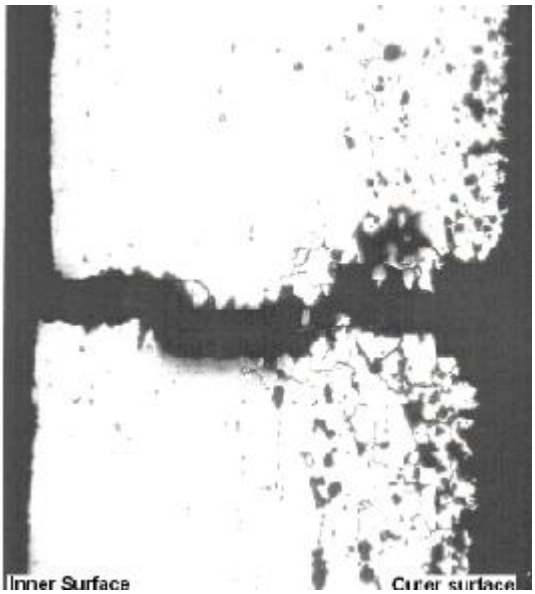

Figure 5: An example of failed AGR cladding. Image from (19)

With the introduction of the caustic dosing to the ponds, it appears to have successfully inhibited any corrosion occurring to the cladding, however, there is a concern that some of the pins may already have micro cracks which are too narrow and tortuous for a sufficiently high release of caesium to occur and allow for detection. Due to the expected quantity of pins in wet interim storage it is considered likely that the proportion of said pins will become flooded.

1.2 Vacuum Drying of Spent Fuel

While the preferred strategy is to continue with the wet interim storage of the spent fuel, it is recognised that a fall back option is required the potential for dry storage should be investigated (20). In addition, regardless of whether dry interim storage is required the Nuclear Decommissioning Authority's (NDA) strategic decision 10 sets out the expectation that the fuel will need to be dried prior to disposal in a GDF (21).

One approach being considered is vacuum drying. In this approach, the material to be dried is placed into a vacuum chamber which is then sealed. By lowering the pressure in the chamber and therefore the water vapour concentration, a vapour pressure gradient is formed causing water to evaporate (22). Vacuum drying in itself is not a new process with the technique being used to remove moisture from products that could degrade or be destroyed should thermal treatment be used such as chemicals, pharmaceuticals or foods (23). Even among the nuclear industry, vacuum drying has been considered a viable means of removing water prior to the fuel being placed into dry storage casks (24). However, this has been primarily conducted on and researched for LWR fuels clad

in zircaloy (25). In contrast the AGR fuel is clad in stainless steel and therefore it is understood that the existing dry storage methods would not be directly applicable for this fuel.

At Sellafield, steps are taken to prevent failed fuel arriving from the reactor stations coming into contact with the pond water. Any fuel which fails in reactor is first sent to hot cell facilities for dry packaging prior to being transferred to Sellafield for pond storage (26). Meanwhile, as mentioned in section 1.1, the pond water chemistry is carefully controlled via dosing with sodium hydroxide to pH 11.4 in order to inhibit the corrosion of the stainless steel (16). Nevertheless, there is a concern that over the extended duration of the interim storage, some of the cladding may fail and allow water to ingress and come into contact with the fuel pellets. Should this water not be removed prior to disposal then the water may undergo radiolysis and produce hydrogen and hydrogen peroxide which is detrimental to the conditions in the store. This is discussed in greater detail in section 1.3.

1.3 Dry Storage and Disposal of Spent Nuclear Fuel

The primary purpose of either wet or dry storage and of any disposal route developed is to maintain the containment barriers that prevent radionuclides from escaping into the environment. For AGR fuel, the primary containment is considered to be the fuel cladding. While in a wet storage environment, corrosion can be controlled by careful management of the water chemistry this cannot be maintained indefinitely (18). Eventually either the pond will reach capacity or the facility will age to the point at which a replacement would be required. In addition due to the need to monitor and control the pond chemistry adds significant cost to the operation.

The United States' reprocessing operations ceased by 1977 as a result of a non-proliferation policy implemented which resulted in all spent fuel being wet stored (27). In the 1980's these stores were beginning to reach capacity and even to this day, only two possible options are permitted to expand storage (28):

1) Re-racking which involves reducing the spacing between storage containers
2) Consolidation which is where the spent fuel is repacked more densely.

This finite expansion prompted utility companies to turn to the dry storage option. Once the fuel has cooled and the radioactivity has decayed sufficiently, it is dried and placed into a metal cylinder which is then enclosed within a metal or concrete outer shell such as those shown in Figure 6. With the success of this approach, other countries around

the world have deployed their own dry storage though it should be noted that none operate the AGR reactors or with stainless steel cladding.

Figure 6: Dry storage cask used for the dry storage of spent LWR fuel in the USA. Image taken from (28).

It is well understood that water, in the presence of radiation, is likely to undergo radiolysis which can lead to the production of both hydrogen and hydrogen peroxide. In a sealed environment such as a dry storage cask or disposal facility there is no means to remove these species from the container. Hydrogen presents a flammability and explosive risk while it is acknowledged that the other radiolysis products such as hydrogen peroxide act to increase the rate of corrosion (29). Further corrosion of the stainless steel cladding of the AGR fuel is obviously undesirable as this could lead to further radionuclide release. Therefore, the removal of the water from the system is crucial for the long term, safe storage or disposal.

2 Thesis Structure, Aims and Objectives

This work aimed to continue to develop the understanding of the behaviour of failed spent AGR fuel during the vacuum drying process, building on work conducted previously. Additionally it aimed to develop a model which could be used to help inform the drying process by providing a prediction of the drying time required for a given defect size and water mass. In order to achieve these aims several strands were pursued. One side focused on the experimental aspects to the work while the other was focused around the computational side of the work.

On the experimental side there were three key objectives:

1. Corrode stainless steel to produce cracks similar to those which are expected in failed AGR cladding.
2. Conduct vacuum drying trials to assess the drying though narrow tortuous cracks in stainless steel.
3. Determine the impact of the narrow tortuous cracks on the flow of fluid though said cracks.

For the computational work, at the beginning of the project, a further three objectives were set out:

1. Model the flow of fluid through a narrow tortuous crack.
2. Model the evaporation of water under low pressure / near vacuum conditions.
3. Combine the two codes to produce a model which could provide insight into the drying time required and validate it against the experimental results.

It should be noted that this project was conducted during and after the COVID pandemic which had a significant impact on the work conducted.

The following section of this report focuses on providing the reader with a review of the relevant literature covering the main concepts of which this work was based on. It focuses on the AGR fuel and storage conditions before covering the material properties and corrosion of stainless steels before turning attention towards the fluid flow and the evaporation of water. Finally the literature review covers the existing state of vacuum drying. The subsequent chapters present the various strands of work which were undertaken during this project. The order of these sections is intended to guide the reader though the work, not in chronological order but instead in the order which provides an understanding as to how the model was built up over the course of this

work. Finally, the entirety of the project is considered, presenting a review of the key findings from this work as well as evaluating the progress made towards the aim and outlining the future work which would need to be undertaken.

3 Literature Review

This chapter sets out a background to the work which has been conducted as part of this project. It initially covers the UK's nuclear history with particular focus given to the AGR programme along with the fuel design in addition to the storage and disposal environments and considerations. A review of stainless steel and relevant corrosion mechanisms is also contained within this chapter along with a discussion about the flow of fluids through restrictions and the evaporation of water at low pressure. The chapter is rounded out by a description of the current state of vacuum drying for both AGR fuel as well as the developments made internationally as a means of drying other fuel types.

3.1 The UK's Nuclear History

Following the second world war and the Manhattan Project, the UK 's nuclear industry was focused on the development of atomic weapons. The first reactors in the UK were constructed at Harwell – Graphite Low Energy Experimental Pile (GLEEP) and British Experimental Pile 0 (BEP0) which commenced operations in 1947 and 1948 respectively (30). The experienced gained from these reactors was used to develop the Windscale Piles which were naturally enriched uranium fuelled, graphite moderated and air cooled reactors. It was realised that the heat removed from the reactor could be harnessed to generate electricity and this led to the creation of the world's first commercial reactor at Calder Hall. Several refinements to the design of the Windscale Piles were implemented, such as the introduction of the closed cycle for the coolant to reduce the release of radioactivity into the atmosphere as well as switching to a carbon dioxide coolant due to its reduced corrosivity (25). While natural uranium was still used in these reactors, the aluminium cladding used for the Windscale Piles was replaced with a magnesium-aluminium alloy to improve the neutron cross section.

For the second generation of nuclear reactors, while most of the world decided to concentrate on water cooled reactor designs, the UK's attention remained fixed on gas cooled systems (31). The prototype AGR reactor at Windscale (now Sellafield), also referred to as the WAGR, became operational in 1962, with the first of the commercial reactors beginning operation in 1976 (32; 33).

3.2 The Advanced Gas-cooled Reactor

As mentioned in section 3.1, the AGR reactors represent the UK's second generation of commercial nuclear power plants. The first of these reactors, Dungeness B, began commercial operation in 1983 and the final reactor station, Torness, coming online in 1989 (34). In 2021, Dungeness B became the first of the AGR reactors to enter defueling and it has since been joined by Hunterston B in 2022 (35; 36). Due to the contracting process there is not a "typical" AGR reactor as each one is slightly different such as Dungeness B where a fuel stringer is comprised of seven fuel elements compared to every other reactor where eight is the norm (37; 38). A schematic showing the design of the AGR reactor is shown in Figure 7.

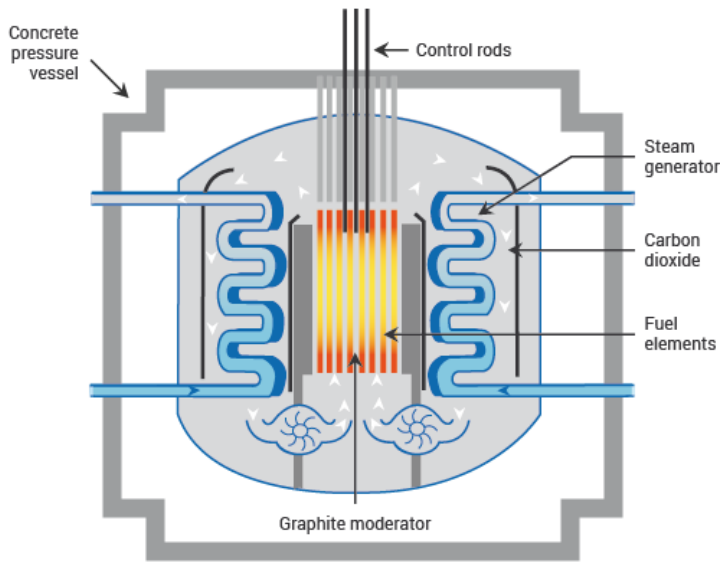

Figure 7: A schematic of the core of an AGR. From Ref (39).

The AGR reactor relies on a graphite core to moderate the neutrons and therefore sustain the fission chain reaction. However, the use of graphite presents a problem in the form of radiation induced oxidation (25).

$$C + CO_2 \rightarrow 2CO \tag{1}$$

To inhibit this degradation a small quantity of methane is added to the coolant (38). While this protects the core from degradation and therefore extends the life of the reactor core, the radiolytic degradation of the added methane results in a carbonaceous deposit which coats the fuel pins, an example of which is shown in Figure 8.

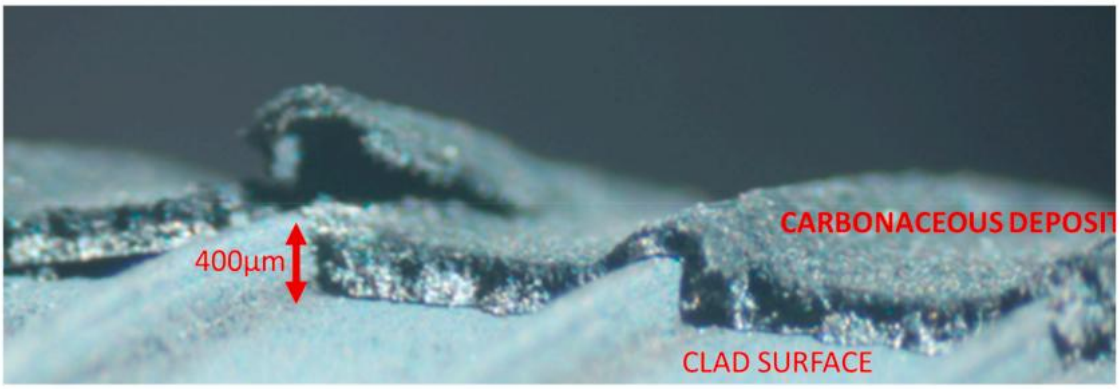

Figure 8: An example of carbonaceous deposit which has built up on AGR cladding. Taken from Ref (38).

3.2.1 The Fuel Assembly

The AGR fuel assembly is shown in Figure 9 and is comprised of a graphite sleeve, a stainless steel brace and the fuel pins held in the brace (40). A fuel pin comprises 64 annular pellets of UO_2 enriched to up to 3.5% ^{235}U and stacked inside the 0.375 mm thick 20/20/Nb stainless steel cladding. A total of 36 of these pins are then placed into a stainless steel brace and then into a graphite sleeve to form a fuel element. Eight of these elements (seven at Dungeness B) are stacked to form a fuel stringer and it is this that is inserted into the reactor (38).

Figure 9: A schematic of an AGR fuel element showing the pins, stainless-steel brace and graphite sleeve (41).

3.2.2 Cladding Material

When compared to the conditions found in the core of an Magnox reactor, the AGR core runs hotter (up to 825°C in an AGR vs 336°C for a Magnox station) resulting in a higher thermal efficiency (9; 42; 43). This along with the increased neutron flux necessitated the change to a stainless steel cladding in place of the magnesium alloy which had been used in the Magnox reactors. The AGR fuel is clad in a 20/25/Nb stainless steel, the composition of which can be found in Table 1 along with the

compositions of the two common grades of stainless steel – 304 which is often used for household items such as utensils and sinks and 316 which is used when harsher environments are expected such as for chemical transport and off-shore facilities (44; 45; 46).

Table 1: Composition of common stainless steels and AGR cladding (20/25/Nb). Compositions taken from (44; 45; 46).

Stainless Steel Grade	**304**	**316**	**20/25/Nb**
Carbon, C	0.07	0.07	0.062
Silicon, Si	1.00	1.00	0.58
Manganese, Mn	2.00	2.00	0.79
Phosphorous, P	0.045	0.045	0.014
Sulphur, S	0.015	0.015	0.019
Chromium, Cr	17.50 – 19.50	16.50 – 18.50	19.33
Nickel, Ni	8.00 – 10.50	10.00-13.00	24.05
Nitrogen, N	0.10	0.10	N/A
Molybdenum,. Mo	N/A	2.00 – 5.00	N/A
Niobium, Nb	N/A	N/A	0.7
Iron, Fe	Balance	Balance	Balance

The use of a stainless steel allows for the properties to be tailored to the expected use of the alloy. In this case the presence of 20% chromium and 25% nickel gives the alloy excellent resistance to the temperatures found in the reactor core, while the 0.7% niobium stabilises the stainless steel (9). The inclusion of the niobium helps to protect the grains from the depletion of chromium which would otherwise protect the boundaries from corrosion by preferentially forming niobium carbides rather than chromium carbides (40). Stainless steels and the degradation mechanisms both mundane and arising from reactor conditions are discussed further in section 3.4.

3.2.3 Failure Mechanisms of AGR Fuel Cladding

There are several mechanisms that can contribute to the degradation of an AGR fuel pin and have the potential to result in a through wall defect forming. These have been covered extensively by *Barker et al* (Ref (38)) and so shall only be summarised here.

Various degradation mechanisms have been observed to occur to the cladding of the AGR fuel during irradiation including:

- Fission gas overpressure – fission of U and Pu produces Xe and Kr which is initially held in the fuel matrix but can migrate over time and be released into the fuel pin internal gas volume.
- Pellet clad mechanical interaction (PCMI) – this form of degradation is generally understood to be the result of a mechanical interaction between the fuel pellets and the cladding. While initially there is a gap between the pellet and the cladding, this closes up under irradiation and can induce localised strain.
- Pin-brace interaction (PBI) – The stainless steel brace used to locate the individual pins within an element does not hold the pin rigidly to allow for thermal expansion of both the brace and the pin. As the coolant flows through the elements it can cause a vibration leading to the brace and pin coming into contact and the cladding wearing away.
- Ratcheting – Inside the fuel pin there are anti-stacking grooves designed to prevent the pellets from migrating downwards under gravity. Should the pellets migrate this can leave a section of cladding unsupported and at risk of creep collapse.
- Clad restructuring – This is a two-step process, the first is the result of critical strain grain growth which reduces the ductility of the cladding leaving it more vulnerable to the other degradation mechanisms discussed.

3.3 Storage of Nuclear Waste

The storage of spent nuclear fuel is a key challenge that must be solved in a manner that provides a safe, long term solution. Two approaches exist; wet storage and dry storage. Both of these are used around the world as interim storage techniques while disposal facilities are constructed.

3.3.1 Wet Storage of Nuclear Fuel

After the AGR fuel is removed from the reactor core, intact fuel is discharged into a pool at the reactor station for initial cooling. In order to prevent corrosion of the cladding and to lower the risk of an unintended criticality boron is added to the water (47). After the initial period at the reactor station, the fuel is transferred to Sellafield for interim storage. Upon arrival at Sellafield, the fuel is again stored underwater.

Initially, the ponds at Sellafield were filled with demineralised water. However, it was determined that with a corrosion rate of 0.5 μm/year in deionised water, the AGR fuel could be stored for 152 years if only general corrosion occurred (48). However, this

requires the chemistry to be carefully controlled. In 0.2-0.3 ppm chloride conditions, failure of the cladding was detected to occur within one to two years (47). Increasing the concentration of chloride further to 1 – 10 ppm and failure was observed after only 100 – 200 days.

To inhibit the corrosion of the cladding, studies were performed using various inhibitors and at different pH (15). The results of these studies suggested that dosing with sodium hydroxide (NaOH), also called caustic, was efficient at inhibiting the corrosion of the cladding. At pH 9, in 1 ppm and 2.5 ppm chloride the cladding was still intact after 1250 and 400 days respectively compared to failures occurring in under 200 days without the dosing. Some fuel had, in 2015, been stored in sodium hydroxide dosed, pH 11.4 demineralised water since 1989 and has not experienced any failure to the cladding.

3.3.2 Dry Storage of Nuclear Fuel

With pond storage having a finite space for the fuel, the alternative approach of dry storage has been used in various countries such as the United States which has operated a dry storage regime since 1986 (49). In the United Kingdom, the NDA has expressed that the storage of spent AGR fuel will continue to operate using a wet storage regime however dry storage will be investigated as an alternative (21). In this storage regime, the fuel is initially stored wet at the reactor location before being transferred to the casks once the criteria are met (50). Dry storage has been primarily employed for the storage of Pressurised Water Reactor (PWR) and Boiling Water Reactor (BWR) fuels which consist of UO_2 clad in zircalloy. Therefore, while there is experience of dry storage nuclear fuel, there is not the experience of dry storing stainless steel clad fuels. In the 1990's Scottish Nuclear did explore the viability of dry storing the AGR fuel but this did not progress beyond a proposed design (51). Since then, approval has been granted for the spent fuel from the Sizewell B PWR to be dry stored at the reactor, with Hinkley Point C following suit (52).

There is no preferred approach to preparing the spent nuclear fuel for the dry storage with two concepts used: vacuum drying (discussed in detail in section 3.3.2.1) and flowed gas drying (discussed in section 3.3.2.2). Removal of water from the exterior surface of an intact fuel pin is a relatively straightforward as the pin can be left to drip dry or for the water to evaporate off. The primary concern with dry storage is that any failed fuel will likely retain water within the pin which cause a concern as radiolysis can cause the production of hydrogen gas within either the storage or disposal environment.

3.3.2.1 Vacuum Drying

Vacuum drying has been utilised previously to dry spent nuclear fuel such as at Hanford where it was used to dry some of the stock of zircaloy clay uranium metal fuel stored there (25; 53). This approach involves sealing the fuel inside of a vacuum chamber and reducing the pressure. As the pressure is reduced, water present in the system evaporates more readily and can then be evacuated, rendering the specimen dry.

In order to determine if the spent fuel has been sufficiently dried, a vacuum rebound test is usually performed according to ASTM C-1553 (54). In such a test, the vacuum chamber is evacuated and isolated and the pressure monitored for 30 minutes, an example of which is shown in Figure 10 (55). After the half an hour has passed, if the pressure has remained below the 4×10^{-4} MPa (3 torr) limit then the material in the chamber is deemed to be suitably dry (55). However, *Goode et al* have raised the issue that it is possible to "cheat" the vacuum drying process by reducing the pressure further than normal to < 1 mBar (56). Once the system is isolated, even a substantial rate of pressure increase of 6 mBarA/hr would result in a passed test despite this rate corresponding to a significant quantity of water evaporating.

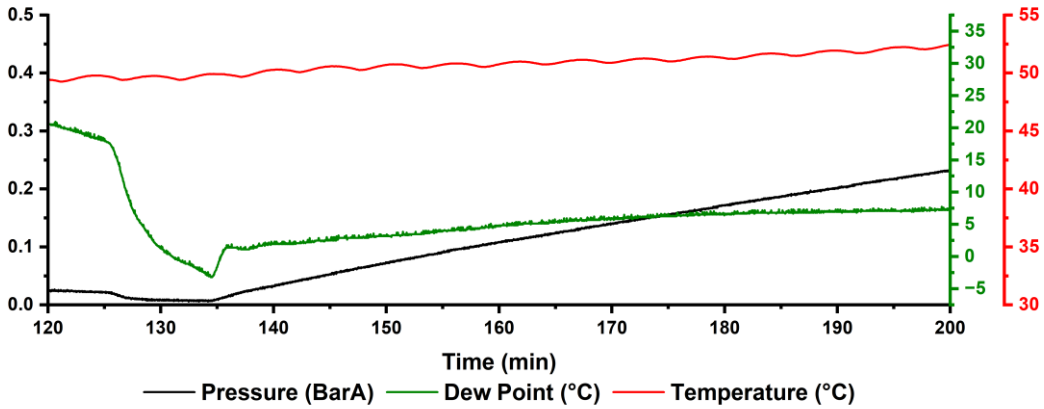

Figure 10: A vacuum rebound test performed as part of the vacuum drying tests.

The mass of water present in the system at the end of the rebound test can be calculated using the ideal gas law (57).

$$PV = nRT \qquad \textit{Eq. 1}$$

$$\frac{P_1V_1}{n_1} = \frac{P_2V_2}{n_2} = RT \qquad \textit{Eq. 2}$$

$$n_2 = \frac{P_2V_2}{P_1V_1}n_1 \qquad \textit{Eq. 3}$$

As V1 = V2:

$$n_2 = \frac{P_2}{P_1} n_1 \qquad \textit{Eq. 4}$$

From this, an upper limit for the mass of water present in the vessel can be calculated.

Vacuum drying also allows for the possibility of ice to be formed during the evacuation and therefore it may be beneficial to undertake the evacuation at a reduced rate or in stages (55; 57).

3.3.2.2 Flowed Gas Drying

The other main approach being considered as a means to dry spent nuclear fuel is to use forced-gas dehydration, also known as flowed gas drying (FGD). In this approach a dry, nonreactive, heated gas such as helium or nitrogen is circulated through the vessel containing the materials to be dried (55). The carrier gas is circulated and dehydrated with each circuit until the moisture content in the gas returning to be dehydrated is equal to the moisture content of the gas after dehydration (58). *J. Goode et al*, previously investigated the possibility of using flowed gas drying as a means to dry failed AGR fuel (59). It was determined in this work by *J. Goode et al,* that while FGD was a possible means to remove residual water from failed fuel, it was not as efficient as vacuum drying.

FGD has also been used by the Canadian National Laboratories as a means to remove water from a tile hole. In this work, due to the nature of the material to be dried, could not be placed into a vacuum chamber and dried. Instead, a dry air-argon mixture was added to the tile hole as the carrier gas with ~250 mL of water removed per 8 hour run time (60).

3.3.3 Geologic Disposal of Nuclear Fuel

At present, the UK's spent nuclear fuel is undergoing interim storage pending a future decision on whether to declare it as a waste for disposal in a GDF (61). This process would involve placing the spent fuel (along with other radioactive waste materials) into an engineered facility deep underground, with an illustrative example of the GDF shown in Figure 11. Several countries have already begun excavating and construction of a GDF such as Sweden, the United States (Yucca Mountain) and Finland where disposal of spent fuel has already started (62; 63; 64).

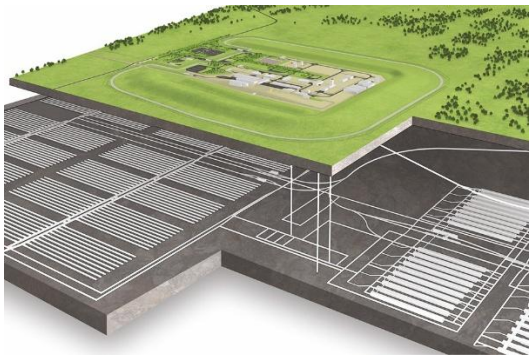

Figure 11: Conceptual computer generated image of a GDF. Taken from (65).

In the UK, site selection has been ongoing since 2018 and as of May 2025 three areas have volunteered as potential hosts; East Lincolnshire, Mid Copeland and South Copeland (66; 67). Currently it is planned that any GDF built by the UK will be ready to accept spent fuel from 2075. As a result it will be necessary to store the UK's inventory of spent fuel for approximately another 50 years (14).

3.4 Stainless Steels

3.4.1 Overview

Steel has been used in numerous applications proving to be one of the most important materials in use. However, exposure to atmospheric conditions can result in corrosion. By alloying steel to form a stainless steel, its properties can be tailored to make it suitable for a wide range of purposes. For example, the addition of copper to form an alloy such as 904L gives the stainless steel excellent resistance to acidic corrosion while the 300 series have increased resistance to temperature (68; 69). However, this tailoring can't prevent the stainless steel being impacted by various conditions such as those experienced by the cladding of the AGR fuel. These conditions can lead to the degradation of the stainless steel and leave it at an increased risk of corrosion. This is of concern to the nuclear industry as any failure of the AGR cladding could lead to the release of fission products and allow water from the pond to come into contact with the fuel inside.

3.4.2 Sensitisation of Stainless Steels

One factor which can lead to the degradation of stainless steel is sensitisation which reduces the corrosion resistance of the material. This phenomena occurs when a stainless steel is exposed to elevated temperatures in the region of 500 – 850 °C and slowly cooled (70). During the exposure to the elevated temperatures, $(CrFe)_{23}C_6$, also referred to as $M_{23}C_6$, precipitates onto the chromium present adjacent to the grain

boundaries (71). How susceptible a stainless steel is to sensitisation depends on the duration of the exposure to the elevated temperature and the carbon content of the alloy as shown by the Time-Temperature-Transformation diagram in Figure 12. For example, a stainless steel containing 0.042 % carbon can be subjected to 600 °C for half an hour without sensitisation occurring. However, if the same stainless steel is exposed to the elevated temperature for one hour then sensitisation will occur. By reducing the carbon content, the temperature required generally decreases however the exposure time increases.

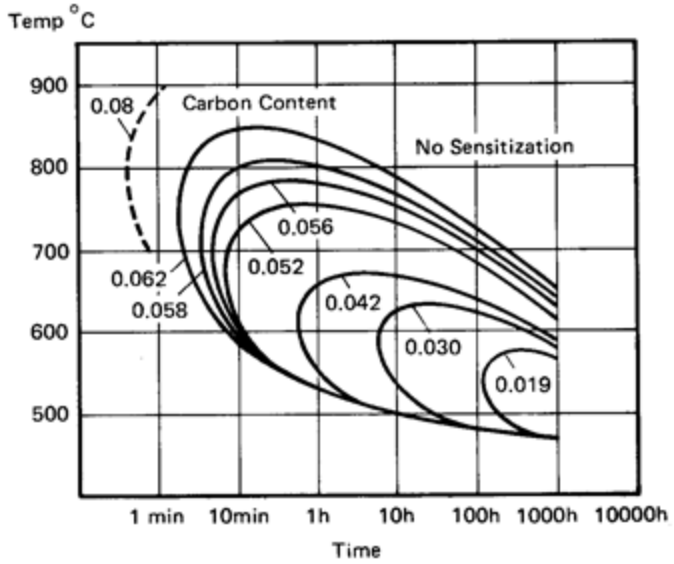

Figure 12: Time-Temperature-Transformation (TTT) diagram for 304 stainless steel. Taken from (72).

When choosing a stainless steel it is possible to minimise the impact of sensitisation by including elements such as titanium, niobium and tantalum as carbides of these elements precipitate out preferentially when compared to chromium carbides. This is why, in the stainless steel chosen for use in the AGR cladding, 0.7 wt.% of the alloy is niobium.

3.4.3 Radiation Induced Segregation

Due to the addition of niobium to the stainless steel alloy, the impact of thermal sensitisation is reduced owing to the precipitation of niobium carbides. However, within the reactor, the neutron flux can cause another phenomena known as radiation induced segregation (RIS) to occur. When RIS occurs, it results in the redistribution of the alloying elements, most notably for this work, chromium, away from the grain boundaries leaving the cladding in a sensitised state (73). It has been determined that this effect is most severe in the temperature range of 400°C – 420 °C. Elements one and

two of the fuel stringer experience these temperatures within the reactor core and are therefore considered to be at risk of RIS and increased risk of failure in the storage environment.

3.5 Corrosion

3.5.1 Overview

Corrosion is a process which is observed on a daily basis such as rusted chains. It is defined as the deterioration of a material from either electrochemical or chemical reactions between the material in question and its environment (74). The general equation follows the redox reaction as follows:

$$M \rightarrow M^{n+} + ne^- \qquad \textit{Eq. 5}$$

$$O_2 + 4e^- + 2H_2O \rightarrow 4OH^- \qquad \textit{Eq. 6}$$

$$2H^+ + 2e^- \rightarrow H_2 \qquad \textit{Eq. 7}$$

$$H_2O + 2e^- \rightarrow 2OH^- \qquad \textit{Eq. 8}$$

While corrosion can come in many forms, the most relevant forms of which are covered here, generally it can be broken down into two categories:

1. General corrosion
2. Localised corrosion

General corrosion covers a relatively large area of the material and is less relevant for the corrosion which could potentially occur on the AGR cladding however, it is covered here briefly. Localised corrosion on the other hand is often harder to observe and is the grouping of concern where the corrosion and failure of the cladding is concerned.

Stainless steels such as the 20/25/Nb stainless steel used for the AGR cladding are usually protected by a passivating layer which inhibits the corrosion of the stainless by either steel underneath. However, should that layer become damaged by either mechanical or chemical means then corrosion can occur.

3.5.2 Forms of Corrosion

This section will cover the principle forms of corrosion which were expected to be encountered during either the interim storage of the spent fuel or during experiments conducted as part of this investigation. Focus has been given to stress corrosion cracking as this was deemed to be the most likely corrosion mechanism to produce representative defects.

3.5.2.1 Uniform Corrosion

This is the most common form of corrosion causing uniform loss of material across the surface of the material in question (75). This can be easily predicted and measured therefore it is unlikely to cause catastrophic failure (76). It has been documented that this form of corrosion can achieve rates on the order of mm/year though in a neutral to alkaline environment the passivating layer on the surface of the stainless steel reduces this rate (47). Prevention of this form of corrosion is relatively simple. The application of coatings such as paint can be used. In addition, cathodic protection can be used, this is done by connecting the material you wish to protect to a sacrificial anode – in the case of a stainless steel zinc could be used. In the same environment the anode will preferentially corrode (77).

3.5.2.2 Pitting and Crevice Corrosion

Pitting and crevice corrosion are very similar mechanistically and therefore will be considered together here.

Pitting corrosion occurs when a small section of the passivating layer becomes damaged exposing the surface of the stainless steel to the corrosive environment. Typically, small holes are formed in the surface of the material which can become covered with corrosion product making the defects difficult to detect (78). Several types of pits are possible, which are outlined in Figure 13 and set out in ASTM G46.

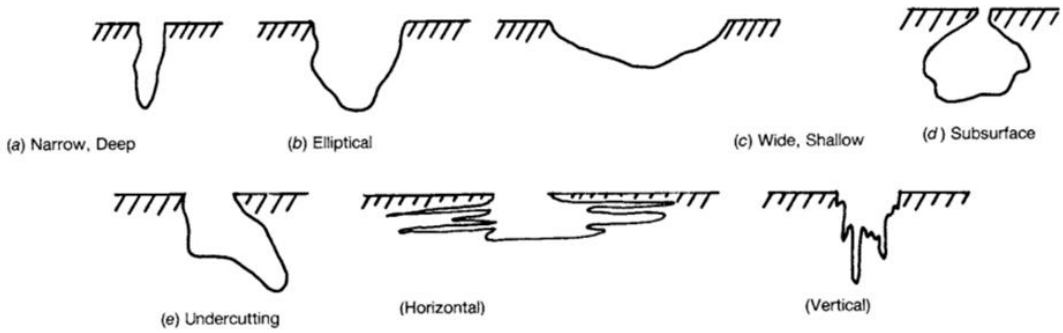

Figure 13: Types of pitting corrosion as set out by ASTM G46 (79).

In order for pitting to occur, either the oxide layer on the surface or the surface itself must become damaged. This allows for an autocatalytic cell to develop as shown in Figure 14 (80). Inside the defect, the metal dissolves off as a positively charged ion which attracts chloride ions into the cell forming a metal chloride that undergoes hydrolysis to form a hydroxide and hydrochloric acid. This lowers the pH inside the

defect accelerating the dissolution of the metal (81).

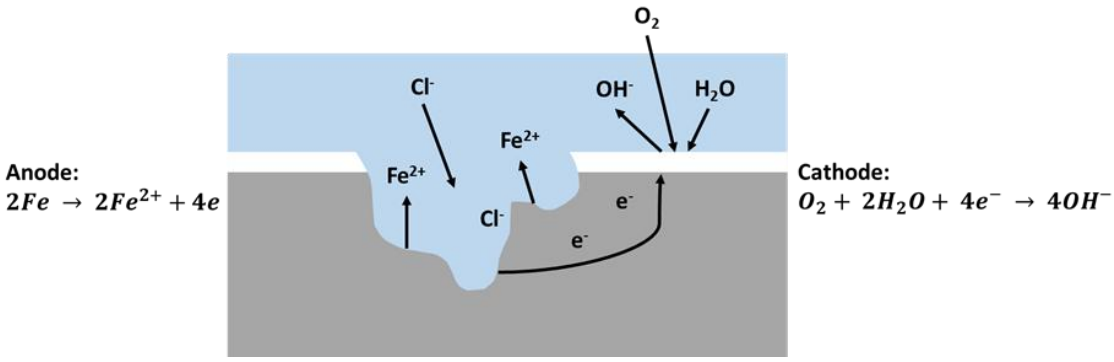

Figure 14: A schematic of the autocatalytic cell which develops in a pit.

Crevice corrosion however, does not require the passivating layer to be damaged in order for the degradation to occur. Instead, crevice corrosion occurs when solution becomes stagnant and isolated from the bulk solution for example around riveted plates or rubber seals, shown schematically in Figure 15. Initially, the corrosion reaction will occur over the entire surface of the material including inside the crevice region (80). Once the oxygen within the region of stagnant solution has been consumed, more mobile ions such as chloride will migrate into the solution. At this point the mechanism is identical to that of pitting corrosion.

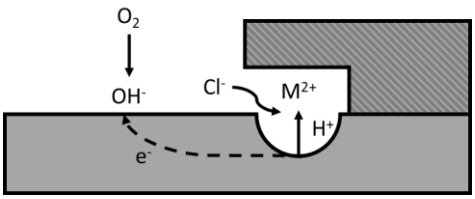

Figure 15: Schematic of crevice corrosion. Adapted from Ref (47).

3.5.2.3 Galvanic Corrosion

When two dissimilar metals are in contact with each other in a corrosive environment a galvanic couple is formed (82). In such a scenario, one of the two metals is found to corrode more readily than the other with the corrosion occurring quicker than it would otherwise. The galvanic series, shown in Figure 16 shows the nobility of different metals which in turn can be used to predict which of the two metals will corrode (83). For example, if a 304 stainless steel and a low alloy steel are paired in a corrosive environment the less noble material – in this case the low alloy steel – will act as the anode and therefore corrode at an increased rate when compared to the anode.

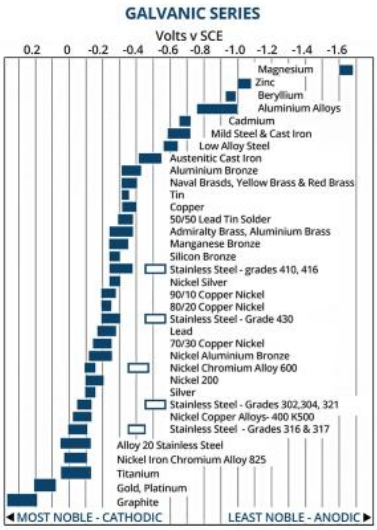

Figure 16: The galvanic series. Taken from Ref (84).

3.5.2.4 Stress Corrosion Cracking

Defined as a progressive fracturing of the material, it is considered to be a very unpredictable corrosion mechanism with failure possible in as little as a few hours (85). For stress corrosion cracking to occur, three factors must be present in the system, a susceptible material must be held in a conducive environment while under stress, as outlined in Figure 17. It should be noted that corrosion of a material followed by the application of stress is not sufficient to cause stress corrosion cracking.

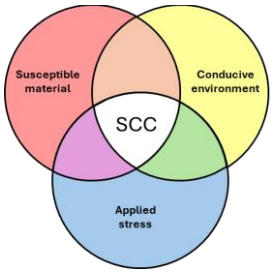

Figure 17: Conditions required for stress corrosion cracking to occur.

Initially, it was assumed that only specific materials under specific conditions however, this view has been shown to be incorrect with a wide range of alloys undergoing stress corrosion cracking (SCC) in a variety of conditions (86). One environment which is known to be particularly potent for SCC in stainless steels is to introduce a hot, concentrated chloride solution.

Despite the large amount of research done into SCC, it is not known exactly what the mechanism which causes the cracking to occur is. While many solutions have been proposed, in the nuclear industry the primary mechanism used to describe SCC is the

slip dissolution/film rupture model which postulates that the crack grows as a result of a passivating film being ruptured allowing for a small quantity of material to be removed before the film reforms and the cycle repeats. Once the metal is exposed to the corrosive solution a mechanism similar to that which generates pits in the metal corrodes the crack tip while the sides remain passivated, thereby elongating the crack. A second method, called the enhanced surface mobility theory stats that the atoms from the highly stressed tip of the crack diffuse to the side of the crack where the stress is reduced and was developed in response to the theory that the oxidation currents at the crack tip were not sufficient to explain the high growth rates of the cracks.

Most stress corrosion cracking initiates from a pit site or similar defect in the metal surface where the solution has become concentrated due to stagnation with the cracking occurring perpendicular to the applied stress. Depending on the alloy and the conditions experienced by the metal, either trans granular or intergranular cracking can occur, with intergranular being more likely if sensitisation has occurred due to the reduction in corrosion resistance at the grain boundaries.

It is also known that caustic solutions are capable of producing SCC, known as caustic cracking, under the right conditions (87). Usually this is observed in boilers where NaOH has been added to help prevent the formation of scaling. It has been observed to occur in locations where a concentration of sodium hydroxide can occur such as around rivets. In low carbon steels, low concentration caustic solutions can be safely handled up until 82°C though this temperature limit is reduced to 65 °C in a solution comprising 50% caustic with some cracking has been observed at temperatures as low as 48 °C (88). Stainless steels on the other hand are much more resistant to caustic cracking with the critical temperature being approximately 120 °C.

3.5.2.5 Intergranular Corrosion

Intergranular corrosion (IGC), also referred to as intergranular attack (IGA) is a localised corrosion phenomenon which preferentially occurs along the grain boundaries of a material while the bulk material remains relatively unaffected (89). When a stainless steel undergoes sensitisation (see 3.4.2) the carbon present in the bulk material diffuses to the grain boundaries (90). At the boundaries the chromium which usually protects from IGA precipitates out as chromium carbide ($Cr_{23}C_6$)leaving a zone around the boundary depleted of Cr and therefore vulnerable to corrosion via IGA as shown in

Figure 18. This is due to the depleted zone becoming anodic with respect to the bulk material (91).

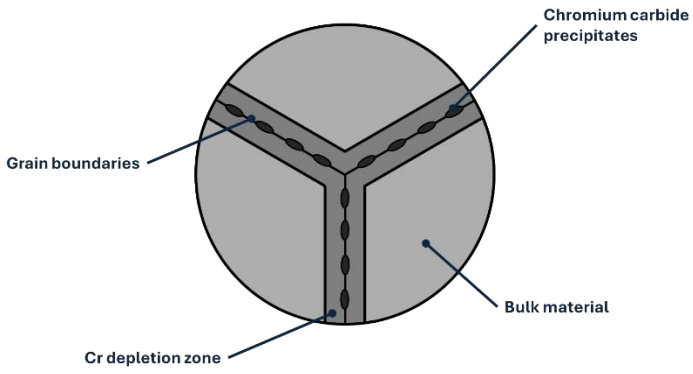

Figure 18: A vulnerable grain boundary. Adapted from Ref (92).

In order to reduce the impact of sensitisation, other elements can be added to the alloy such as niobium, in the case of the AGR cladding, or Ti and Ta in other use cases (46; 93). These stabilising elements form carbides at higher temperatures than the chromium, the carbon combines with these stabilising elements and as a result there is a reduced amount of chromium carbide formed in the grain boundary.

3.5.3 Generation of Representative Corrosion Defects

In order to produce representative defects in stainless steel a reliable and repeatable method is required. The current understanding of the corrosion of the spent fuel indicates that narrow, tortuous cracks are formed in the cladding through intergranular stress corrosion cracking. From an examination of the literature, two methods were identified as possible approaches which would be suitable for the production of defects: immersion in a corrosive media and the drop evaporation technique.

3.5.3.1 Immersion Testing

One means to produce stress corrosion cracks in stainless steel is to immerse the sample in a corrosive electrolyte while under stress such as in the process used by *Steinsmo and Drugli* (94). In the approach set out, the sample of stainless steel is submerged in a concentrated seawater solution as shown in Figure 19.

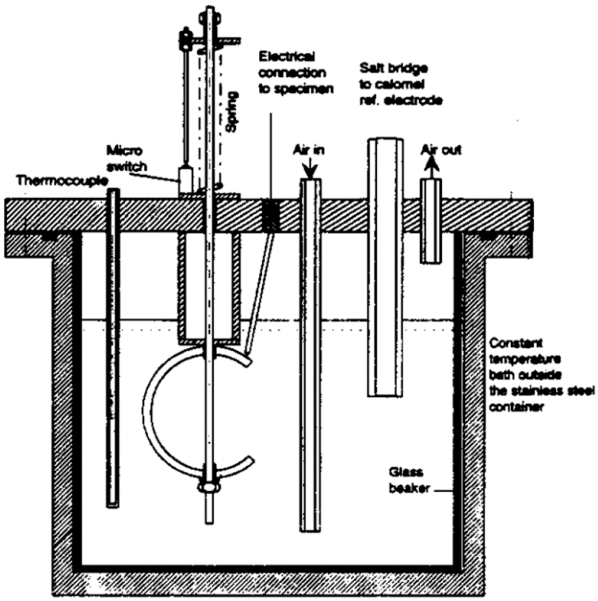

Figure 19: The immersion test set up used by Drugli and Steinsmo (94).

To undertake the tests, a c-ring sample is stressed to near its yield strength and clamped into place. An electrical connection is then established with the sample and a micro-switch in order to end the experiment should cracking occur and prevent the catastrophic failure of the sample. A concentrated seawater simulant was used at two different temperatures; 90°C and 132°C. These temperatures corresponded to concentrations of 8.2 M/L and 9.5 M/L respectively. An electrolyte was also tested with a pH of 1.6-2.5 at 132°C. In testing it was found that the grade of stainless steel heavily influenced the time taken for cracks to form with durations of 670 to 4000 hours reported.

While this method has been shown to be capable of producing stress corrosion cracks, the inability to observe the process during the testing and the complexity of the set up to ensure the cracking does not progress beyond the desired extent were considered to be key challenges which would need to be addressed should the technique be utilised. Additionally, the use of a C-ring sample presented challenges. Should cracking occur, the curved nature of the sample would then prove to be harder to fashion a test piece suitable for the vacuum drying experiments when compared to a flat sample.

In addition, other researchers have found that pH 2 solutions were unable to replicate the corrosion observed to be produced via other approaches with the suggestion made that localised conditions generated by the other approach was the cause.

3.5.3.2 Potassium Tetrathionate

The petrochemical industry has experienced failure of stainless steel components via SCC owing to the presence of a polythionic acid such as potassium tetrathionate (95). It has been shown that exposure to a 0.1 M solution of $K_2S_4O_6$ acidified to pH 2 with sulphuric acid was capable of suitably corroding the stainless steel in a relatively short time frame (96; 97). This approach also allowed for the use of flat specimens to be used for testing which is beneficial for further testing should suitable defects be produced. A flat sample geometry is also advantageous for the observation of the corrosion. In this scenario, a sample can be removed, washed and examined using microscopy to determine the extent of the cracking before returning it to the corrosive environment. This would help to ensure that catastrophic failure of the sample does not occur. A further advantage to this method is that, compared to the others discussed, no external heating is required with tests undertaken at room temperature.

3.5.3.3 Drop Evaporation

The other primary option considered for inducing stress corrosion cracking of the samples was to utilise the drop evaporation technique. This approach has been used extensively to undertake research into the impact of sea spray evaporating off stainless steels in marine environments such as offshore oil rigs and coastal facilities.

In order to replicate the conditions experienced by a component exposed to the saline environment, the technique requires a flat sample to be placed under stress such as by inducing a deflection in the sample which is then heated to the desired temperature for the test. Finally, the corrosive solution is dripped onto the centre of the sample.

While other means of inducing a tensile stress in the sample are possible, most literature, such as experiments performed by *Pereira et al*, use a modified form of the four-point bend test, as shown in Figure 20 (98; 99).

Figure 20: The modified four-point bend test rig used by Pereira et al to induce stress on the samples.

Once the desired stress has been applied by raising the lower plate, the set-up is inserted into an oven and heated to the desired temperature, 90°C or 110°C for the tests

performed by *Pereira et al*. Once the sample has been suitably heated, a pH 8.2 synthetic seawater was dripped onto the centre point of the sample at a rate slow enough to allow for the previous drips to evaporate, thereby concentrating the chloride and making the remaining solution increasingly aggressive. It was concluded by *Pereira et al,* that the technique is a suitable means of producing SCC in a stainless steel provided test temperatures of 110°C were used. Other research by *Steinsmo and Drugli* however, tested a range of grades of stainless steels at temperatures between 117°C and 155°C but also report that 316 stainless steel is capable of cracking at temperatures as low as 30°C in a similar set-up (100).

In the British standard, *BS EN ISO 15324:2008*, sets out a standard for the drop evaporation method, specifying a drip rate of 10 droplets per minute (101). It is also recommended that samples have a circular cross section and a dog-bone shape however this geometry is not suited to the work performed here but it informed the experiments undertaken. A standard method is outlined in Table 2 along with the adaptations made by *Hinds and Turnbull* (102).

Table 2: The ISO standard for the drop evaporation technique and the adaptations made by Hinds and Turnbull.

	ISO Standard	**Hinds and Turnbull**
Specimen Temperature (Dry)	300°C	70°C - 110°C
Test Solution	0.1 M NaCl	ASTM Seawater
Specimen Geometry	Cylindrical	Flat dog bone
Test Duration	500 Hours	336 Hours
Wetting Cycle	Dries between drops	Remains wetted

During their investigation, *Hinds and Turnbull* were able to adapt the process to reduce the temperature from 300°C to between 70°C and 110°C while still producing SCC in the samples. It is also notable that the work by *Hinds and Turnbull* utilises a flat dog bone sample geometry which is also found in the majority of the literature, rather than a cylindrical sample. Another point of difference is the change in the wetting cycle process. In the ISO standard, it is set out that the sample should be allowed to dry fully prior to the next droplet of corrosive solution being administered however, in practice it has been favoured to forgo this and allow the sample to remain slightly wetted.

This adaptation results in the zone around the dripping location remaining cooler than the rest of the sample which was theorised to potentially result in a lack of corrosion

occurring in the region however SCC was still observed to occur. One other observation made by *Hinds and Turnbull* among others conducting research using the drop evaporation technique, was the build-up of salt around the dripping location which was determined to be advantageous to corrosion. Figure 21 shows a temperature profile for the surface of a sample undergoing the drop evaporation corrosion technique and highlights the reasoning as to why each droplet should be left to fully evaporate in order to ensure that the sample returns to the test temperature. It was however, noted by *Hinds and Turnbull* that the cyclic temperature profile could be a possible failure mechanism in itself though this was deemed to be unlikely due to the temperature change only being recorded as 1°C or 2°C. The temperature change noted by *Hinds and Turnbull* differs from that recorded by *Jin* as shown by the fluctuations observed in Figure 21 (102; 103). It is suggested that by not allowing the sample to fully dry between droplets, the temperature fluctuation is reduced which would account for the change seen.

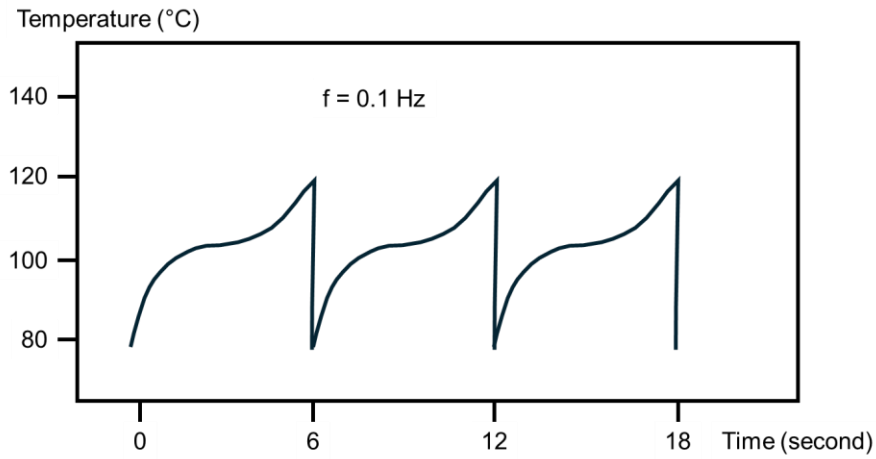

Figure 21: The typical surface temperature of a sample undergoing the drop evaporation technique. Adapted for clarity from (104).

Other variations on this technique are possible such as the means for applying a stress to the sample. For example, *Lasek et al* attached a mass to one end of the specimen to induce stress though this approach also used temperatures in the 250°C range which is higher than most of the other work undertaken using the drop evaporation technique used (105).

While most tests performed are aimed at studying the effects of seawater and therefore utilise either a NaCl solution or a synthetic seawater, however, other aggressive solutions can be used. *Tsutsui et al*, for example, used a $MgCl_2$ solution and did not stress the sample or drip the magnesium chloride solution onto the sample, preferring instead to place droplets on the surface as required as this study was focused on the

production of pits rather than SCC (106). It was noted however, that the initiation of pitting corrosion required a solution of 6 M or greater.

3.5.4 Analysis Techniques

In order to examine the samples both during and after the corrosion experiments, a variety of techniques will be used and are summarised in Table 3 and these are discussed in further detail below.

Table 3: Overview of techniques used to analyse corrosion test samples.

Instrument	Technique	Brief Overview
Olympus SZX10 Macro Stereo Microscope	Macroscope	Initial analysis of the sample to survey large areas at low magnification and detect sites of interest for further examination. Covers a magnification range of 6.3x to 63x.
Olympus BX51 Research System Microscope	Microscope	Higher quality images of corrosion sites, capable of revealing grain boundaries and cracking at the base of pits.
Carl Zeiss LSM800 Mat Confocal Laser Scanning Microscope (CLSM)	CLSM	High resolution images with the capability to produce “z-stack” images resulting in the entire image being in focus despite a change in the height of the surface. Laser scanning also allows for topographic height mapping of the sample.
Hitachi TM3030Plus SEM with EDX	SEM & EDX	Very high magnification images of the sample (magnification in the 1000’s) along with composition possible via the EDX attachment.
Zeiss X-ray Microscope Xradia 410 Versa	XCT	Able to image through the depth of the sample and reveal the full extent and pathway of a crack or pit via a 3D reconstruction from which cross sections can be viewed.

3.5.4.1 Optical Microscopy

Optical microscopy is the most straightforward means by which a sample can be magnified. The basic principle is that light is either transmitted through the sample from below of reflected off the sample and passes through a series of lenses resulting in a magnified image. While transmitted light is the most common approach that most people will have come across from their time in school biology labs for looking at cells, in this work transmitted light was not used due to the opaque nature of the samples. When an opaque sample is being analysed, a reflected light source is required to ensure suitable definition on the surface of the sample can be resolved. This technique has been used extensively across numerous industries and applications to allow the user to resolve details that the human eye would be unable to pick out otherwise.

Within optical microscopy, two different contrast modes are available (on certain models of microscopes) brightfield and darkfield (107). In a brightfield set-up the light incident on the sample (in reflected light mode) is reflected by a semi-silvered mirror before being focused onto the centre of the objective lens while the darkfield set-up places a block in front of the incident light effectively creating a ring mirror which causes the incident light to be directed towards the edges of the objective lens. This has impacts on the sample features which can be detected. In brightfield set ups the light is incident on the sample at an acute angle of between 45° and 90° from the horizontal plane and therefore, the surface features which absorb or scatter the light will appear dark against a bright background. Darkfield, on the other hand, requires the incident light to hit the surface at an oblique angle and therefore the majority of the light incident on the surface is scattered away from the lens. Edges and defects present on the surface however, will result in the light being reflected into the lens thereby showing up as brighter regions on a dark background.

The primary microscopes that will be used are the Olympus SZX10 Macro Stereo Microscope and the Olympus BX51 Research System Microscope. The SZX10 would be the first option to use to analyse a sample. The SZX10 is equipped with a separate light sources on movable arms allowing for the sample to be illuminated in order to accentuate surface features. This microscope requires minimal sample preparation or set-up and is therefore ideal for quick investigations of the sample to check large areas for potential pitting and cracking. With a large working distance it is also ideal for examination of the stressed samples to locate regions which can be sectioned out for further analysis under higher powered microscopes.

Should further analysis be deemed necessary then the Olympus BX51 Research System Microscope would be one option. This microscope is equipped with higher magnification lenses and both bright and darkfield capabilities. This would therefore allow for an increased level of detail to be observed on the surface of the sample. However, due to the increased magnification of the lenses attached it is necessary to determine regions of interest prior to the use of this microscope. The possible working distance available to this microscope is also reduced when compared to the Olympus SZX10 Macro Stereo Microscope prompting consideration to be given to how useful the system would be.

3.5.4.2 Confocal Laser Scanning Microscopy

The Confocal Laser Scanning Microscope (CLSM) provides capabilities beyond that of the other light microscopes present such as those discussed in section 3.5.4.1. Two features in particular were considered to be crucial for the analysis of any defects produced. The first is the ability to produce a z-stack. To produce this an image is taken with the microscope set to move through a range of focal planes capturing an image at set intervals, as shown schematically in Figure 22. These images can then be stitched together to create an image which results in the entire range being in focus at once providing a means to examine the full depth of a pit where normally only the one slice could be observed in focus at any given moment.

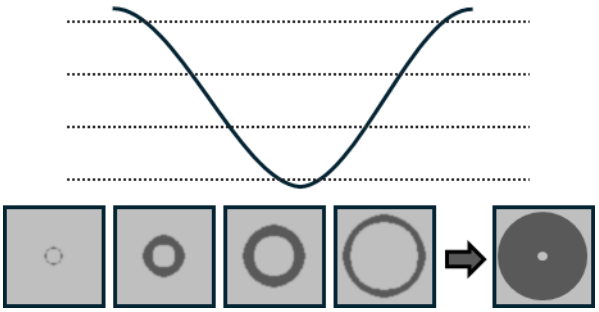

Figure 22: Schematic showing different planes used to create a z-stack.

With the CLSM this can be taken one step further. By scanning a laser across the surface of the sample in a raster pattern, the software is able to build up a topographic profile of the sample. This can then be analysed to determine the depth of any pits or defects which are present in the sample.

3.5.4.3 SEM and EDS

A Scanning Electron Microscope (SEM) uses electrons to produce very high magnification images of the sample at high resolutions. Two modes of operation are

possible; backscatter electrons and secondary electrons with Figure 23 showing a schematic of the region in which the different electrons are generated.

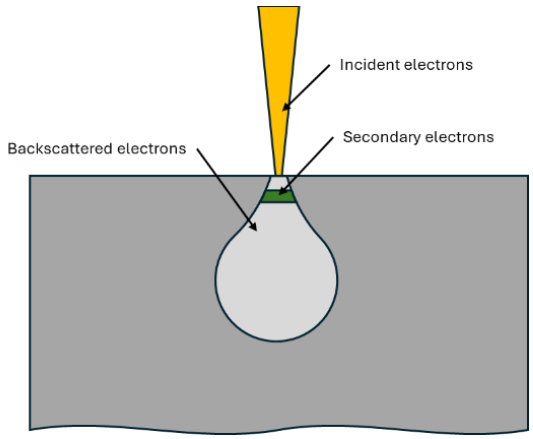

Figure 23: Schematic showing the difference between where backscatter and secondary electrons are produced during imaging by an SEM. Simplified from (108).

When the electrons hit the surface of the sample a few microns of penetration is achieved prior to the electrons interacting with the atoms which make up the sample. The depth at which this interaction occurs depends on the material density and the accelerating voltage being used.

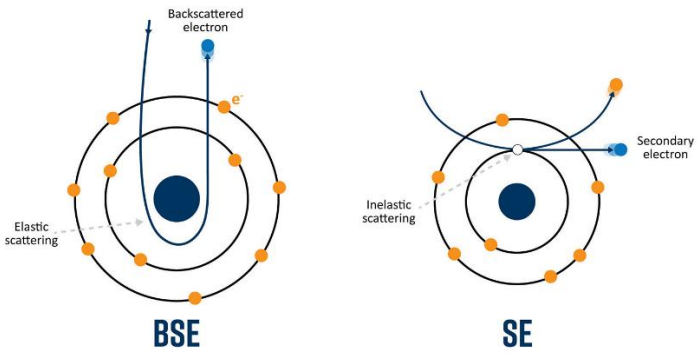

Figure 24: The difference between backscattered electrons and secondary electrons. Image from (109).

In order to generate images that highlight surface topography, secondary electrons are used due to the near-surface region where the generation occurs. These electrons, as shown in Figure 24, arise from the inelastic scattering of an electron-electron interaction (108).

In backscatter mode, the electrons detected are being generated much deeper in the material and therefore do not provide the user with as much information concerning the topography of the sample. However, this mode is a useful means to determine information about the composition of the sample. Where the sample is composed of different elements, the denser elements will show up as brighter region on the display

due to an increased proportion of the incident electrons being scattered back towards the detector, as shown schematically in Figure 25.

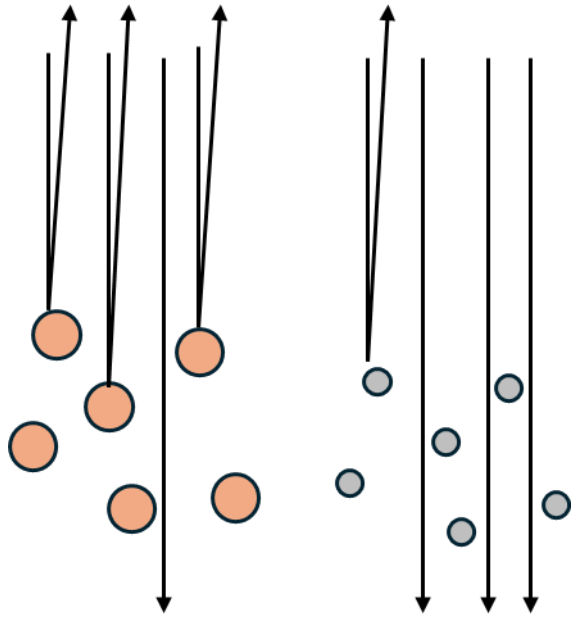

Figure 25: An illustration of the interaction between incident electrons and two materials of different density showing how the more dense material scatters a higher proportion of electrons back at the detector. Simplified and adapted from (108).

Owing to the high resolution and magnification possible from an SEM, the approach will be able to provide the possibility for a detailed investigation in to corrosion effects ongoing at the base of pits which could not be observed via other means.

The SEM set-up also allows for the composition of the sample to be measured using Energy Dispersive X-ray Spectroscopy or EDS. This technique utilises the x-rays which are produced when the incident electrons from the SEM cause the emission of an x-ray from the atom the electron interacts with, as shown schematically in Figure 26 (110). As these x-rays are characteristic of the element which generated them this interaction can be used to determine the composition of the region being imaged (111).

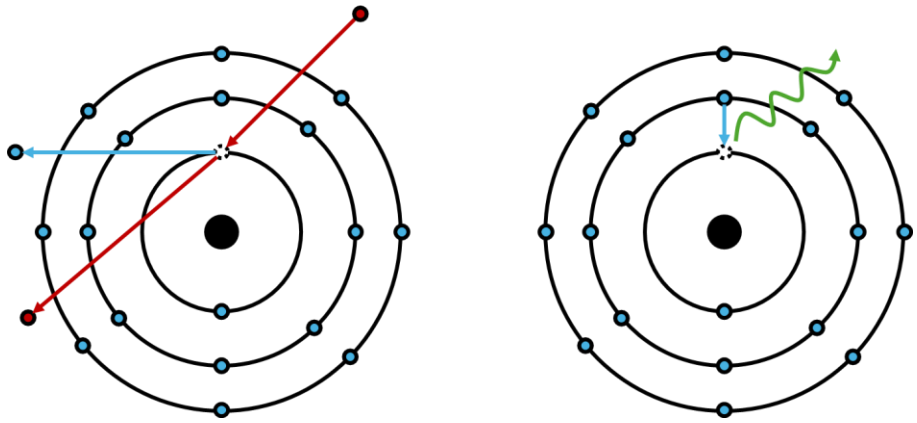

Figure 26: A illustration showing how an x-ray is emitted from an atom to then be detected by EDS.

3.5.4.4 X-Ray Computed Tomography

The final analysis technique to be used is X-Ray Computed Tomography or XCT. In this technique, x-rays are directed at the sample with a detector placed behind the sample (112). As the intensity of the incident x-rays is known and the intensity at the detector is measured it is possible to determine the density of the material in the sample (113). This process is repeated either rotating the sample or the source and detector to build up a 3D model of the sample as shown in Figure 27.

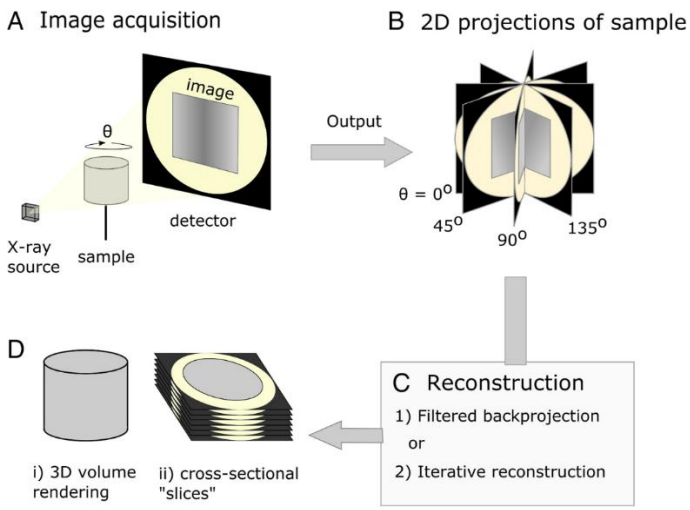

Figure 27: Schematic showing the principles behind the x-ray computed tomography set up (114).

3.6 Fluid Flow

Fluid flow can refer to either the flow of a gaseous media or a liquid media however, in this work it will primarily be used to refer to the flow of gas. This section will set out the different types of flow models which were examined and the merits of each.

3.6.1 Flow Regimes

Flow regimes describe a flow structure or a distribution of one fluid relative to another in the same volume, for example water and air in a sloped pipe (115). This governs how the fluid in question interacts with the surroundings and can also influence the properties of the fluid (116). A key value in determining the flow characteristics is the Reynolds Number, Re (117). This is defined as:

$$Re = \frac{d \cdot V \cdot \rho}{\mu} \qquad \textit{Eq. 9}$$

This number can be used to determine the type of flow occurring, such as laminar or turbulent with the bounds to these regimes set out in Table 4.

Table 4:The Reynolds number and range for the different flow regimes (117).

Flow Type	**Reynolds Number**
Laminar	Re < 2,300
Transition	2,300 < Re < 4,000
Turbulent	Re > 4,000

3.6.1.1 Laminar Flow

Laminar flow occurs when the fluid particles move in smooth and parallel paths as shown in Figure 28. This is usually found when there is a low flow rate and through an unobstructed flow channel (118). As stated in Table 4, laminar flow occurs when the Reynolds number is below 2,300.

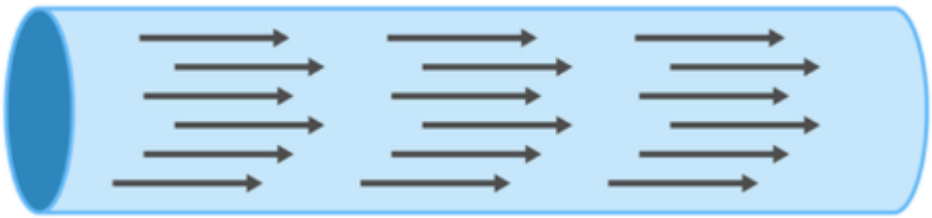

Figure 28: Laminar flow in a pipe shown schematically. Image from Bronkhorst (118).

3.6.1.2 Turbulent Flow

The other main flow state is turbulent flow. In this state, the flow contains eddies and instabilities unlike laminar flow, as shown in Figure 29 (119). In pipe systems, turbulent flow usually arises from flow passing through restrictions such as valves and adaptors (118).

Figure 29: Turbulent flow in a pipe shown schematically. Image from Bronkhorst (118).

3.6.1.3 Transition Flow

Between the two main flow regimes of laminar and turbulent flow, there is the transition phase where one regime changes into the other with the Reynolds number for this transitions depending on a variety of factors that are fluid and system specific (120). Constant changes in the fluid's speed and directions occur during this regime as shown schematically in Figure 30.

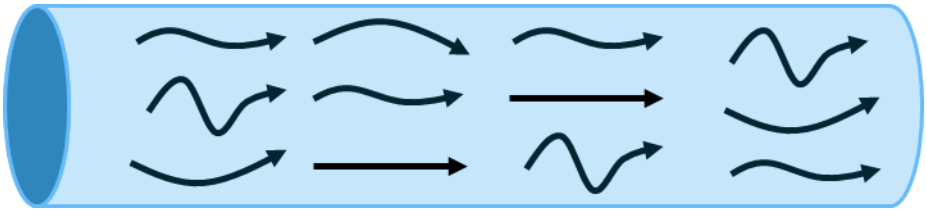

Figure 30: Transition regime flow shown schematically highlighting the changes in direction that occur in this regime while the overall flow remains fairly linear.

3.6.1.4 Multiphase Flow

This is the flow of a heterogeneous mixture containing two or more phases such as gaseous and liquid flows (121). Several types of multiphase flow exist: bubble, slug, transition and mist (122). The first type, shown by Figure 31, diagram one, is bubble flow. In this flow, there is a continuous liquid phase with evenly dispersed gas bubbles. Diagram two is representative of slug flow where irregular gas bubble has formed in the continuous liquid phase. As more irregular bubbles occur, the flow is represented by diagram three – known as transition flow and there is an approximately even split between the gaseous and liquid phases. Finally, diagram four represents the inverse of diagram one, mist flow. In this flow the gas phase is now continuous with the liquid suspended as a mist and a film on the wall of the tube/pipe.

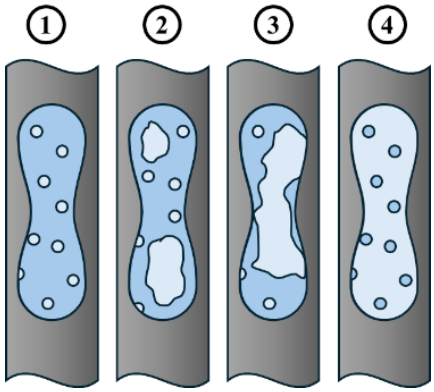

Figure 31: Different multiphase flow types. Adapted from (122).

3.6.2 Types of Flow Models

Various fluid flow models exist to cover the different scenarios and defect types. Three options have been considered in this work: orifice flow, capillary flow and the leak-before-break approach. Both single phase and two phase (gas-liquid) flows were initially considered though eventually the focus turned to purely gaseous flow through the crack.

The following section refers to the parameters of the defect, for clarity these are shown in Figure 32.

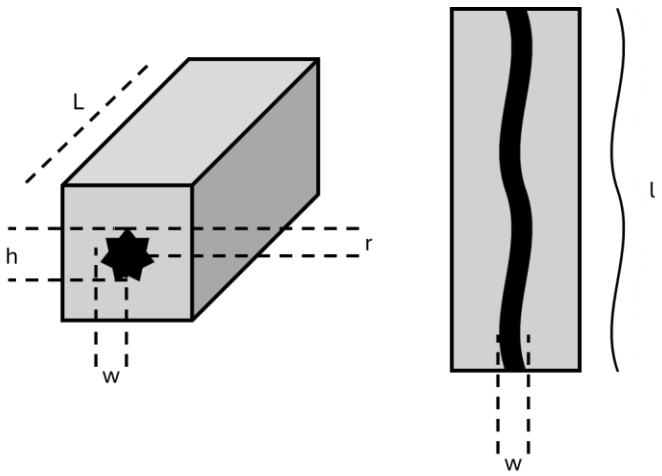

Figure 32: Key parameters of the crack shown in isometric and top down cross sectional views.

3.6.2.1 Orifice Flow

The simplest restriction to the flow of a fluid is a sharp edged orifice, such as the one shown in Figure 33. The British Standard for the calculation of the mass flow rate through such an orifice employs Bernoulli's equation where Q_m is the mass flow rate and C_d is a discharge coefficient (123).

$$Q_m = \frac{C_d}{\sqrt{1-\beta^4}} \cdot \varepsilon \cdot A \cdot \sqrt{2 \cdot \Delta P \cdot \rho} \qquad \textit{Eq. 10}$$

Where, during the flow under consideration there is no change in the phase of the fluid and that any liquid flow being considered, is above the vapour pressure of the liquid in question. An assumption is also made that the flow is isothermal, i.e. the temperature of the fluid across the orifice plate is constant. However, a process for considering a non-ideal gas and featuring a temperature change though this case is discounted as it is considered to not be relevant for this work.

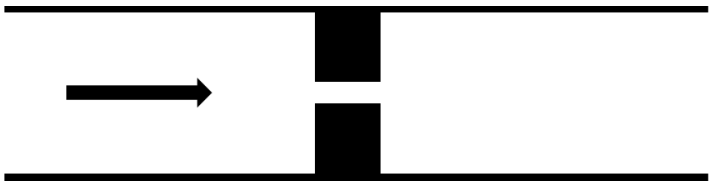

Figure 33: Schematic of a sharp edged orifice in a pipe.

One approach using the orifice equation as a starting point is set out by *Bomelburg* and is concerned with the flow of a perfect gas out of a closed container through a smooth, cylindrical hole in the wall (124).

In such a scenario, assuming that the system is adiabatic, then the mass flow rate through the hole is given by

$$Q_m = \alpha \cdot A \cdot \left(\frac{P_o}{P_s}\right)^{1/\gamma} \cdot \sqrt{\frac{\gamma}{\gamma-1} \cdot \left[1 - \left(\frac{P_o}{P_s}\right)^{(\gamma-1)/\gamma}\right]} \cdot \sqrt{2 \cdot g \cdot P_s \cdot \rho_s} \qquad \textit{Eq. 11}$$

Where, γ is the ratio of the specific heat capacities ${c_p}/{c_v}$.This can then be simplified to obtain an equation for the mass flow rate of:

$$Q_m = \alpha \cdot A \cdot \chi_{max} \cdot \sqrt{2 \cdot g \cdot P_s \cdot \rho_s} \qquad \textit{Eq. 12}$$

Where χ_{max} is given by

$$\chi_{max} = \left(\frac{2}{\gamma+1}\right)^{1/(\gamma-1)} \cdot \sqrt{\frac{\gamma}{\gamma+1}} \qquad \textit{Eq. 13}$$

It should be noted that while the diameter of the pinhole used in the work by Bomelburg - 100µm – is representative of the pinholes used in this work, the pressure used, a 70 atm starting pressure, is likely to mean the approach is unsuited to the situation being considered here. However, no limits are stated in the paper and the large pressure

differences between internal and external conditions is also found in the work presented here.

3.6.2.2 Capillary Flow

A capillary is defined as a very narrow tube with a bore passing through the length of the tube. Tubes of this sort are routinely used to admit a known flow of gas in order to calibrate vacuum equipment such as gauges (125). At the time of the paper by *Tison*, many models had been established to predict the flow through a metal capillary with flow rates as low as 10^{-8} – 10^{-14} mol s^{-1} however, as noted by *Tison* the validity has not been established. In the work by *Tison*, a 100 Pa or $9x10^{-4}$ atm. While this gives a large pressure difference between the internal and external pressure of 1000 times the starting pressure is not comparable to that which a vacuum drying set-up would create across the defect at the start of the process. *Ochert and Steckelmacher* have also considered the flow of a gas through a small capillary (126). In the article, an approach is presented which covers a range of capillary diameters which is on the lower end, and below the diameter of the cracks expected to be found in failed cladding – 0.2 µm to 10 µm with one end of the capillary at atmospheric pressure and the other assumed to be zero. However, despite the applicability of the equations based on the pressure range and size of capillary many of the terms in the equation are not defined in the literature.

A capillary flow model covering very large pressure ranges, with upstream to downstream ratios in the order of 1000 times with defects which are considered to be "not feasible to measure" is presented by *S. A. Tison* (127). However, despite large regions of the model fitting the experimental data well, there is a 40 % overestimation of the data at times. In addition, with the diameter of the capillary determined to be ~ 2 µm, this fell too far outside of the range of the pinhole discs and slits to be considered as a viable approach to use.

3.6.2.3 Leak Before Break

Leak before break is widely used within the nuclear industry and proposes that pipework will develop a leak before catastrophic failure occurs (128). This approach has been utilised by EDF Energy for the safety case at the Sizewell B PWR building on the R6 integrity assessment procedures. This approach has been utilised by EDF Energy for the safety case at the Sizewell B PWR building on the R6 integrity assessment procedures (129) As this approach is so prevalent in the industry, several computational

models exist to model the leak such as DAFTCAT, SQUIRT and PICEP however the underlying equations used could not be found in a search of the literature.

One approach, set out by *Chang et al*, considered is to treat the defect as a smooth orifice with the orifice area term being replaced with the crack opening area, A, with the volumetric flow, Q_v, through the crack given by (130):

$$Q_v = C_f \cdot A \cdot \sqrt{\frac{2 \cdot \Delta P}{\rho}} \qquad \textit{Eq. 14}$$

For an axial crack, a means of determining the opening area, A, is given relying on a shell parameter and the ratio of hoop stress to yield strength:

$$A = \frac{2 \cdot \pi \cdot P \cdot r \cdot \left(\frac{l_e}{2}\right)^2 \cdot \Omega}{E \cdot L} \qquad \textit{Eq. 15}$$

$$\Omega = 1 + 0.64935 \cdot \Lambda_e^2 - 8.9683 \times 10^{-3} \cdot \Lambda_e^4 + 1.33873 \times 10^{-4} \cdot \Lambda_e^6 \qquad \textit{Eq. 16}$$

$$\Lambda_e = \frac{\frac{l_e}{2}}{\sqrt{R \cdot L}} \qquad \textit{Eq. 17}$$

$$\frac{l_e}{2} = \frac{l}{2}\left[1 + \frac{\Phi}{2}\left(\frac{\sigma_{hoop}}{S_y}\right)^2\right] \qquad \textit{Eq. 18}$$

$$\Phi = 1 + 1.28987 \cdot \Lambda^2 - 2.6905 \times 10^{-2} \cdot \Lambda^4 + 5.3549 \times 10^{-4} \cdot \Lambda^6 \qquad \textit{Eq. 19}$$

$$\Lambda = \frac{l/2}{\sqrt{R \cdot L}} \qquad \textit{Eq. 20}$$

While providing good estimates of the leak rate through cracks, this model was determined to reliably overestimate the flow rate. This approach was also used by *Majumdar et al* to investigate the use of leak before break in stress corrosion cracking situations (131). However, in this work the calculation for the opening area was adjusted and calculated by:

$$A = \frac{2 \cdot \pi \cdot \frac{l_e}{2}^2 \cdot \Xi \cdot \sigma_{hoop}}{E} \qquad \textit{Eq. 21}$$

This approach, as with many of the models considered for this concept of flow rate modelling wraps up many of the terms that would be expected to be calculated and vital to the determination of flow rate into a term, in this case, Cf, the flow coefficient or a discharge coefficient, C_D, in this document. The means of determining this value are not

always well defined and this could be interpreted as a means of applying a fitting factor to the results. This is not an unexpected step however as with each crack being different in terms of the morphology, opening area, shape and surface roughness which would be nigh on impossible to calculate or determine in many cases.

The complex nature of crack pathways and the problem this presents when looking to model the gas flow through such a pathway was recognised by *Button et al.* who noted that by modelling the situation as an isothermal flow with a constant crack width then a more simplistic approach can be taken as the inability to define the pathway exactly will be a greater source of inaccuracy in the results (132). In order to provide validation for the model produced, *Button et al.* used parallel plates which had been sandblasted to introduce a surface roughness to the otherwise smooth surfaces. These plates were then held at various widths to create a rough channel for the gas to flow along. With the smallest crack width tested being recorded as 112 μm and the largest at 892 μm, the pinholes and the cracks formed by stress corrosion cracking would likely fall outside of the range for which this model has been tested. In addition, the crack length of 7cm as opposed to the few hundred microns that would be achieved through the AGR cladding or the material being used in this investigation. This issue of scale coupled with the fact that many of the variables used in the paper do not have their units defined and therefore it was decided to exclude the approach from consideration.

The model presented by *Baker et al*, also considers the flow between two parallel plates which were sandblasted to introduce frictional forces through surface roughness (133). While the work does look at smaller widths than those considered by *Button et al.* 40 – 100 μm wide, this is still on the upper end of the widths expected and it is acknowledged that, at the lower widths there is some deviation in the results when compared to the experimental data. Combined with the length of the parallel plates being used, this was deemed to be a model that would not be progressed as the cracks being assessed in this investigation were outside of the range this approach was validated against.

P. Gill et al, considered the problem of modelling the flow through complex pathways using an ordinary differential equation approach with the cracks being considered much more complex than the parallel plates considered in other sources (134). Unlike other approaches which consider only a rectangular crack opening area, the work by *Gill et al*, presents a model where ellipse or diamond openings are also considered. Additionally, the cracks being modelled are shown to have significant pathway deviation from the

straight channel and have widths close to the expected size of the crack to be produced in this work. A system of ordinary differential equations is provided:

$$\begin{pmatrix} \frac{\partial u_m}{\partial T} & \frac{\partial u_m}{\partial P} & -\frac{u_m}{v} \\ 0 & 1 & \frac{v}{u_m} \\ \frac{\partial h_m}{\partial T} & \frac{\partial h_m}{\partial P} & v \end{pmatrix} \begin{pmatrix} \frac{dT}{dz} \\ \frac{dP}{dz} \\ \frac{dv}{dz} \end{pmatrix} = \begin{pmatrix} \frac{u_m}{A} \cdot \frac{dA}{dz} \\ -\frac{P_f}{A} \cdot \tau_{wall} - \frac{1}{u_m} \cdot \frac{dF}{dz} \cdot \frac{v^2}{2} \\ \frac{P_f \cdot q_{wall} \cdot u_m}{A \cdot v} \end{pmatrix} \qquad \textit{Eq. 22}$$

While, from the results shown in the literature, this approach seemed to provide good agreement with data, extracting a useable form of the equations proved to be very difficult. Attempts were made to simplify the work and assume an isothermal flow, as done by *Button et al*, however this resulted in many terms collapsing to zero and no flow calculation being possible. It is also noted that the equation used by the DAFTCAT model is presented in this paper. However, with the units unclear and lacking the full approach taken by the program, including the ranges of both crack size and pressures, it was decided that it was not suitable to consider this model.

The final two sets of models considered here, by *Beck et al,* and *Taggart and Budden*, consider the impact of the crack morphology on the flow rate such as inertia, expansion and recirculation (135; 136) The model by *Beck et al*, is considered to be particularly applicable to the topic of this work as it explicitly covers crack widths as low as 10 µm and present different models to cover the crack at wider diameters as different resistive forces play an increased role. In the model by *Beck et al*, the overall volume flow rate, Q_v, given by

$$Q_v = v \cdot w_{eff} \qquad \textit{Eq. 23}$$

For the narrowest cracks considered, between 1×10^{-5} and 3×10^{-5} m wide, the velocity of the fluid is given by

$$0 = \frac{2 \cdot v}{\rho} \cdot \left[\frac{12 \cdot \mu \cdot l_{eff}}{w_{eff}^2}\right] - \Delta P \qquad \textit{Eq. 24}$$

In this regime, the flow is primarily influenced by the viscosity of the fluid. As the crack diameter increases to between 3×10^{-5} and 6×10^{-5} m, it becomes less tortuous and as a result the inertia pressure becomes important, with the velocity given by:

$$0 = \frac{\rho \cdot v^2}{2} \cdot \left[N \cdot 2 \cdot \theta \cdot \frac{w_{eff}}{d}\right] + \frac{2 \cdot v}{\rho} \cdot \left[\frac{12 \cdot \mu \cdot l_{eff}}{w_{eff}^2}\right] - \Delta P \qquad \textit{Eq. 25}$$

As the defect diameter is increased further to the region of $6x10^{-5}$ to 10^{-5} m the inertia forces are now considered to be minor, and the expansions and contractions of the fluid need to be accounted for resulting in the equation:

$$0 = \frac{\rho \cdot v^2}{2} \cdot \left[N\left(1 - \left(\frac{w_{eff}}{w}\right)^2\right)\right] + \frac{2 \cdot v}{\rho} \cdot \left[\frac{12 \cdot \mu \cdot l_{eff}}{w_{eff}^2}\right] - \Delta P \qquad \textit{Eq. 26}$$

Finally, for a crack opening area above $9x10^{-5}$ m, the flow becomes turbulent with the pressure losses experienced by the fluid almost entirely arises from the expansions and contractions giving a simplified equation for the velocity of

$$0 = \frac{\rho \cdot v^2}{2} \cdot \left[N\left(1 - \left(\frac{w_{eff}}{w}\right)^2\right)\right] - \Delta P \qquad \textit{Eq. 27}$$

Meanwhile, the approach used by *Taggart and Budden* calculates the mass flow rate using the equation:

$$Q_m = C_D \cdot (P \cdot \rho)^{1/2} \cdot \overline{w} \cdot L \qquad \textit{Eq. 28}$$

with the discharge coefficient, C_D, related to the sum of the pressure losses caused by friction, inertia and recirculation effects. Despite the applicability of the two models, some variables are still difficult to determine for a real crack such as the number of turns. Despite this drawback, the applicable range of crack size and pressure difference across the crack lead to the decision being taken to progress these models for comparison to the experimental data.

3.6.3 Other Approaches

Baker et al, rather than considering a crack as a capillary or orifice, considered the flow through two parallel plates (137). By taking into account the drop in pressure from friction with the walls, contractions, expansions and edge effects, the equation below was derived:

$$\Delta P = \frac{12 \cdot \mu \cdot l}{L \cdot w^3} \cdot Q_v + \frac{\rho \cdot C}{2 \cdot w^2 \cdot L^2} \cdot {Q_v}^2 \qquad \textit{Eq. 29}$$

To validate the model various shapes of cracks were produced: straight-through, “L” shaped and “S” shaped. However, as the cracks considered in this paper were on the order of mm width this was not considered to be a viable option for modelling the μm scale cracks we expect to find in the cladding should it have failed.

A second approach, used by *Hsieh et al* was to consider the flow of a gas along a microchannel (138).

The channel used in the investigation was 50µm deep, 200µm wide and 24,000µm. While the channel depth is potentially a suitable comparison to the dimensions expected to be found in an AGR fuel pin, the width and length are far beyond the expected conditions for a crack. Nevertheless, the approach is considered here for completeness as the pressure in the channel prior to the injection of the gas was 0.13Pa. This corresponds to the expected pressure of the system prior to the removal of the water vapour from the test sample.

$$Q_m = \frac{h^3 \cdot w \cdot P_o^2}{24 \cdot \mu \cdot l \cdot R \cdot T} \cdot [P^2 - 1 + 12 \cdot \psi \cdot K \cdot (P - 1)] \qquad \textit{Eq. 30}$$

Using the Darcy friction factor good agreement with experimental data was established though a slight overestimation of the flow is obtained.

3.7 Water in the Vacuum Drying Process

3.7.1 Boiling and Evaporation

Evaporation is the process by which a liquid undergoes a phase change into its vapour at a temperature below the temperature at which the liquid would boil (139). In order for a molecule of the liquid to evaporate, it must possess enough kinetic energy to overcome the effects of the intermolecular forces which are present in the liquid.

Boiling, on the other hand occurs when all the molecules in the liquid possess enough kinetic energy to vaporise and occurs when the vapour pressure of the liquid is equal to the external pressure. By reducing the external pressure it is therefore possible to reduce the temperature at which a liquid boils at. For example, water boils at 100°C, however, if the pressure is reduced to 0.1 BarA (i.e. a tenth of normal atmospheric pressure) then the boiling point falls to just 45.6°C (140).

3.8 Summary

Multiple methods exist for producing corrosion cracks in a metal sample with all showing the ability to produce dendritic stress corrosion cracks. After assessing the different options and in consultation with the technical staff at the University of Leeds it was decided that the drop evaporation technique was the most simplistic to undertake as it required the minimal amount of set up compared to the immersion processes. The DET method also allows for the visual examination of the sample while a test is being

conducted which is important in this work as the aim is not to cause catastrophic failure but to induce initial cracking and then end the test.

In terms of the fluid flow modelling, there are many different models which are in use to determine a flow rate through narrow cracks. However, in many of the sources found in the literature the units were not stated which meant these approaches were not considered as validation of the code would not have been possible prior to modelling the vacuum drying. Furthermore, other methods rely on the use of computational fluid dynamics. These modelling approaches, while very accurate would have been very time consuming to produce and potentially would require a new pathway to be calculated and produced for each defect being examined in order to ensure a good flow rate was calculated. Other approaches, such as the ordinary differential equation approach set out by *Gill et al*, were initially promising but it was not possible to manipulate the equations in such a manner that the flow rate was a calculable variable. Attempts were made to reduce the complexity by assuming isothermal flow however this resulted in many terms collapsing to zero and consequently a flow rate of zero was calculated. In the end three methods were chosen to progress: *Bomelburg* which considers flow of gas from a high pressure container through a small, smooth, circular defect into a lower pressure environment in a modified orifice flow format and the approaches by *Beck et al*. and *Taggart and Budden.* Both of these methods use the Leak-before-break principle and consider the various frictional forces such as surface roughness and tortuosity.

4 Corroding Stainless Steel Samples

This chapter will focus on the means by which a corrosion crack was produced in stainless steel. It covers the material tested and the techniques implemented in the pursuit of a representative crack before discussing the methodologies of the various approaches. Finally the results of each of the techniques are presented and discussed.

4.1 Experimental Work

This section will set out the work undertaken to produce defects in samples of stainless steel. It covers the test materials, the design of the set-ups and the methodology used.

4.1.1 Test Material

The stainless steel used for the AGR fuel cladding is known as 20/25/Nb and is extremely corrosion resistant, therefore it was decided that a stainless steel with a lower corrosion resistance would be used as a surrogate material. Thus, 304 stainless steel was chosen as the desired test material, with 316 stainless steel considered as an option should the method prove successful.

Sheets of 0.4 mm thick 304 stainless steel were ordered from RS Pro and subsequently cut into 260 mm x 30 mm strips in house. Following this the strips were washed in acetone followed by cleaning in a 3MX ultrasonic cleaner to remove any surface contamination such as oils or grease which may have been left over from the cutting process or manual handling.

After several corrosion experiments were conducted it was noted that less corrosion than anticipated was occurring and this prompted an investigation into the composition of the 304 stainless steel purchased from RS Pro. EDS of an offcut from one of the unused strips of RS Pro supplied stainless steel was analysed with the results shown in Table 5. The results of the EDS showed the presence of molybdenum which should not be found in 304 stainless steel. Molybdenum is added to increase the corrosion resistance of the alloy, when added to 304 stainless steel, it is reclassified as 316 stainless steel (141). The sample of RS Pro stainless steel was also analysed by the University of Lancaster in order to confirm the presence of molybdenum. This finding explained the lower than expected corrosion. After this analysis, two strips of 304 stainless steel, confirmed by EDS, were sourced from the University of Leeds' workshop and subject to the corrosion testing discussed in 4.1.2.

Table 5: Refence compositions of 304 and 316 stainless steel taken from Thyssenkrupp Materials along with the composition of supposed 304 stainless steel purchased from RS-Pro (44) (45).

Stainless Steel Grade	304 (wt. %)	RS Pro (wt. %)	316 (wt. %)
Carbon, C	0.07	-	0.07
Chromium, Cr	17.50 - 19.50	16.0	16.50 - 18.50
Manganese, Mn	2.00	1.0	2.00
Molybdenum, Mo	-	1.7	2.00 - 2.50
Nitrogen, N	0.1	-	0.10
Nickel, Ni	8.00 - 10.50	8.8	10.00 - 13.00
Phosphorus, P	0.045	-	0.045
Sulphur, S	0.015 - 0.03	-	0.015
Silicon, Si	1.00	0.70	1.00
Iron, Fe	Balance	59.9	Balance

4.1.1.1 Thermal Treatment

To degrade the corrosion resistance of the stainless steel the samples were thermally treated. Two strips at a time were placed into a Carbolite chamber furnace having first been washed in acetone and cleaned in deionised water using an ultrasonic bath. A range of temperatures and durations were used to explore the effect of the thermal treatment on the corrosion of the samples. The samples were heated to the desired temperature and held there for pre-determined duration before furnace cooling back to room temperature. The breakdown of the conditions each sample was subjected to can be found in Table 6, Table 7, Table 8, Table 9, Table 10.

4.1.1.2 Surface Treatment

While in the furnace, a protective oxide layer forms on the surface of the stainless steel which needed to be removed prior to any degradation technique being undertaken in order to expose the surface. Two methods were utilised for this process, the first using sandpaper and the second using a shot blasting process.

<u>Hand Sanding:</u>

Successively finer sandpaper was used to remove the oxide layer from the sample. Starting with P240 to remove the bulk of the oxide layer before progressing to P400, P800 and P1200 which removed the remaining oxide. A mirror finish was not aimed for

or achieved as the scratches present from the sanding process were, it was hoped, possible initiation sites for corrosion as stagnant solution could build up there.

Shot Blasting:

With the hand sanding approach proving to be effective but time consuming, a quicker method was sought. It was recommended that the shot blasting equipment be utilised. Shot blasting involves propelling high velocity plastic pellets at the sample in a similar approach to sandblasting.

While this approach removes the oxide layer which builds up during the thermal treatment process, it results in the surface of the sample becoming rough and uneven. As many forms of corrosion require regions of stagnant solution this was not perceived to be a detriment to the experiments being conducted, it ultimately made the analysis of the samples more arduous as corrosion damage was not as visible when compared to the hand sanded samples. A further drawback which was not anticipated until after all the shot blasting had been completed was the cold working which the material underwent as a result of the process, resulting in compressive stresses being imparted on the sample (142).

4.1.2 Drop Evaporation Technique

4.1.2.1 Development of the Testing Rig

Work conducted previously in this field utilised an adapted form of the four-point bend test, such as the one used by *Pereira et al*, whose set up is shown in Figure 34. In this arrangement the inner loading points are raised up into the sample which induces the stress once contact is made between the sample and the outer loading points. This leaves the sample exposed for easy observation and delivery of the corrosive media, however, the rig must be placed into an oven, as there is no heating of the sample directly.

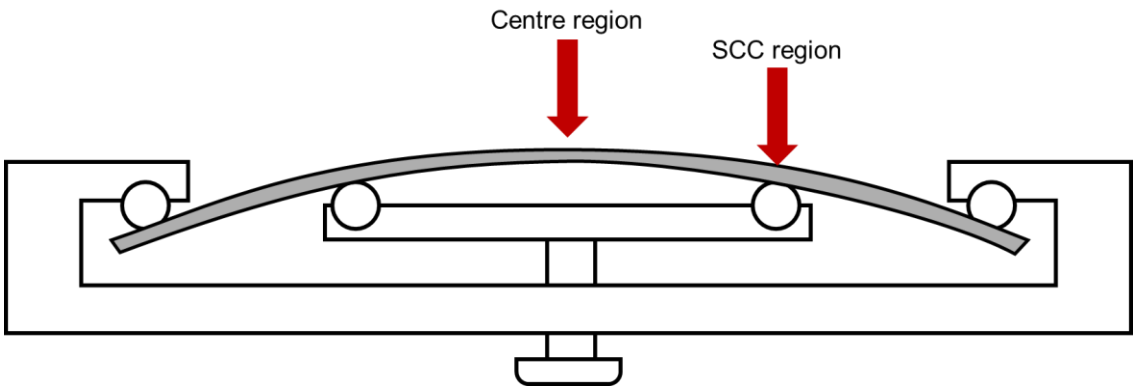

Figure 34: Schematic of the set-up used by Pereira et al (143). Adapted from the reference for clarity.

To adapt the approach for the work conducted in support of this thesis, the decision was taken to adapt the design. Figure 35 shows the changes made. In this version of the rig, the inner loading points are static and the outer points can be lowered to induce stress on the sample. This increases the access to the sample with regards to the implementation of heating however it comes at the cost of easy access to the point of maximums stress. To rectify this the screw used to lower the loading points features a bore through the full length, through which a section of tube can be placed to ensure delivery of the corrosive media. Figure 36 shows a photo of the final rig produced for this work.

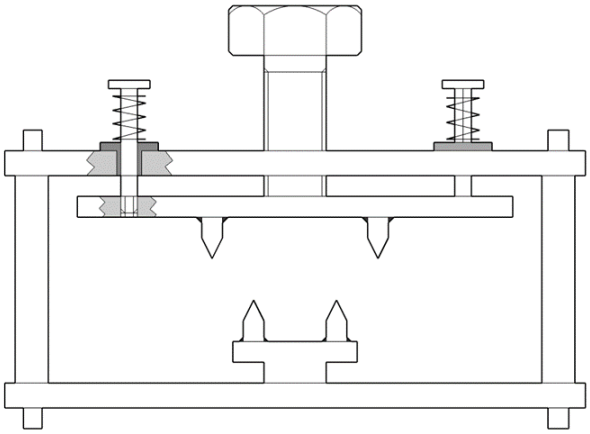

Figure 35: Schematic of the rig used for the drop evaporation work conducted for this thesis.

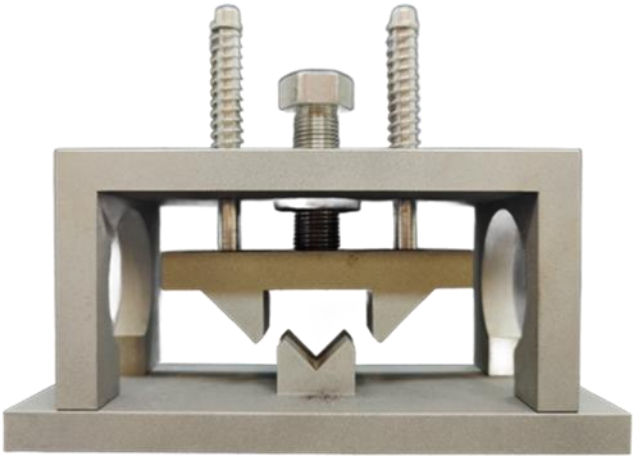

Figure 36: A photograph of the finished drop evaporation rig used for this work.

4.1.2.2 Heating the Sample

In order to provide heating to the sample various approaches were considered. The first option was to utilise resistive heating as had been done in literature. However, this was ruled out due to the health and safety risks involved. Secondly various heating sources were trialled such as heating a copper rod which was placed into contact with the centre

of the sample and using heating pads directly on either end of the sample. These pads were placed away from the dripping site in order to allow for the wiring and pads to be kept dry and prevent any electrical risks. However, in testing it was found that both of these methods were insufficient to provide a suitable transfer of thermal energy to the sample with the test region remaining cool to the touch after over an hour of heating. Finally, two cartridge heaters were placed into brass blocks and taped to the underside of the sample and positioned against the lower loading points. These brass blocks provided excellent thermal conductivity and a large surface area ultimately proving sufficient in transferring the thermal energy to the centre of the sample with a diagram of the arrangement shown in Figure 37.

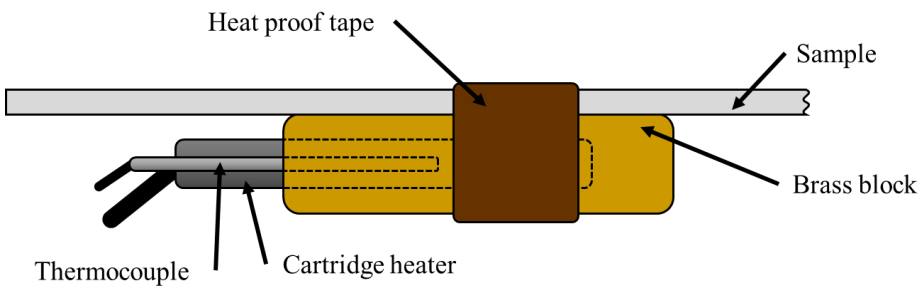

Figure 37: Diagram of the set up used to heat the sample for the drop evaporation tests conducted in the rig.

During experiments, the set-up was found to fray and degrade rapidly often causing an abrupt end to the test as wires frayed and ultimately the heaters short-circuited. This was rectified by the addition of a heat-resistant sheath over the wires connecting the heaters to the controllers.

4.1.2.3 Methodology for Automated Drop Evaporation Rig

A strip of stainless steel is selected and washed to remove any surface contamination. Initially this is achieved by a wash in acetone followed by further cleaning in an ultrasonic bath. Following this the sample is dried with a paper towel before being inserted into the rig. Care is taken to ensure that there is minimal contact between the loading points and the sample to minimise the formation of surface defects such as scratches.

Once the sample has been positioned, the brass block is held in place and the heat proof tape applied to attach the block to the sample. To ensure the centre of the sample is sufficiently heated, it was decided that the brass block should be adjacent to the lower loading points. The upper loading points are then lowered and the desired deflection and therefore stress is applied to the sample.

To deliver the corrosive solution, a four litre container is filled and placed at an elevated location adjacent to the rig with the reservoir connected to a peristaltic pump. Tubing is connected to the outlet of the pump and fed down through the bore in the screw to allow for the solution to be delivered to the centre-point of the sample.

Once this is all in place, the cartridge heaters are turned on and the sample left to reach the desired test temperature - 180°C for these tests – which was confirmed by an infrared thermometer. Then the peristaltic pump is switched on and the corrosive solution delivered one droplet at a time to the sample.

The sample is regularly checked to ensure that catastrophic failure has not occurred and to ensure that the solution reservoir does not run dry throughout the test.

To cease the testing, either due to observation of corrosion which warrants examination or after a predetermined duration has elapsed the pump is switched off and the tubing extracted from the rig. Additionally the heaters are turned off and the sample left to cool. Following this any salt build-up is removed using mechanical, manual techniques taking care not to damage the surface. Any deposit which is adhered to the surface is removed by hot water and/or a wash in the ultrasonic bath.

4.1.2.4 Second Generation of Drop Evaporation Test Rig

Once the technique had been shown to be effective at corroding samples of stainless steel, a second, refined version of the design was commissioned. This design incorporated elements of the original design as well as some improvements arising from experience operating the first generation of the rig. However, the basic operational premise remained the same. Modularity was also brought back into the design with a second set of lower loading points and side supports manufactured to allow for increased deflection to be applied should it be desired.

4.1.2.5 Operational Issues with the Design

The original design set out a modular design that would allow for easy adjustments to be made to improve ability of the rig to conduct tests. For example, the workshop made unapproved alterations to the design in order to simplify the construction process. Rather than keep the open sided design originally presented (and shown in Figure 35), a circular hole was cut into the side for the sample to be passed through. This resulted in the samples being unable to sit on the lower loading points and time was lost while this was rectified. Additionally, the dowels which were added to prevent the upper loading

points from dropping onto the surface of the sample and to prevent twisting of the component during operation were not attached to the component as specified.

The build-up of salt during the operation of the rig was also another issues. As shown in Figure 38 over the course of three weeks a substantial mass of salt – NaCl in these photos – which obscured the view of the sample. This was not unexpected as various literature sources had noted the formation of a "salt volcano" and indeed had theorised that the salt could lead to a crevice corrosion cell forming between the salt and the sample surface.

Figure 38: The build-up of salt on and around the rig after during operation of the DET rig after 7 days, 14 days and 21 days.

Other changes made impacted the operation of the rig, such as the decision taken unilaterally by the workshop to change to using 304 stainless steel for several components rather than the requested 316 stainless steel. This resulted in several components undergoing corrosion and becoming stuck and risking damage to the samples when trying to extract them for analysis, such as the pylon, as shown in Figure 39. With the build-up of salt, as shown in Figure 38, exacerbating the problem. This was later rectified in the construction of the second rig as well as with new components for the first rig.

Figure 39: Corrosion of one of the pylons found on the first generation drop evaporation rig. Acquired on the stereomicroscope using the 1.25x lens for a total magnification of 12.5x.

During one experiment a large mass of brown “sludge” was observed to have pooled in the bund, this is shown in Figure 40. This was unique to the test conducted with MgCl2 at a concentration of 35 g/L. Initially the test was promising with a salt build up similar to the other tests (see Figure 50) however, once the sludge was noted the test was halted due to the source seemingly being the brass heating block and the cartridge heater and concerns for a severe electrical failure. This substance is discussed in more depth later on (see Section 4.2.2.2).

Figure 40: A portion of the unknown brown sludge which formed during one of the drop evaporation tests conducted using the automated rigs.

4.1.2.6 Adaption to the Constantly Wetted Approach

Following the repeated electrical issues and the generation of the brown sludge it was decided that an alternative, more reliable method would be required. The solution devised was to add the droplets manually and utilise a drying oven to heat the sample and evaporate the solution thereby concentrating the solution in a similar manner to that achieved with the automated rig. This approach was inspired by the work of *Drugli and Steinsmo* who noted that while the target for the drop evaporation technique is to allow the previous droplet to evaporate, this was very difficult to achieve and usually resulted in pools of liquid forming on the sample.

4.1.2.7 Methodology for the Constantly Wetted Approach

In this approach the samples are manually deflected and then tape applied to maintain the stress for the test duration. Tape was also added at points either side of the centre to help provide a bounding region for the solution and prevent it flowing off to either side. Following this, the sample is placed on a bund in a drying oven set to 65°C. Droplets of the corrosive solution were then added using a pipette and the sample was left undisturbed, in a fashion seen in Figure 41, with periodic checks to ensure solution was still present.

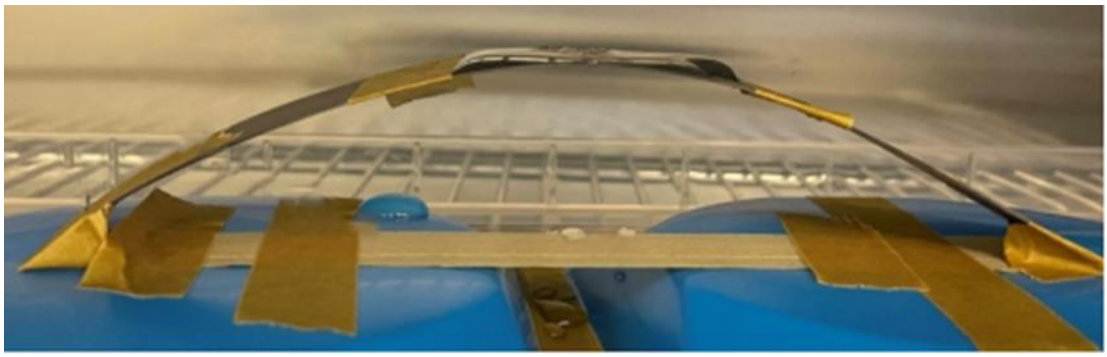

Figure 41: An image of a sample undergoing corrosion testing using the constantly wetted approach.

New solution was added periodically and it was also necessary to break the salt layer which formed across the surface of the solution in order to ensure evaporation and therefore concentration of the solution continued throughout the experiment.

As with the automated rig, once the test had been completed, or if the sample was extracted for interim analysis, the salt had to be removed. This was achieved by an initial wash in tap water followed by an ultrasonic bath for 30 minutes at 37 kHz. This removed the vast majority of salt from the sample although some residue was found in pits.

4.1.3 Potassium Tetrathionate

4.1.3.1 Methodology

<u>Unstressed Samples:</u>

Strips of 304 stainless steel were acquired from the University of Leeds workshop and tested via SEM-EDS to confirm the composition. These samples were then placed in a furnace at 650°C for a range of dwell times; 5 hours, 12 hours, 24 hours, 36 hours, and 48 hours before being furnace cooled. Samples of the stainless steel that were not thermally treated and mild steel were also tested. After sanding the thermally treated samples to remove any oxide layer that had formed, samples were cut, placed into falcon tubes and submerged in the solution of 0.1 M potassium tetrathionate which had been acidified to pH 2 with the addition of sulphuric acid with an example falcon tube shown in Figure 42.

Figure 42: One of the falcon tubes containing a sample of sensitised 304 stainless steel being exposed to the 0.1 M potassium tetrathionate which has been acidified to pH 2 with the addition of sulphuric acid.

Six different batches of samples were generated with each batch remaining submerged for a different duration. The tested durations were: 24 hours, 72 hours, 144 hours, 192 hours and 240 hours. After the experimental duration was over, the samples were removed from the solution and washed in tap water to remove any residual solution before being left to dry in the drying oven at 65°C before being examined under a microscope for signs of corrosion.

4.2 Results and Discussion

4.2.1 Potassium Tetrathionate

All of the samples tested were analysed using the Olympus SZX10 Macro Stereo Microscope to look for any signs of corrosion occurring on the sample surface due to the speed at which this microscope can be operated and the flexibility afforded by the external lighting which allows for surface features to be identified quickly and efficiently.

After 24 hours exposure to the solution, there were no signs of corrosion present on any of the samples of stainless steel however the mild steel sample showed signs of corrosion damage with the extent of corrosion increasing as the duration of the experiment increased. This is shown in Figure 43.

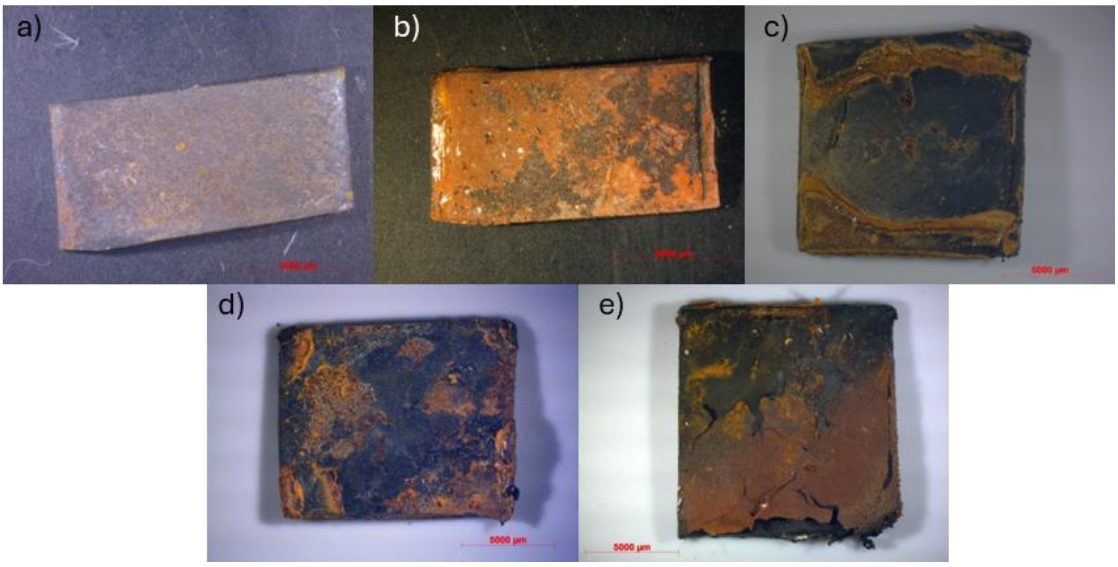

Figure 43: Corrosion damage to the samples of mild steel exposed to the 0.1 M potassium tetrathionate which had been acidified to pH 2 with sulfuric acid. a) 24 hours b) 72 hours c) 144 hours d) 192 hours e) 240 hours.

In contrast, none of the stainless steel samples showed any signs of corrosion occurring at any test duration and after any of the dwell times used. Figure 44 shows the sample which was held at 650°C for 48 hours as this was deemed to be the most likely sample of 304 stainless steel to corrode however, no corrosion was observed.

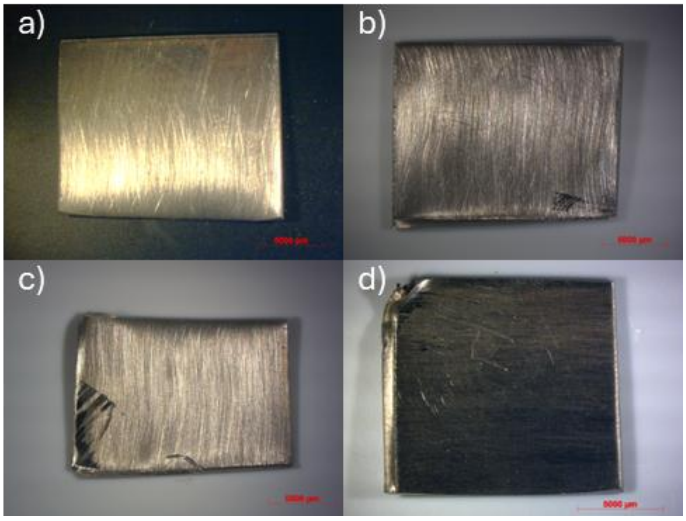

Figure 44: Samples of 304 stainless steel thermally treated at 650C for 48 hours and left to furnace cool. These samples were also hand sanded to remove the oxide layer that had formed prior to immersion in the acidified potassium tetrathionate for: a) 72 hours b) 144 hours c) 192 hours d) 240 hours

4.2.2 Automated Drop Evaporation Technique

Initial testing was conducted using the rig set up described in section 4.1.2. Once the testing with this rig was halted due to the concerns about the repeated electrical issues

and the production of the brown sludge, the constantly wetted approach was utilised and developed with assistance from *A. Prior* (144).

4.2.2.1 Sodium Chloride

Initial tests, including the commissioning trails (indicated by the sample ID:C1 and sample ID:C2) were conducted using sodium chloride at a concentration of 35 g/L. An overview of the conditions used for these initial commissioning tests is set out in Table 6. These initial tests on samples ID:C1 and ID:C2 were performed as a means to test the operation of the rig and its safety when operating unsupervised overnight and at weekends. Testing of sample ID:C1 was undertaken intermittently from 09:00 till 17:00 for a week.

Table 6: Summary of experimental conditions for the NaCl tests using the automated rig.

Sample ID	Thermal Treatment		Surface Finish	Experimental Conditions		
	Temperature (°C)	Duration (hours)		Temperature (°C)	Concentration (g/L)	Duration (hours)
C1	-	-	AR	180	35	168
C2	-	-	AR	180	35	216
S1	600	5	AR	180	35	168
P1	600	5	AR, 5P	180	35	168

Figure 45 shows the result of the ID:C1 test which, despite the limited running, produced evidence of corrosion with an orange-brown deposit which was not removed by washing in water or acetone, along with a single 50 µm diameter pit in the centre of the sample. This gave confidence that the method would be suitable for producing corrosion damage to the samples.

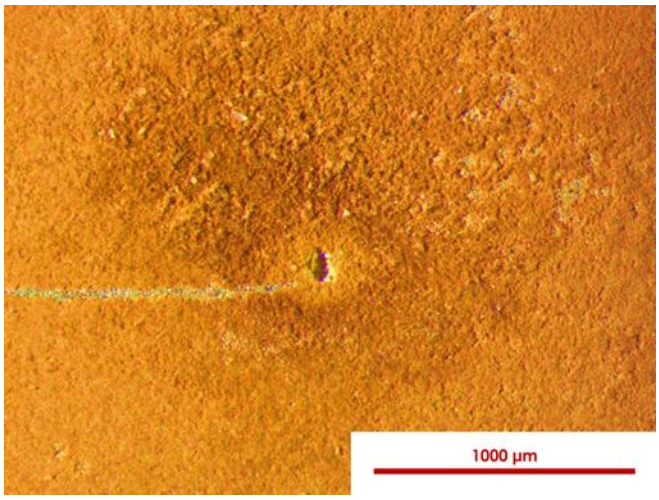

Figure 45: Sample C1 which was held under stressed conditions for 168 hours with 35 g/L NaCl dripped onto the sample from 09:00 to 17:00 for a week producing a 50 µm diameter pit shown here.

Following this, sample ID:C2 was tested under similar conditions however, this sample was allowed to remain under the full experimental conditions for the full duration without supervision. However, despite the increased run time there was no signs of corrosion observed on the surface of the sample and the orange-brown deposit seen in Figure 45 was not present.

Thermally treated samples where then subjected to the drop evaporation process. Sample S1 was heated to 600°C in a furnace and left to dwell for 5 hours before furnace cooling back to room temperature. The oxide layer was left intact for this test with the sample tested for a week exposed to the same 35 g/L NaCl solution as samples ID:C1 and ID:C2. As with the sample ID:C2, no deposit was observed on the surface of the sample and no corrosion damage occurred around the centre point of the sample. However, in the region around the loading points cracking and pitting was observed. Cracking did occur on this sample and using the confocal microscope it was possible to obtain topographic data for the region of interest with the results of this shown in Figure 46 and Figure 47.

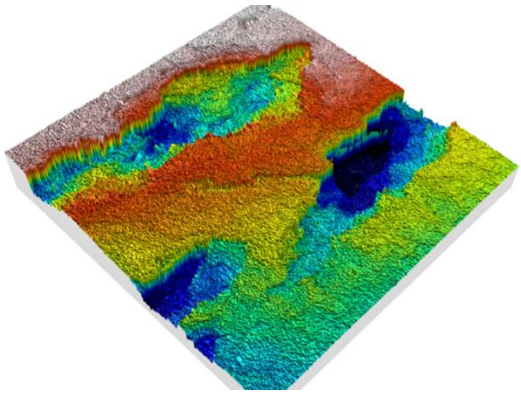

Figure 46: a 3D view of the pits generated in sample S1 found in the region around the loading point. The data was gathered using the 50x magnification, 0.6 lens on the CLSM.

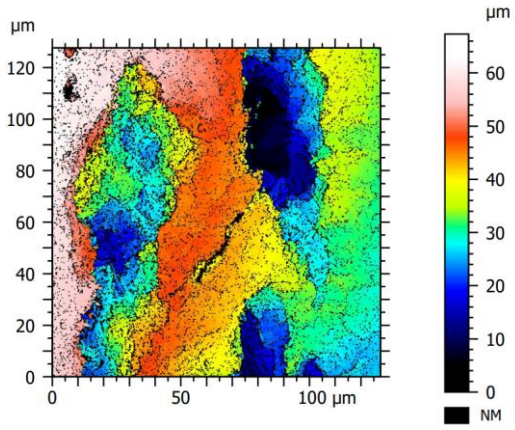

Figure 47: A 2D topographic view of the same region shown in Figure 46.

These images showed that the cracks were not deep and were connecting the different pits rather than penetrating through the thickness of the material. Nevertheless, further encouragement was gathered from this test as it showed pits reaching approximately 60 µm into the sample though an exact depth is not possible to determine from this view.

In order to artificially create the regions of stagnant solution required for pitting and crevice corrosion which could potentially initiate SCC, a centre punch was used to create five marks in the surface prior to exposure to the corrosive environment. There was no corrosion observed in any of the five centre punch marks which was attributed to the work hardening effects of the punching process. However, as shown in Figure 48, cracking occurred at the location where the sample is bent and in contact with the rig framework. Therefore it was concluded that galvanic or crevice corrosion may have been the driving mechanism which produced these cracks.

Figure 48: A z-stack of the sample P1showing the edge of one of the centre punch marks found near the loading points. Taken using the 10x magnification 0.4 lens on the CLSM.

Corrosion pits were also observed to have formed on the edges of the sample, well away from the points of contact with the rig ruling out crevice corrosion as the driving mechanism. These pits are shown in Figure 49 along with a depth profile through the deepest point according to the CLSM which was recorded as approximately 150 µm.

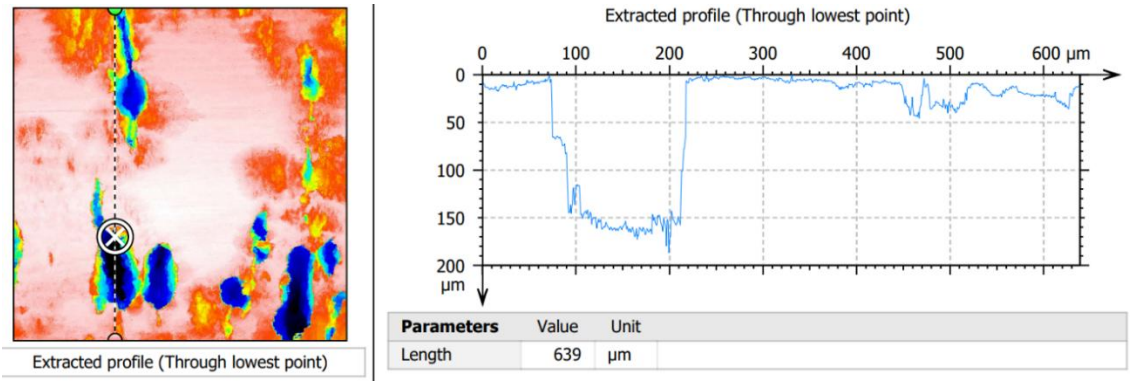

Figure 49: The topographic scan and depth profile of the corrosion pits which formed on the edge of sample P1.

It was hoped that observation of the sample would be possible in order to spot any corrosion which was occurring and prevent catastrophic failure of the sample from occurring. Unfortunately this was not possible with the NaCl tests due to the vast quantity of salt which accumulated around the rig, shown in Figure 50.

Figure 50: A series of pictures showing the build-up of NaCl on the rig over the course of an experiment after: a) 7 days b) 14 days and c) 21 days.

4.2.2.2 Magnesium Chloride

After initial tests on samples ID:C1, ID:C2, ID:S1 and ID:P1 showed promise, it became clear that there was a need to accelerate the corrosion rate. Therefore magnesium chloride was chosen instead of NaCl. In theory, this would result in the corrosive solution being more aggressive owing to the two chloride ions per molecule.

Initial testing using sample 1 was conducted using a sample that was not thermally treated to allow for a comparison to samples ID:C1 and ID:C2. After 168 hours, a brown sludge like material was noted to be pooling in the bund and sand bed with this shown in Figure 40. After continued observation and noting that the quantity of the sludge was increasing the test was halted after 216 hours as concerns were raised given the origin of the sludge appeared to be from near one of the heaters.

Table 7: Summary of the experimental conditions for the MgCl2 tests conducted on the automated rig.

Sample ID	Thermal Treatment		Surface Finish	Experimental Conditions		
	Temperature (°C)	Duration (hours)		Temperature (°C)	Concentration (g/L)	Duration (hours)
1	-	-	HS	180	35	216

A sample of the sludge was taken and EDS performed in order to determine the composition and a possible source of the material.

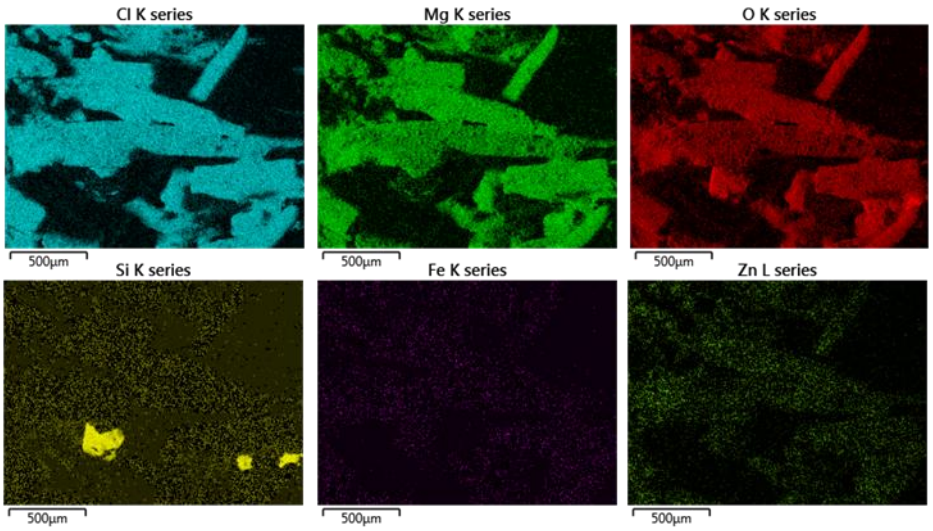

Figure 51: EDS analysis of the mystery material showing the distribution of the main elements detected.

The EDS analysis of the material detected six main elements, chlorine, magnesium, oxygen, silicon, iron and zinc with a large amount of the first three (Cl, Mg and O) as

shown by the large signals for these elements in Figure 51. These are hypothesised to have come from the heat-proof tape, the rig and the sample and the brass block. One possible explanation for the material is that a magnesium oxychloride had been produced, also known as sorel cement. It is noted that this would require a high temperature environment, above that which the heaters were rated for. However, the heaters were observed to have glowed red as seen in Figure 50b. As a result it is theorised that the $MgCl_2$ solution came into contact with the heaters and corroded these potentially exposing the core. The examination of this was not taken further however as the decision was made to cease operating with this approach and the determination of the material's composition was not relevant to this work.

The sample under investigation at this time, ID:1, described in Table 7, was removed from the rig and carefully washed in deionised water as it was clear from a visual examination that significant corrosion had occurred and the sample had potentially undergone catastrophic failure with a substantial crack visible and shown in Figure 52. Unlike the NaCl tests, the bulk of the corrosion on sample ID:1 was observed to have occurred on the underside of the sample with crevice corrosion deemed to be the likely mechanism. Galvanic corrosion is also suspected to have been a factor with the stainless steel being less noble than brass and therefore corroding at an increased rate.

Figure 52: Sample ID:1 after gentle cleaning in deionised water. The significant corrosion damage is visible with a crack circled.

Upon removal of the heat-proof tape, the sample split into two sections around the crack marked in Figure 52. The edges of these two sections were analysed using the Olympus BX51 microscope, with two images shown in Figure 53 which show further cracking having taken place.

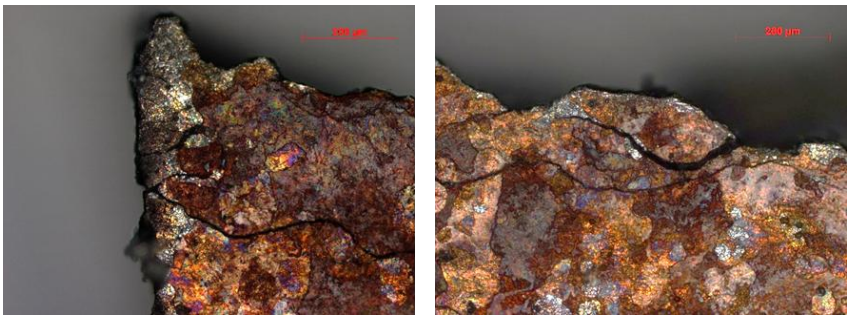

Figure 53: Images of cracks near the failure surface of sample ID:1 showing the corrosion damage. Taken at 10x magnification on the Olympus BX51 microscope.

Further examination using SEM was also conducted with several of the images gathered shown in Figure 54. The images show cracking propagating from the top surface of the sample through the full thickness of the material when viewed at a 45° angle (Figure 54a and Figure 54d) however, these cracks were too close to the edge of the sample and therefore a suitable test piece for vacuum drying could not be manufactured from the sample. In Figure 54b, a crack was imaged which measured approximately 5 µm wide which is within the size range expected for SCC cracks in AGR cladding. However, unlike the predicted cracks, this crack appeared to be transgranular in nature rather than intergranular.

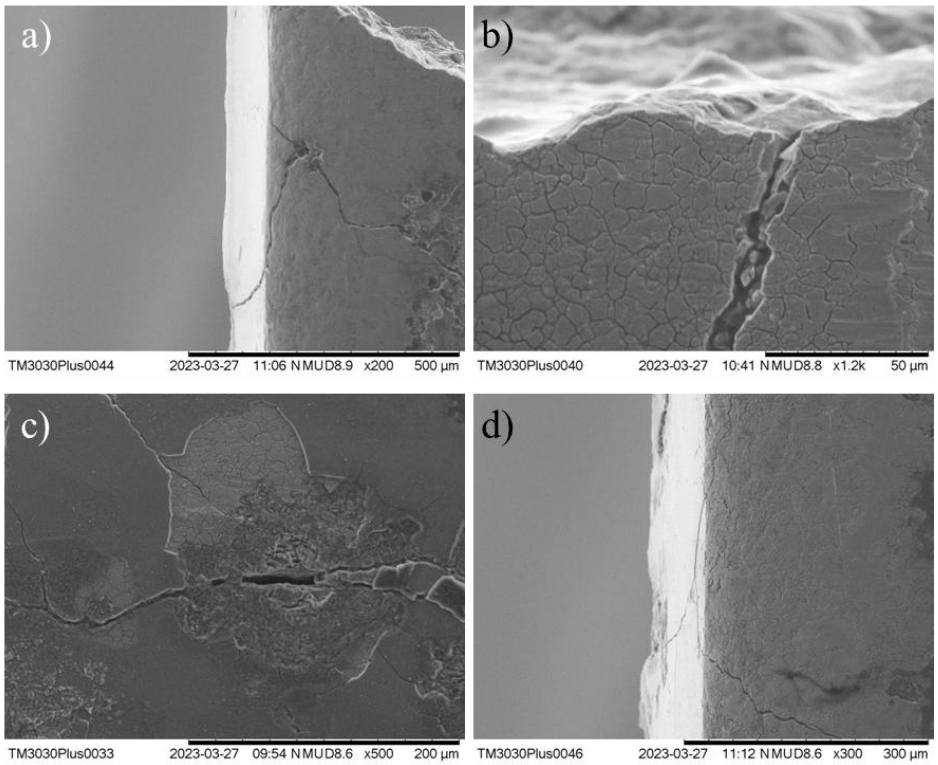

Figure 54: SEM images of microcracks detected on the sample 1 after nine days exposure to 35g/L MgCl2. a) Crack from the surface through the depth. b) Trans-granular crack from the failure edge. c) A crack initiated in a local corrosion region. d) Part of a crack network from the surface through the material.

4.2.3 Manual Drop Evaporation Technique

With the automated drop evaporation rig experiencing faults an alternative method was developed and set out in sections 4.1.2.6 and 4.1.2.7. Only key results will be presented here with the test conditions outlined in Table 8.

Table 8: Summary of experimental conditions for the $MgCl_2$ tests corroded using the constantly wetted method.

Sample ID	Thermal Treatment		Surface Finish	Pre-Treatment	Experimental Conditions		
	Temperature (°C)	Duration (hours)			Temperature (°C)	Concentration (g/L)	Duration (hours)
2a	600	5	HS	-	65	380.8	1776
3a	650	12	SB	-	65	380.8	1488
4a	650	48	SB	-	65	380.8	888
5a	650	5	SB	-	65	380.8	1344
6	950	0.5	HS	- ET	65	380.8	336 432
2b	600	5	SB	-	65	380.8	432
3b	650	12	SB	-	65	380.8	432
4b	650	48	SB	-	65	380.8	432
5b	650	5	SB	-	65	380.8	432
7	650	24	SB	-	65	380.8	432
8	650	36	SB	-	65	380.8	432
9a	950 700	2 70	HS	10P, ET	65	380.8	432
9b	950 700	2 70	HS	ET	65 65	380.8	432
10a	-	-	AR	ET	65	380.8	432
10b	-	-	AR	ET	65	380.8	432

The bulk of tests were undertaken using the RS Pro stainless steel, the composition of which is set out in Table 5. All of the samples were thermally treated by heating in a furnace at the temperature and for the dwell time shown in Table 8 before being left to furnace cool. Four of the samples (ID:2a, ID:6, ID:9a and ID:9b) were subject to the hand sanding process in order to remove the oxide layer that built up during the thermal treatment. Initially P240 grade sandpaper was used before progressing to P400, P800 and P1200 grades. The other samples, except for ID:10a and ID:10b, where shot blasted to remove the oxide layer. Samples ID6, ID9a and ID9b were also etched with a 40% $FeCl_3$ etchant for 15 minutes to ensure the removal of the oxide layer.

Sample ID:2a

The first sample analysed, sample ID:2a, was heat treated by placing the strip into a furnace at 600°C for five hours before being allowed to furnace cool. The hand sanding procedure was used to remove the oxide layer and was ultimately subjected to the constantly wetted technique for 1776 hours in total using 380.8 g/L $MgCl_2$. After 336 hours the sample was removed from the drying oven and cleaned in water and acetone for examination. A pit was observed and measured using the CLSM to be approximately 50 µm deep. The sample was then returned to the drying cabinet for a further 336 hours at which time it was cleaned and returned to the microscope for analysis. This time, little extra corrosion was observed in the initial pit however a second pit had developed with the CLSM scans indicating a depth of approximately 100 µm. The lack of further corrosion occurring in the original pit was attributed to the passivation of the pit surface and therefore it was decided that samples would be left under test conditions for the full duration unless extensive corrosion was observed.

After the test duration had elapsed the sample was washed using tap water to remove the bulk of the remaining solution before being paced in a 3MX ultrasonic bath at 37 kHz for 30 minutes to remove any salt or solution from pits or cracks which may have developed. Examination using the CLSM revealed that the second pit, which was originally 100 µm deep had corroded further and now was now measured to have a depth of approximately 150 µm. This pit is shown and as a topographic scan in Figure 55.

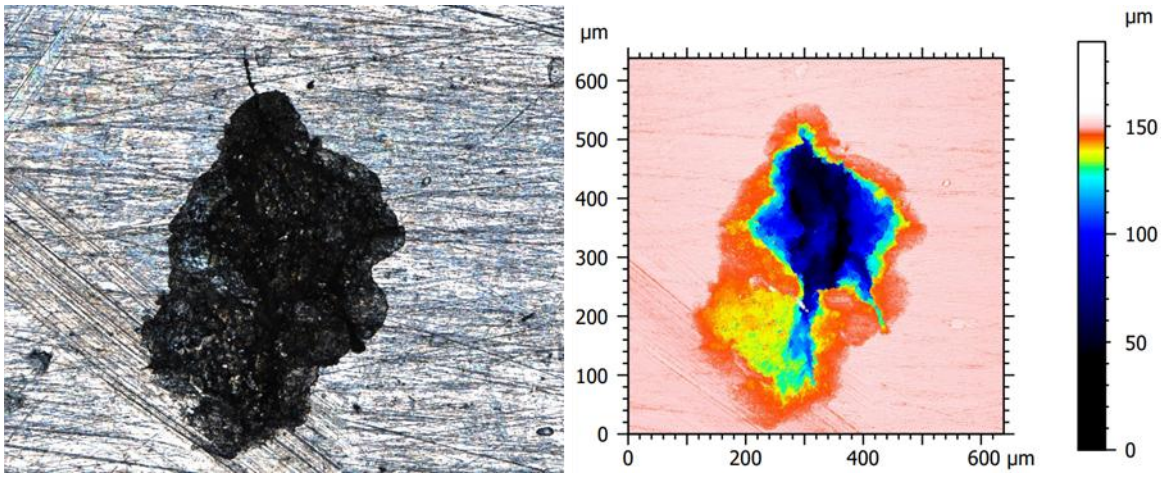

Figure 55: Sample ID:2a showing the pit which had developed on the surface after 1080 hours of exposure and which had not been observed after observation at 672 hours. This image was taken at the end of the test (1776 hours) using the 10x magnification, 0.4 lens on the CLSM. The right hand image was acquired using the same lens on the CLSM to obtain a topographic profile which was then levelled against the surface of the sample.

With a Z-stack of this pit showing signs of cracking at the base of the pit, it was cut from the sample and examined using an SEM, the images from which can be seen in Figure 56. Under increased magnification the cracking which had begun to propagate from the base of the pit was clearly visible and so the sample was sent for CT scanning.

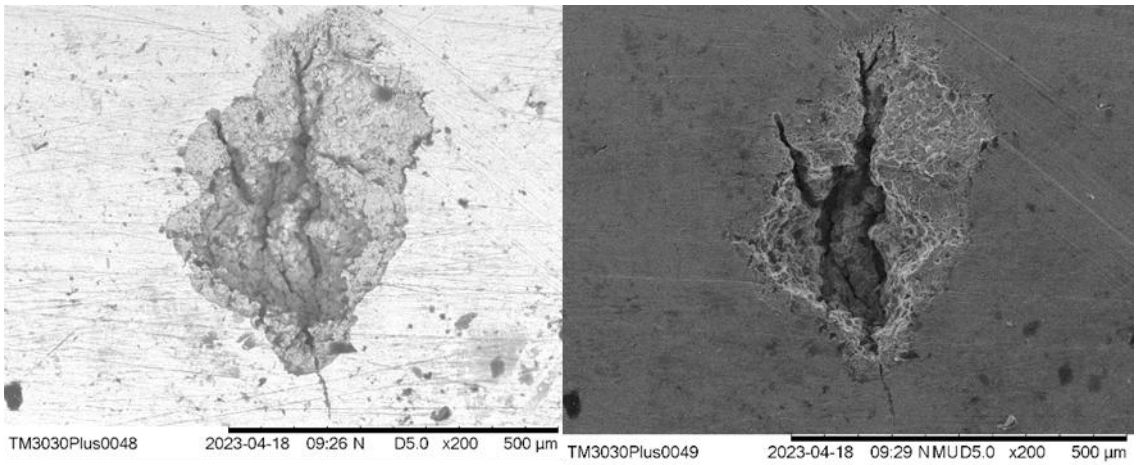

Figure 56: SEM image of the pit shown in Figure 55. (L) An image taken using a 15kV accelerating voltage using backscatter electron mode and under 200 times magnification. (R) The same location imaged using the secondary electron mode but with the same accelerating voltage and magnification.

The CT scan, shown in Figure 57 used a 110 kV beam energy with a power of 10 W. An exposure time of 15 seconds was assigned resulting in 1601 radiographs over a rotation of 360° and four times magnification with voxels measuring 1.2 x 1.2 x 1.2 µm. From analysis undertaken by *A. Prior*, it was determined that the crack shown in Figure 57a when combined with the pit reached a depth of approximately 200 µm while the crack

in Figure 57b coupled with the depth of the pit shows corrosion damage reaching approximately 150 µm (144).

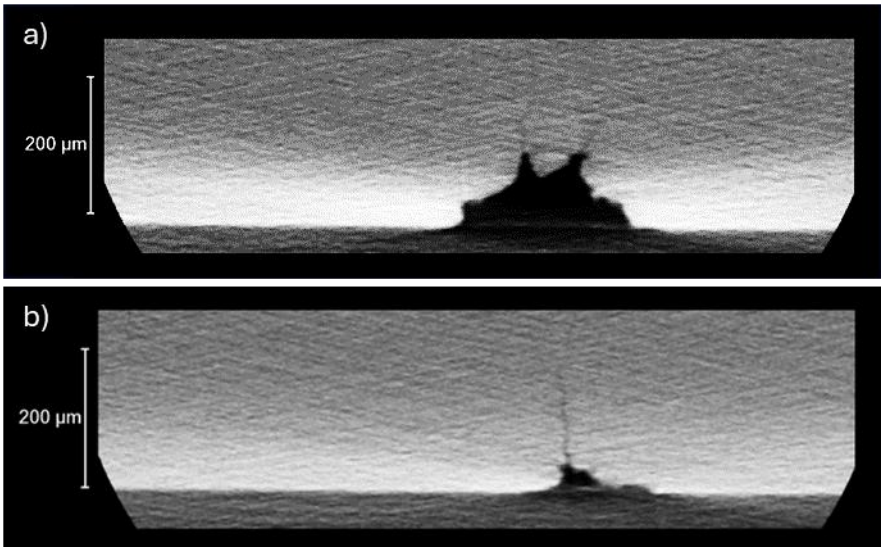

Figure 57: The CT scan results of the pit imaged by CLSM (Figure 55) and SEM (Figure 56) showing two slices. A) shows the pit splitting into two lowest points with cracks propagating from each. B) shows a longer crack propagating from a shallower location on the pit.

Achieving substantial corrosion equating to roughly 50% of the depth of AGR cladding showed that the constantly wetted approach was a viable means of producing cracking within samples of 316 stainless steel.

<u>Sample ID:5a:</u>

This sample was thermally treated at 650°C for five hours with the oxide layer removed by shot blasting as opposed to the hand sanding used on samples such as ID:2a. It is worth noting that along with the issues caused by the shot blasting process which hampered the corrosion, the uneven surface made examination under the microscopes more difficult. This sample was started after the decision to leave the samples undisturbed for the entire test duration was made and therefore there are no intermediate images of the sample to compare the corrosion extent as the test progressed. However, examination of the sample after 1344 hours being subjected to the corrosion test, revealed a shallow pit had formed which is shown along with a topographic scan in Figure 58.

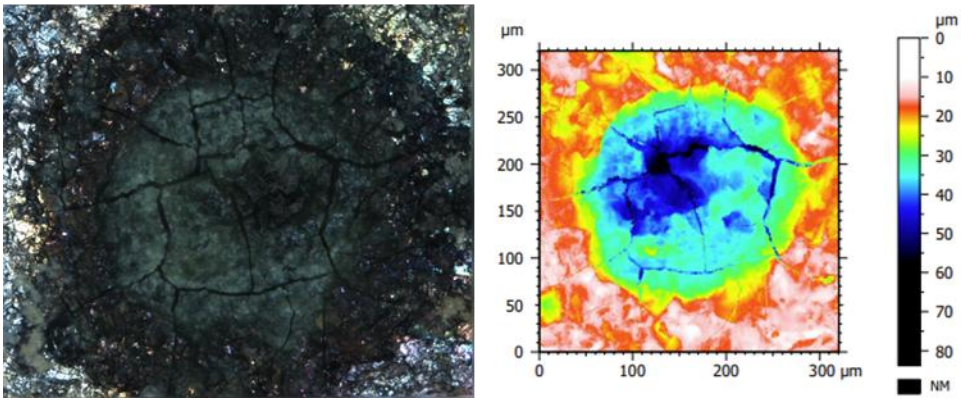

Figure 58: Sample ID:5a after 1344 hours of corrosion without interruption for examination. (L) Optical image taken using the 20x 0.4 lens on the CLSM. (R) The topographic scan of the same area also using the 20x 0.4 lens.

Under optical and topographic examination it was determined that limited pitting had occurred on this sample however, compared to sample ID:2a the pit was shallow, only measured at 60 – 70 µm at the lowest point and the bulk of the pit only reaching 40 - 50 µm according to the extracted profile which is shown in Figure 59.

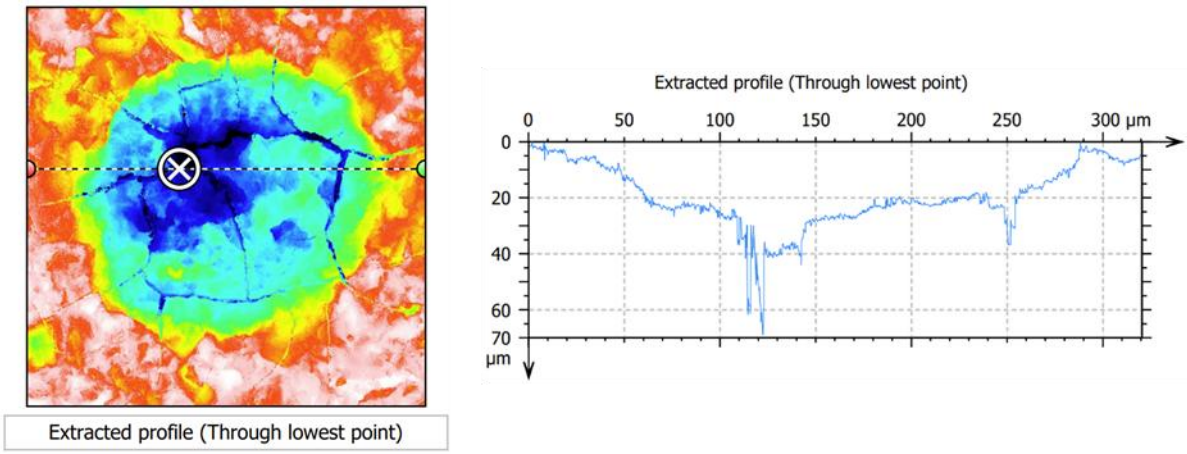

Figure 59: The extracted topographic profile pass through the lowest point measured by the CLSM scan of a pit on sample ID:5a.

The reduced level of corrosion observed in this sample has been attributed to the shot blasting of the surface. However, despite this, the cracking occurring around the grains was deemed to be an indication that producing SCC and therefore representative cracks in 316 stainless steel would be possible using this approach.

<u>Sample ID:11</u>

With the corrosion of strips of 316 stainless steel proving to be successful at generating pitting with some cracking also observed, samples of 304 stainless steel were acquired

from the University of Leeds mechanical workshop and the composition tested with SEM-EDS and compared to the standard composition of 304 stainless steel.

As set out in Table 9, this sample was initially held at 950°C for 2 hours followed by furnace cooling to 700°C where it was held for a further 70 hours. Following this the sample was left to furnace cool and return to room temperature. This sample was then hand sanded to remove the oxide layer that had accumulated exposing the stainless steel underneath. It was then subjected to the constantly wetted approach for 432 hours. After this initial period, the sample was removed and examined though minimal corrosion was observed. While it was expected that using 304 stainless steel would corrode more readily when compared to the 316 stainless steel samples used in the other tests, this test was conducted over a reduced duration which may account for the reduced corrosion.

Table 9: Summary of the experimental conditions for the sample of 304 stainless steel in the drying cabinet set up.

Sample ID	Thermal Treatment		Surface Finish	Experimental Conditions		
	Temperature (°C)	Duration (hours)		Temperature (°C)	Concentration (g/L)	Duration (hours)
11	950 700	2 70	HS	65	380.8	432

Thinning of Samples:

After examination of the samples showed promise with pitting reaching 100-150 µm it is expected that, if time had not been a limiting factor, then a through-sample defect would have been possible. However, as time was limited a means of speeding up the corrosion process was required. It was decided that this would take the form of thinning the samples rather than by increasing the concentration of chloride any further. Seven samples were selected with these outlined in Table 10 and Table 8 showing the conditions prior to thinning.

Table 10: Conditions experienced by the samples post thinning with a Dremel.

Sample ID	Thinned After (hours)	Experimental Conditions		
		Temperature (°C)	Concentration (g/L)	Total Duration (hours)
2a	1776	65	380.8	3120
4a	888	65	380.8	2232
3a	1488	65	380.8	2832
3b	432	65	380.8	1776
7	432	65	380.8	1776
2b	432	65	380.8	1776
11	432	65	380.8	1776

Each of the samples were removed from the initial testing being conducted and washed before being analysed using the CLSM and the locations of corrosion damage marked and traced to the reverse of the sample. A Dremel was then used to grid away a significant portion of the stainless steel within the bounding box traced to the reverse of the sample. Following this, the samples were restressed for further exposure to the corrosive environment for a further 1344 hours with minimal observation to prevent potential passivation.

It should be noted that sample ID:2a was handled differently. For this sample, the sectioned and imaged portion (see Figure 55, Figure 56 and Figure 57) was thinned and placed into a weigh boat and the $MgCl_2$ solution added.

Figure 60: Corrosion located in and around the site where a Dremel was used to remove material. This image shows sample ID:3a after the further 1344 hours of corrosion and is a composite, tiled image taken using the CLSM.

Minimal corrosion was observed on the shot blasted samples though small cracks were observed in the Dremel sites with one such location shown in Figure 60. When sample ID:11 was examined some isolated cracks were noted however the majority were located either within or propagating from the thinned region. Figure 61 shows four of the thinned regions of the sample on both sides of the sample. Side one with the Dremel marks showed evidence of cracks propagating from the regions where material was removed. When examining the reverse of the sample in the same location, extensive cracking was observed.

With the crack networks matching up on either side of the sample it was decided that each of the thinned regions would be cut out of the strip into 9.5 mm diameter discs matching the pinhole and slit discs which were purchased from Edmund Optics.

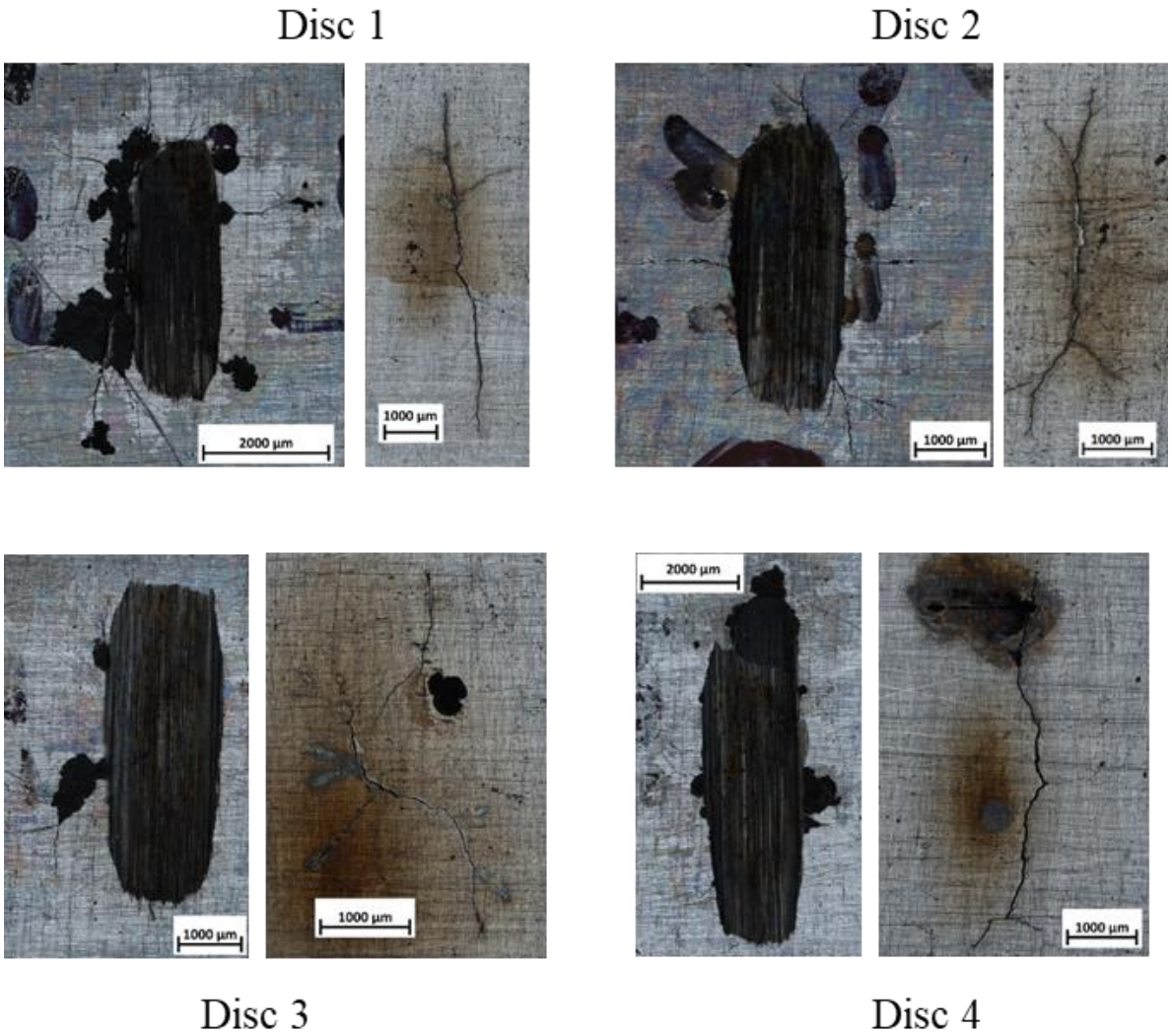

Figure 61: Images taken of four thinned regions of sample ID:11 on both the side where the Dremel was applied and the reverse location where initial corrosion was observed.

These discs were then subjected to a CT scan using a 0.39x magnification and a voxel size of 11.7 µm x 11.7 µm x 11.7 µm. All the discs were scanned at the same time stacked on top of each other. It should be noted that the dark concentric rings seen in the overhead view of the discs are an artefact of the CT process rather than being a feature on the samples.

<u>Disc 1:</u>

From the CT scan of this disc, shown in Figure 62, Figure 63 and Figure 64, the crack is observed to have propagated through the remaining thickness of the sample and in some locations it appears to have propagated through the full 400 µm of the sample. The width of the crack remains relatively constant throughout its full length however, it is notable that the crack is not dendritic as would be expected if the crack was SCC.

Figure 63b shows two crack sections, this is the same crack however the pathway passes out of the plane being imaged before returning back to the imaged plane.

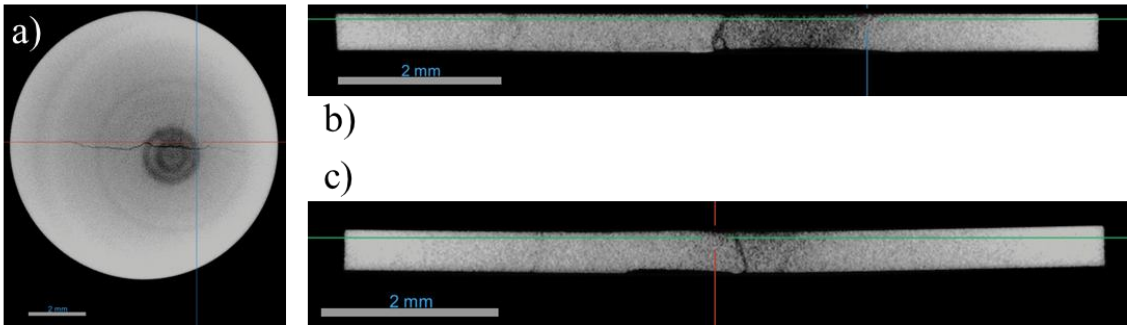

Figure 62: A CT image of disc one in the "upper" portion of the disc. a) The plan view. b) A slice looking along the red line in (a). c) A slice looking along the blue line in (a).

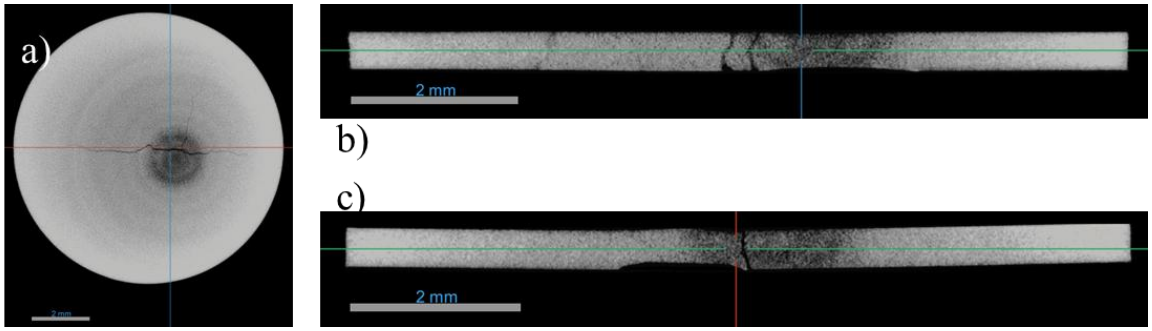

Figure 63: A CT image of disc one in the "central" portion of the disc. a) The plan view. b) A slice looking along the red line in (a). c) A slice looking along the blue line in (a).

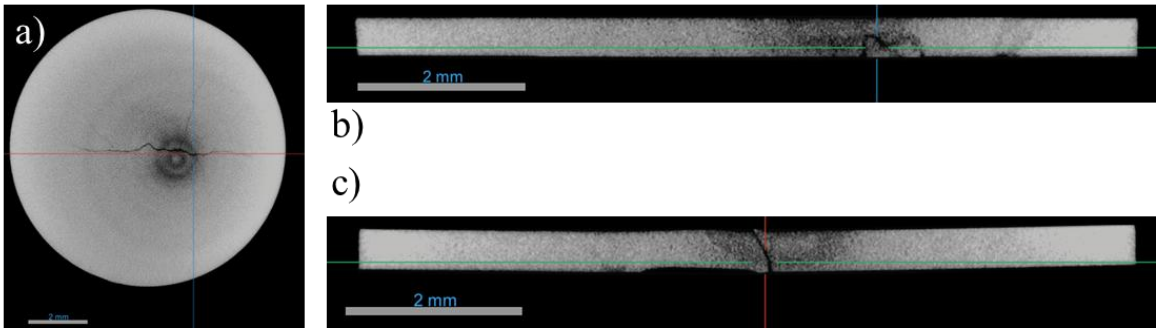

Figure 64: A CT image of disc one in the "lower" portion of the disc. a) The plan view. b) A slice looking along the red line in (a). c) A slice looking along the blue line in (a).

In Figure 64b, a “U” shaped crack is seen and it was not apparent from this view whether the crack had propagated through the sample. With other portions of the crack propagating through the full thickness this was not a concern and suggested that while not immediately apparent from the majority of the images of the disc, the crack may have some branches and dead ends adding complexity to the crack path.

Disc 2:

The crack observed in disc two appears to be narrower than that produced in disc one with the CT scan struggling to produce clear images due to the size of the voxels. Despite this however, it is clear that the crack does propagate through the width of the stainless steel emerging in the thinned region as can be seen in Figure 65, Figure 66 and Figure 67.

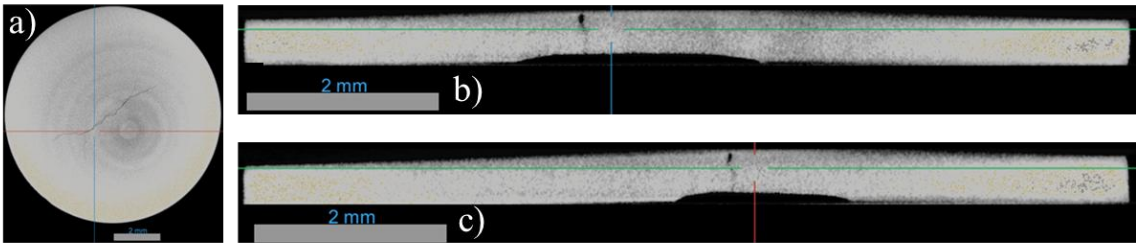

Figure 65: A CT image of disc two in the "upper" portion of the disc. a) The plan view. b) A slice looking along the red line in (a). c) A slice looking along the blue line in (a).

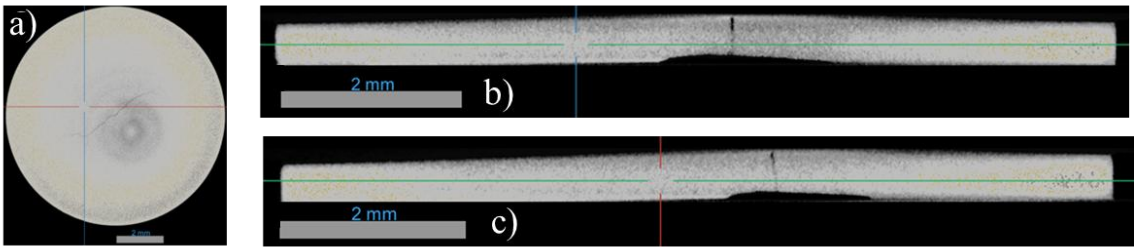

Figure 66: A CT image of disc two in the "central" portion of the disc. a) The plan view. b) A slice looking along the red line in (a). c) A slice looking along the blue line in (a).

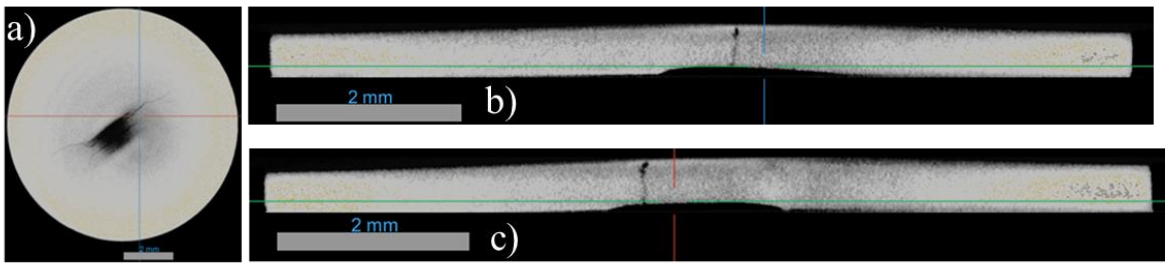

Figure 67: A CT image of disc two in the "lower" portion of the disc. a) The plan view. b) A slice looking along the red line in (a). c) A slice looking along the blue line in (a).

Disc 3:

When compared to Disc 1 and Disc 2, Disc 3 is even more indistinct on the CT images owing to the voxel size as shown by the lack of a distinct pathway on Figure 68, Figure 69 and Figure 70. However, it is still possible to determine the pathway of a defect, for

example in Figure 68b, a crack path can be seen just to the left of the blue line. There is a possibility that two cracks were generated during the corrosion of this region, in Figure 68a, there are two distinct sections of crack that do not appear to be connected and examination of the CT results was inconclusive as far as a connection between the two sections.

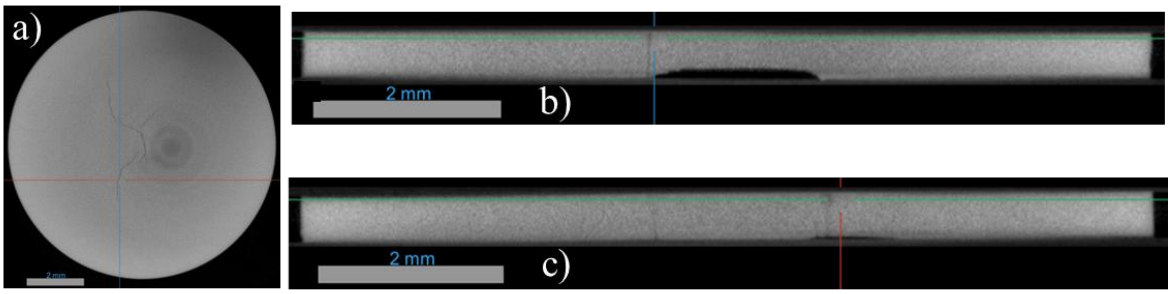

Figure 68: A CT image of disc three in the "upper" portion of the disc. a) The plan view. b) A slice looking along the red line in (a). c) A slice looking along the blue line in (a).

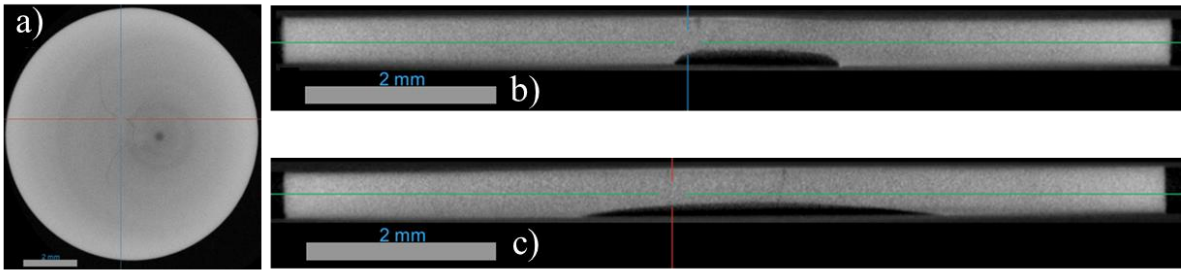

Figure 69: A CT image of disc three in the "central" portion of the disc. a) The plan view. b) A slice looking along the red line in (a). c) A slice looking along the blue line in (a).

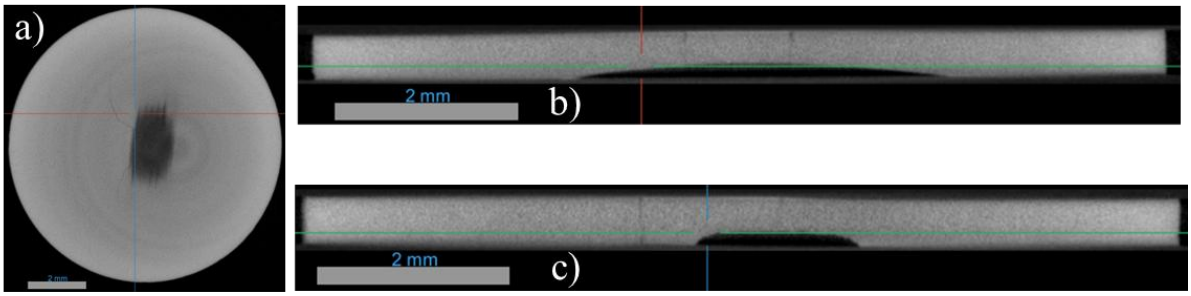

Figure 70: A CT image of disc three in the "lower" portion of the disc. a) The plan view. b) A slice looking along the red line in (a). c) A slice looking along the blue line in (a).

<u>Disc 4:</u>

As with the other discs, a crack pathway is clear from the CT images shown in Figure 71, Figure 72 and Figure 73. Unlike the other discs however, there is evidence of branching, in particular this can be seen in Figure 72b with multiple tracks imaged

covering the full thickness of the sample though this could be the result of the crack passing in and out of the image plane multiple times in a short horizontal distance.

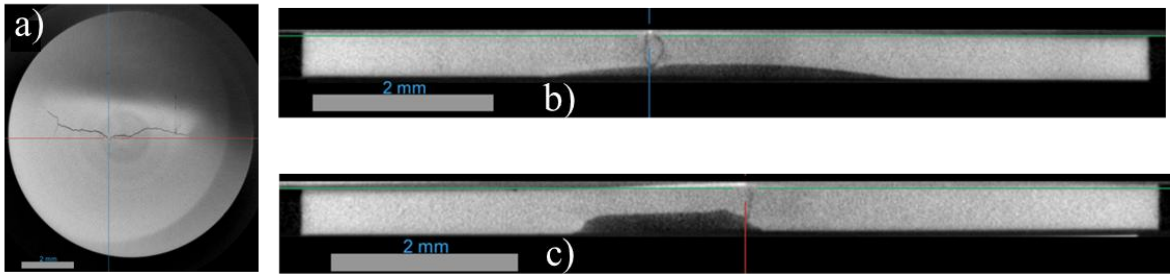

Figure 71: A CT image of disc four in the "upper" portion of the disc. a) The plan view. b) A slice looking along the red line in (a). c) A slice looking along the blue line in (a).

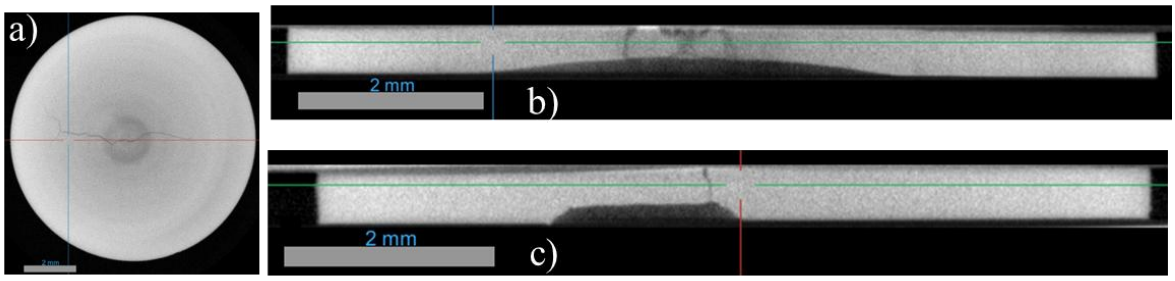

Figure 72: A CT image of disc four in the "central" portion of the disc. a) The plan view. b) A slice looking along the red line in (a). c) A slice looking along the blue line in (a).

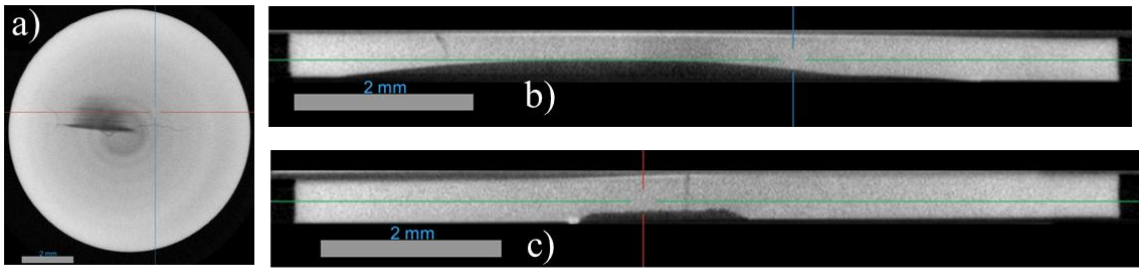

Figure 73: A CT image of disc four in the "lower" portion of the disc. a) The plan view. b) A slice looking along the red line in (a). c) A slice looking along the blue line in (a).

4.3 Summary

In trying to produce representative cracks, several methods have been tested. The acidified potassium tetrathionate test were able to corrode the sample of mild steel though rather than producing pits, the sample degraded through exfoliation which would not result in the production of pits or cracks. The samples of 316 and 304 stainless steel tested showed no evidence of corrosion, as demonstrated in Figure 44.

The drop evaporation technique on the other hand was shown to be capable of corroding both 304 and 316 stainless steel with evidence of pitting in both hand sanded and shot blasted samples. Given the samples subjected to shot blasting were also 316 stainless steel, the production of corrosion pits with signs of cracking was notable as 316 grade stainless steel is considered to be a go to choice for corrosion resistant stainless steel and the shot peening effect of the shot blasting approach increasing the resistance to stress corrosion cracking

While not intended to be performed at the outset of the work, the thinning of the samples using the Dremel allowed for the rapid production of the through-thickness cracks in targeted locations and this showed that the constantly wetted technique was viable to produce cracking. While the original aim of the corrosion work was to produce representative cracks ideally via stress corrosion cracking, it was acknowledged that cracks with a similar morphology were desired and if that was achieved via another form of corrosion then it was acceptable. The cracks produced in this work are not the tortuous cracks expected to be found with SCC however, the scale of these cracks is representative of those expected. These cracks, from the CT scans would appear to be a half way stage between the significant cladding failure seen in Figure 5 and the appearance of SCC cracks. It is also noted (with the dimensions determined in Section 5.3) that these defects are wider than those expected to be formed in a failed AGR cladding sample. These defects are closer in dimension to the example of corrosion failed AGR cladding in Figure 5. However, corrosion is not the only means by which a fuel pin cladding may fail with other causes detailed by *M. Barker et al* (38). It is feasible that some of the mechanisms discussed in the paper could thin the cladding prior to or during storage conditions with corrosion providing the final break-through. This could result in crack pathways caused by mechanisms such as PCMI, as shown in Figure 74, which measures approximately 20 µm on the exterior surface of the cladding and 64 µm on the interior / fuel-cladding interface side of the cladding.

Therefore, while these cracks are not necessarily the tortuous SCC cracks intended, PCMI and clad restructuring as detailed by *Barker et al,* could result in cladding failures of similar dimensions and morphologies.

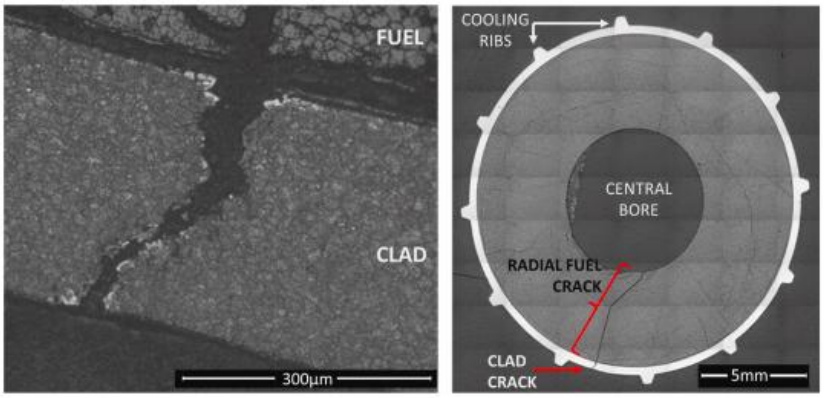

Figure 74: A crack caused by PCMI. Image taken from (38).

5 Image Analysis of Defects

In order to determine the flow of fluid (liquid or gaseous) through a channel it is necessary to know the dimensions of said channel. In this work, while the defects produced are 3D, it was assumed that a 2D cross section would be sufficient to provide an approximation at the dimensions and ultimately the flow through the channel.

5.1 Computational Work

5.1.1 Approach to Image Analysis

In order to determine the flow channel length and average width it is necessary to remove the dead ends and other artefacts from consideration as these have a minor impact on the flow of fluid through the defect. To achieve this, the graphics package, Serif DrawPlus X8 was used and the brush tool used to remove these unwanted features. An example of this is shown in Figure 75 where voids and dead ends have been removed to prevent these from altering the output.

Figure 75: (L) The original image of a crack taken from Ref (15) (R) The cleaned up version of the crack used in the image analysis code.

Following the cleaning up of the image it is loaded into the Matlab code to be simplified into a binary image. In this part of the process, each pixel of the image is assigned a value, either one or zero depending on the colour of the pixel. The next step of the process is to produce the skeleton of the defect pathway. This is best described as a controlled erosion process which results in a one pixel wide line following the essential structure or centreline of the defect being processed. A very simple example of this is shown in Figure 76.

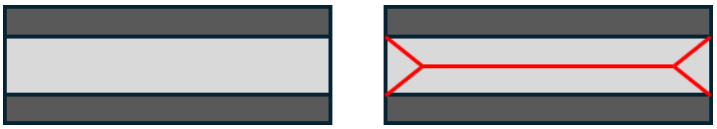

Figure 76: (L) The original image of the defect to be analysed. (R) The skeleton produced by the MATLAB code overlayed with the original image.

With this process, the openings at each end of the defect pathway cannot be handled simply. The skeleton process produces the triangular features seen in Figure 76R and

necessitates the addition of a a process to determine a suitable length in these regions. Once the skeleton has been produced, the user is invited to input the pixel coordinates of the point where the skeleton diverges into the triangular regions and the point at which this triangular region touched the edge of the image, highlighted in Figure 77. Between the locations b and c, Matlab has a built-in function to calculate the number of pixels between the two locations on a skeleton. To handle the a-b and c-d sections, it was decided that, as a right angled triangle could always be formed, pythagoras' theorem could be used. The code produced takes the coordinates of, for example, locations a and b and then calculates the straight line distance from location b to the edge of the image and adds it to the other lengths calculated – b-c and c-edge to give the total length of the crack.

Figure 77: The skeleton of the channel overlayed on an image of the channel with the coordinate locations highlighted.

To calculate the average width of the channel, the code counts the number of pixels which were assigned a value of "0" and therefore part of the defect pathway and then divides this value by the calculated length.

5.1.2 Determination of the Dimensions of Defects from Literature

While the initial testing of the code would be undertaken using defects drawn in the Serif DrawPlus X8 graphics package which allows for the dimensions to be accurately known, this is not possible with the cracks gathered from literature. In literature, the focus of the research nearly always involves knowing the width of the crack being investigated and no lengths were provided.

Therefore, to determine the length, circles of a known scale size were drawn and placed along the skeleton and then in a straight line from the edge of the skeleton to the edge of the crack image.

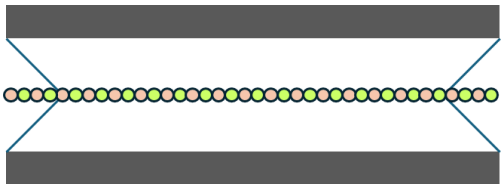

Figure 78: A diagram showing how the length of the cracks in literature was calculated.

Where the width is provided by the literature, if more than one width is supplied, these were averaged and used as the average width of the crack such as in Figure 79. Though it should be acknowledged that inaccuracies are present in both the placement of the cursor when the crack was measured and the placement of any bar showing the width, for example in Figure 79, it is not clear if the bar is the length associated with the bar or if it is the width of the crack as the bars occasionally overlap the material.

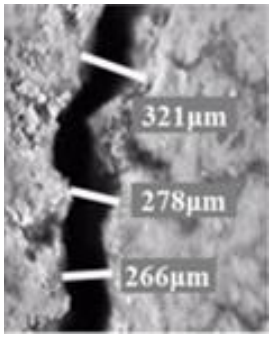

Figure 79: An example of a crack from literature where widths are provided. Image of the defect taken from Ref (145).

If only one width measurement was provided then other widths were calculated and averaged using the same method by which the length was determined but with the circle placed perpendicular to the skeleton path. When the manual measurement approach was tested a suitable level of accuracy was achieved.

5.2 Validation of the Image Analysis Code

5.2.1 Drawn Defects

In order to test the code, some channels of known dimensions were required. To achieve this Serif DrawPlus X8 is utilised to both draw cracks of known length and widths and therefore allow for an analysis of the sensitivity of the code to be undertaken.

5.2.1.1 Straight Channels

With the easiest possible defect for the code to be presented with consisting of a smooth, straight channel this was tested first. Two different tests were undertaken, the

first assessing how much of an impact the length made to the overall estimates with these results shown in Table 11 and secondly assessing the impact of increasing the width while the length remained constant, shown in Table 12.

From these tests it was determined that the code was able to determine the length and width of the drawn defects with satisfactory accuracy. When the length of the defect is increased and the width kept constant, there is little change in the accuracy of the length estimation however there is a slight improvement to the estimation of the width however this is not considered to be a substantial improvement. When the testing changed to keep the length the same throughout and to increase the width, while there was still little change in the length estimation, there was no clear pattern to the estimation of the width.

Table 11: The results from testing the image analysis code against drawn straight channels where the length was varied.

Known Dimensions		**Calculated Dimensions**		**% Variation**	
Length	**Width**	**Length**	**Width**	**Length**	**Width**
29.88	8.03	29.89	8.43	0.04	4.98
40.20	8.03	40.39	8.53	0.48	6.18
50.25	8.03	50.48	8.49	0.45	5.68
60.04	8.03	60.15	8.40	0.19	4.64
7001	8.03	70.03	8.37	0.03	4.20
80.15	8.03	80.26	8.37	0.14	4.29
90.21	8.03	90.41	8.35	0.22	4.02
100.26	8.03	100.33	8.33	0.07	3.81
200.80	8.03	201.33	8.29	0.26	3.28
400.56	8.03	401.01	8.26	0.11	2.81

Table 12: The results from testing the image analysis code for drawn cracks where the width was varied.

Known Dimensions		Calculated Dimensions		% Variation	
Length	**Width**	**Length**	**Width**	**Length**	**Width**
49.99	8.03	50.12	8.47	0.27	5.48
49.99	9.35	50.38	9.64	0.79	3.12
49.99	10.62	50.38	11.10	0.78	4.53
49.99	11.46	50.12	11.39	0.26	0.65
49.99	12.31	50.12	12.87	0.26	4.55
49.99	13.58	50.12	13.85	0.26	1.97
49.99	14.85	50.12	15.31	0.26	3.12
49.99	15.70	50.37	16.01	0.77	1.95

5.2.1.2 Organic Shapes

Having tested the code against the most simple scenario, more complex shapes featuring changes in direction were drawn out, again in Serif DrawPlus X8. This provided an increase in the difficulty for measuring the defect dimensions and therefore a step closer to testing the code on cracks found in the literature.

Table 13 shows the results from the testing. Overall, the code performed to a suitable level of accuracy on the majority of the tested defects. However, when right-angled corners were tested, the approach resulted in a large deviation from the known length when compared to the other results obtained. It is theorised that this is due to the interaction of the right angles and the skeleton produced which cuts across the corner thereby not following the centreline from which the length was measured. This is reinforced by the successful estimation of more complex defect shapes featuring 90° turns but in arcs rather than abrupt changes in direction.

This is considered to be a minor issue as, while the percentage change is above what would be expected based on the results gathered for other defects, the estimation is still reasonable and the nature of the defect is outside of any expected corrosion defect.

Table 13: Results from testing the image analysis code against more complex drawn defect pathways.

Defect Image	Known Dimensions		Calculated Dimensions		% Variation	
	Length	**Width**	**Length**	**Width**	**Length**	**Width**
	16.12	0.63	15.45	0.71	13.39	4.13
	58.10	0.63	60.69	0.62	1.45	4.45
	24.92	0.63	25.63	0.65	2.81	2.86
	32.58	0.63	33.85	0.61	2.96	3.89
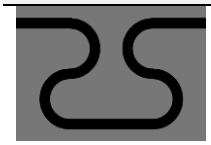	65.16	0.63	67.72	0.64	1.14	3.92
	99.95	2.33	102.09	2.28	1.97	2.14

5.2.2 Defects from Literature

The final test for the code is to estimate the dimensions of cracks sourced from literature. The defects were sources from a range of papers, not only covering corrosion of metals but also cracks in concrete to provide variation in the topography of the defect edges. Table 14 shows the defects chosen along with the dimensions which were either stated by the source or calculated using the approach outlined in Section 5.1.2. The results generated by the image analysis code are also presented along with percentage variation between the stated dimension and the calculated dimension.

As these cracks were sourced from literature, many featured measurements of width that had been overlayed. Where this occurs, Serif DrawPlus X8 was used to edit out these labels with all the cracks being “cleaned up” in the software to remove voids and other artifacts which were detected by the code but did not contribute to the main crack.

Table 14: Results from testing the image analysis code against cracks presented in literature.

Defect Image	Source	Known Dimensions		Calculated Dimensions		% Variation	
		Length	Width	Length	Width	Length	Width
	(15)	400.00	50	442.09	49.65	10.52	0.71
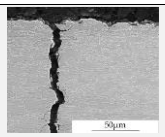	(146)	121.88	6.25	131.66	7.00	8.03	11.95
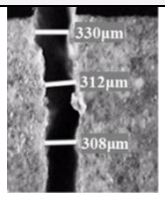	(145)	2021.25	317.00	2247.74	311.28	11.21	1.80
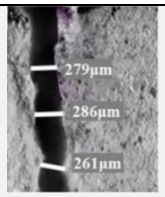	(145)	2197.13	275.00	2109.06	2261.58	4.01	4.88
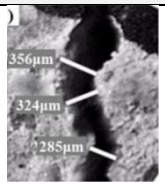	(145)	1646.50	322.00	1772.35	311.90	7.64	3.14
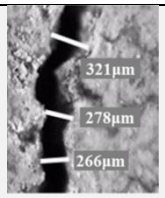	(145)	2310.88	288.00	2602.13	250.25	12.60	13.11
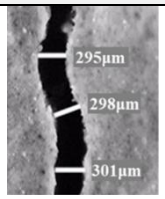	(145)	1994.13	298.00	2302.59	290.68	15.47	2.46
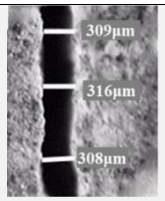	(145)	2085.75	311.00	2210.25	319.86	5.97	2.85

Defect Image	Source	Known Dimensions		Calculated Dimensions		% Variation	
		Length	Width	Length	Width	Length	Width
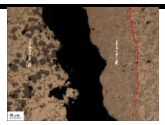	(147)	192.50	63.37	222.93	58.37	15.81	7.89
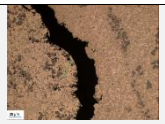	(147)	205.00	26.04	220.82	29.02	7.72	11.46
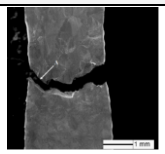	(148)	2.88	0.31	3.10	0.33	3.82	2.43
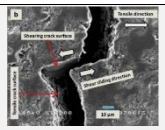	(149)	132.50	18.75	133.94	16.78	1.09	10.52
	(150)	2562.50	62.50	2830.92	62.93	10.47	0.69
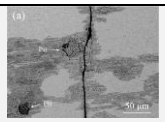	(151)	204.00	3.13	244.09	3.61	19.65	15.44
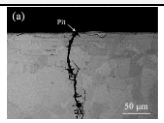	(151)	156.25	4.69	168.77	4.35	8.01	7.16
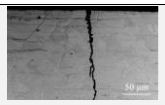	(151)	165.75	4.75	178.95	4.69	7.97	1.24
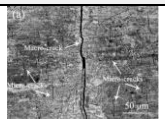	(151)	207.50	2.96	213.40	3.08	2.84	4.06
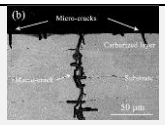	(151)	107.50	5.25	115.74	6.25	7.66	19.11
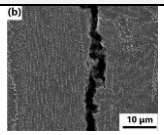	(152)	39.50	3.63	43.92	3.23	11.19	10.82
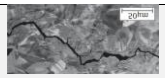	(153)	327.00	3.20	341.58	3.07	4.46	3.91
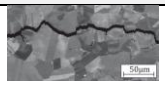	(153)	291.50	4.00	309.68	4.33	6.24	8.21

5.3 Application to Corroded Samples

The images of the defects presented in Figure 62, Figure 63, Figure 64, Figure 65, Figure 66, Figure 67, Figure 68, Figure 69, Figure 70, Figure 71, Figure 72 and Figure 73 were tested using the image analysis code to determine the length and average width of the defects produced through corrosion. However, the voxel size using the in the CT scan and the overall low resolution prevented the defect from being detected as seen in Figure 80. In order to determine a length of the crack and an average width, the image analysis code was used to determine a number of pixels per mm scale with the determined dimensions shown in Table 15.

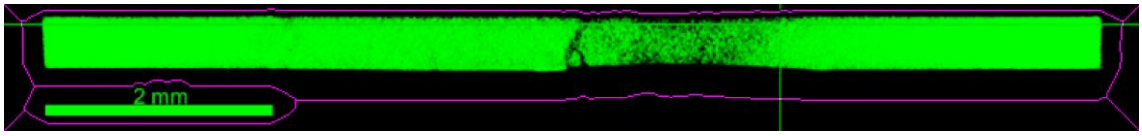

Figure 80: Attempted analysis of the produced cracks showing the skeleton produced by the code overlayed on the original image provided.

Table 15: Length and average width of the defects in Disc 1 as determined using a pixel/mm scale and the image analysis code.

Image	Length (µm)	Average Width (µm)
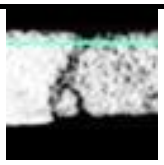	384 (left channel) 360 (right channel)	36
	504	60
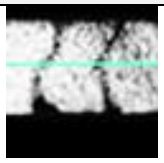	468 (left channel) 432 (right channel)	43.2 (left channel) 45.6 (right channel)
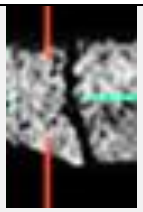	420	40
	456	34.5

While these cracks were calculated to be wider than those which are expected to be found in the AGR cladding, the morphology of the cracks represents a step towards stress corrosion cracks when compared to the pinhole and slit discs that were used in this work as well as when compared to the 227 μm diameter defect sample constructed by *M. Jackson.* When compared to the AGR cladding failure shown in Figure 5, these defects are of a similar width to this however, in most of the cracks have a morphology featuring more tortuosity and branching that the failure in Figure 5.

5.4 Summary

In testing of the image analysis code, the initial tests with the pathways drawn manually a good level of agreement was achieved. Progressing the testing onto more organic shapes showed that, as long as the changes in direction were not abrupt, a good estimation of the crack length could be achieved and this in turn resulted in the width being accurately estimated.

The approach to determining the length and width of defects taken from literature is accepted to have inherent flaws in the process however it is believed that all measures to make the process as robust and repeatable as possible were established and followed. To confirm the approach was viable, the organic defects which had been drawn in Serif DrawPlus X8 were used as tests with the method proving to be suitable, if occasionally fiddly to undertake. Therefore it was decided that multiple determinations of the length and width would be used and an average taken.

Unfortunately, the resolution on the CT scans was not sufficient in order for the defect to be detected by the skeletonization process. In an attempt to rectify this the contrast was altered but this still did not allow for the detection of the channel. As a result the manual approach was used. With the evidence gathered from testing cracks from literature, it is believed that with higher resolution scans this process would have been able to detect the channels however, this would likely have necessitated further work to the samples which would have increased the change of damage and rendered the discs unsuitable for use int eh vacuum drying or fluid flow rig.

6 Simplified Fluid Flow Testing

This Chapter sets out the work done to design, build, test and operate the simplified fluid flow rig used to provide repeatable, accurate measurements of the pressure over time as air was allowed to return to an evacuated gas sample tube passing through the selected disc or defect. The attempts to manufacture narrow crack pathways from Perspex is also covered here. Finally the results gathered from the tests conducted with optical pinhole and slit discs are presented as well as the results from the corroded samples which proved that the defects had formed a crack pathway through the full thickness of the material.

6.1 Overview

With a need to determine the flow rate through the defects a simple set-up was devised in which a tank could be evacuated with the pressure then monitored as air is allowed to re-enter the tank via the defect. Unlike the vacuum drying rig (discussed in Chapter 7) this rig allows for the defect to be analysed without external factors influencing the flow such as the evaporation of water. By removing these variables and influences, the results gathered from this rig could be utilised in providing the validation for the models being considered.

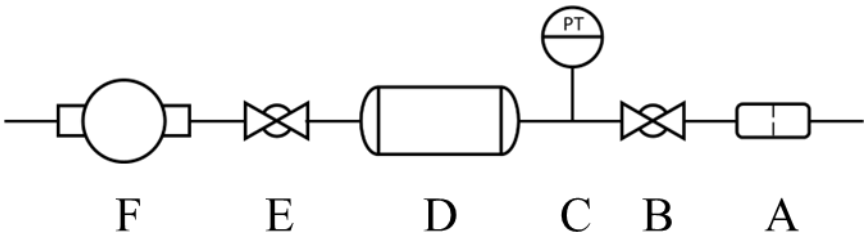

Figure 81: A schematic for the simplified fluid flow rig.

Figure 81 shows the schematic for system devised, with the final rig shown in Figure 85. A Swagelok fitting was used to house the defect discs. Initial tests with the discs being secured in place using the fitting found that the disc would deform and potentially burst under test conditions. To solve this, a metal disc containing a defect such as those shown in Figure 82 is placed into the fitting with an O-ring to ensure an air-tight seal is formed. This limits the deformation and maintains the integrity of the disc. Two valves from Swagelok are used to allow the tank to be isolated from the pump and atmosphere as required. An Omega pressure transducer is used to provide pressure data logging capabilities. The initial plan for the rig had been for it to be designed in such a manner

as to allow for the tank to be under vacuum or atmospheric pressure with the vacuum pump either used to evacuate the tank prior to the air flowing through the defect or to pull a vacuum with the air being removed through the defect however only the set up shown has been used.

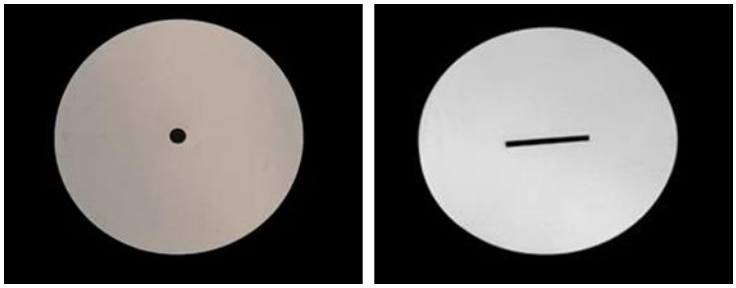

Figure 82: Examples of (L) a pinhole disc test piece and (R) a slit test piece. Images from (154) and (155) respectively.

6.2 Experimental Work

6.2.1.1 Methodology

In order to conduct an experiment using the rig, the valves labelled as B and E in Figure 81, are opened and the chamber (component D) allowed to return to atmospheric pressure before the valve B is closed. The sample mount can then be attached at component A's location in the schematic.

To assemble the sample mount, the upper part of the fitting is removed and the first O-ring inserted and adjusted to ensure it is flush with the base of the fitting. Then the sample the be tested is added to the assembly along with another O-ring on top to form a seal. Finally the tubing with the ferrule is added and the fitting is re-attached and tightened to seal the assembly in place. The components for this assembly and the completed form can be seen in Figure 83 and Figure 84.

Figure 83: The components in the order of assembly to hold a sample, in this case a corroded disc, in place for both the simplified fluid flow rig and later the vacuum drying rig. Left to right: one half of a Swagelok fitting, a Swagelok ferrule with tubing to form a seal, the first O-ring, the sample to be tested and the final O-ring to seal against the base of the fitting.

Figure 84: The assembled fitting using the components shown in Figure 83. A similar assembly was used in the vacuum drying rig.

The data logger should be started at this point to record the atmospheric pressure ahead of the evacuation. At this point the vacuum pump can be turned on and the tank evacuated to the desired pressure. Once this has been achieved, the valve, labelled as E, is closed to isolate the system and valve B opened to begin the test.

6.2.1.2 Testing

To provide data which could be used to compare experimental data to the predictions made by the computational work undertaken several batches of tests were undertaken. The first set used pinhole discs purchased from Edmund Optics. These discs, 0.3 mm thick and with a diameter of 9.5 mm featured a pinhole in the centre. Various sizes of pinhole diameter were tested: 1 µm, 5 µm, 10 µm, 20 µm, 50 µm and 100 µm. Additionally, slit discs (shown in Figure 82) were tested. These slits measure 3 mm long and the widths tested were 10 µm, 50 µm and 100 µm. Finally, the corroded discs produced were tested. Details of these can be found in sections 4 and 5 however, it is worth mentioning that the samples were cut out of the strips into discs with a diameter of 9.5 mm.

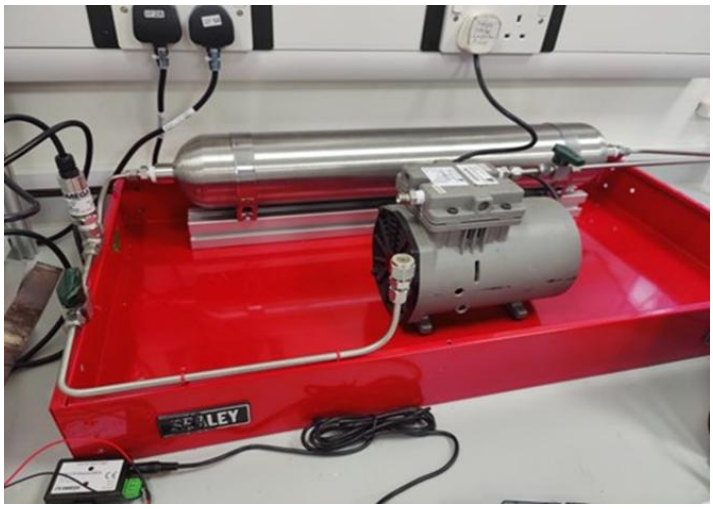

Figure 85: A photograph of the simplified fluid flow testing rig showing the sample mounting location, pressure chamber and vacuum pump.

All the tests were conducted using the same approach. After ensuring that the tank was at atmospheric pressure prior to starting any test the vacuum pump was switched on for approximately six minutes which resulted in a pressure of 0.1 BarA being achieved. The results obtained from these tests can be seen in section 6.3.

6.3 Results and Discussion

6.3.1 Pinhole Discs

Figure 86 shows the averaged results from three tests conducted using each of the stated size on pinhole discs. From these tests it was observed that the smaller diameters, 1 µm and 5 µm resulted in a rate which was not dissimilar from the leak rate of the system. This prompted uncertainty as to if the sample assembly or the rig itself was leaking and contributing to a faster return to atmospheric pressure than would be expected. As a result these discs were removed from any future testing and comparison with the computational predictions. These tests also prompted additional checks on the fittings and components although there was no significant leaks detected which would impact other results gathered using this rig.

As would be expected, the large the hole in the disc, the faster the system returned to atmospheric pressure. It was noted that despite the multiple repeated experiments the 10 µm diameter pinhole was observed to result in the pressure returning to atmospheric pressure quicker than the 20 µm diameter pinhole did. Initially this was attributed to the disc and assembly not sealing correctly however, after a total of three tests conducted independently with both the 10 µm and 20 µm discs with little variation observed suggests this is not the case and the result is genuine.

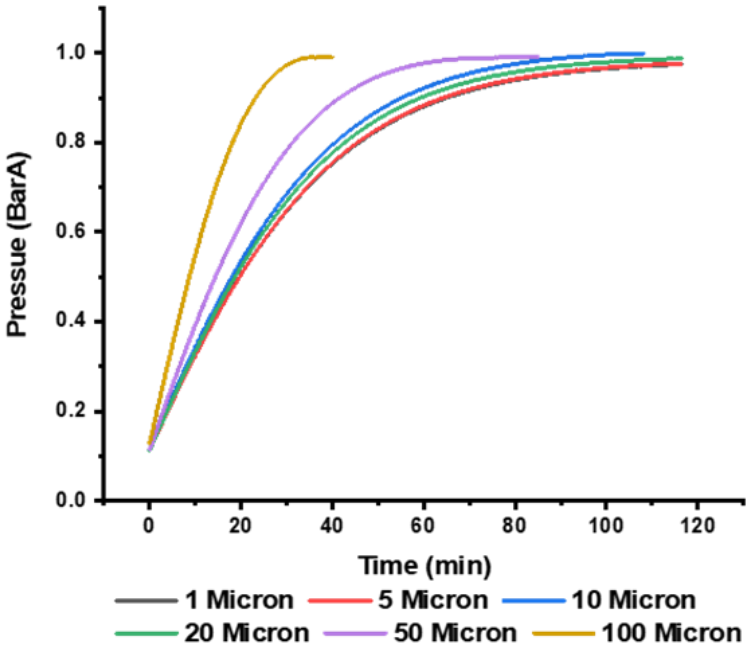

Figure 86: The time taken for the sample tank to reach atmospheric pressure from a starting pressure of approximately 0.1 BarA through discs featuring various sizes of pinholes.

6.3.2 Slit Discs

As with the pinhole discs, three independent experimental runs were conducted and the average results are shown in Figure 87. These samples, despite being tested repeatedly and at different times showed very little deviation across the three runs indicating that the rig was reliably sealing and operating in a repeatable fashion. Due to the larger opening area presented by the slit discs, the time to return the system to atmospheric pressure was significantly quicker than the pinhole discs as would be expected.

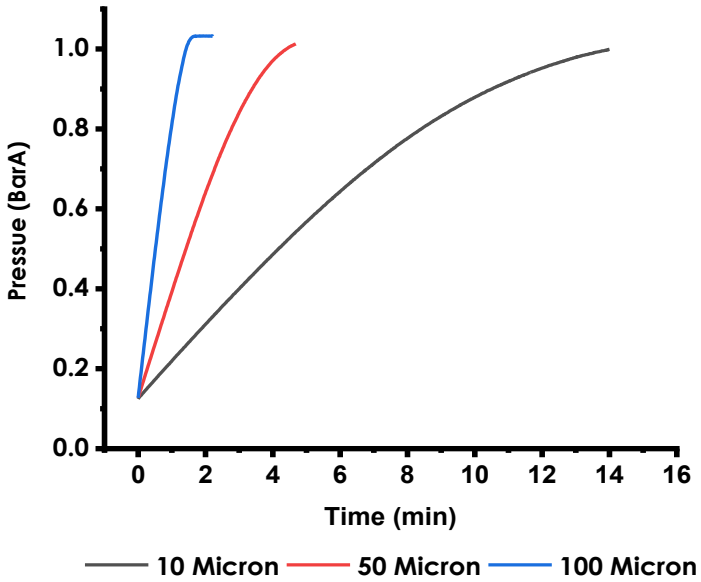

Figure 87: Average results from three tests of each of the slit discs in the simplified fluid flow rig.

6.3.3 Perspex Samples

While waiting for the corrosion experiments to produce suitable defects, an attempt to manufacture cracks in a disc which could be mounted inside the assembly was sought. One option tested was to use Perspex. A strip 30 mm in width and 200 mm long was cut from a sheet and placed into a vice after which a chisel and mallet were used to produce a crack which propagated partially through the Perspex with a representation of the set up shown in Figure 88. Once a crack of suitable depth had been created, a junior hacksaw was used to cut a disc out encompassing the end of the crack. Files were then used to clean the edge of the sample up and refine the shape, an image of one of the samples produced is shown in Figure 89.

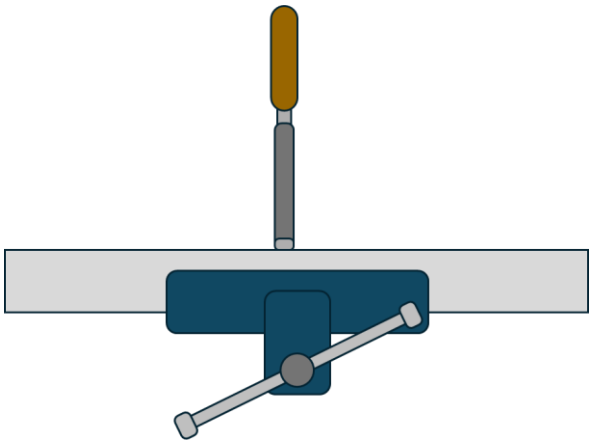

Figure 88: A representation of how the Perspex strips were cracked.

Samples were produced including a disc with no crack present to act as a blank, leak testing sample. This blank sample tested and a leak was detected this likely arose from the Perspex being too thick to fit into the Swagelok fitting fully ensuring a proper seal was not possible. Another factor was likely the uneven surface of the Perspex which originated from the use of a vice to hold the sample in place for the crack production and sample shaping process.

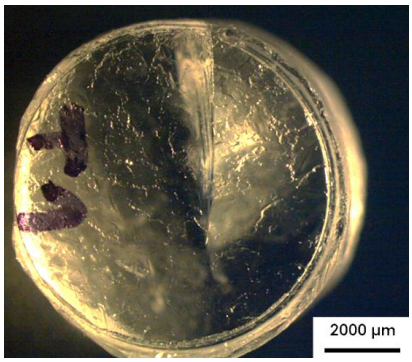

Figure 89: A stereomicroscope image of one of the Perspex samples produced

6.3.4 Corroded Samples

With the CT scan confirming that the defects in the discs (Figure 62, Figure 73) had propagated through the full depth of the stainless steel, tests using the fluid flow rig were undertaken using the same methodology as the pinhole and slit discs discussed earlier. Unlike the pinhole and slit discs which were so thin a backing plate was required to prevent rupture and deformation, these discs were able to withstand the pressure difference without deformation.

Following the same methodology as was used to obtain the results from the pinhole and slit discs, the different corroded samples were tested. The results of these tests are shown in Figure 90.

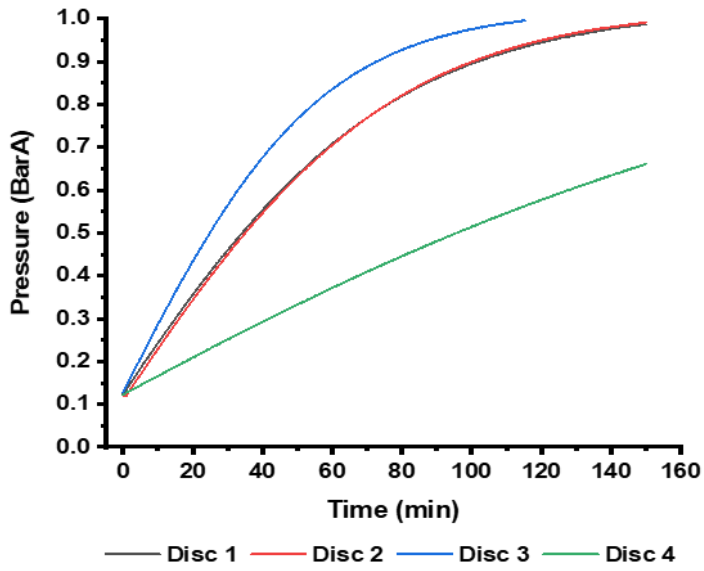

Figure 90: The results of the return to atmospheric tests undertaken using the discs featuring the corroded crack discs.

Given the nature of the cracks a large degree of variation was expected depending on the crack morphology and width. It is therefore interesting that the results for Disc 1 and Disc 2 are so similar.

6.4 Summary

The simplified fluid flow rig proved to be a repeatable means of determining the flow through the pinhole and slit discs with multiple tests being performed and very little variation seen despite the tests being conducted independently. When testing the discs, some unexpected results were measured with the 10 µm diameter pinhole returning to

atmospheric pressure faster than the 20 μm across multiple, independently set up and performed tests all showing the same result.

While the attempts to produce defect pathways using Perspex did not work, it is expected that with some changes to the technique to ensure that there was no surface deformation it is possible a viable sample could be constructed.

When the corroded discs were tested, the same level of repeatability was found. This testing also showed that the defects spotted using the microscopy techniques and CT scans were pathways which gas could flow through.

7 Vacuum Drying Through Defects

In order to provide validation to the flow model and to assess the effectiveness of vacuum drying as a process to be used to dry any spent fuel, tests need to be conducted using the defects. This chapter will cover the tests undertaken using initial testing samples featuring a drilled hole along with the tests undertaken using the discs purchased from Edmund Optics. Finally, the chapter will cover the tests performed using the defects produced as part of this work.

7.1 The Vacuum Drying Rig

7.1.1 First Generation Rig

First built by *J. Goode*, the rig consists of a vessel constructed from a 2.5” section of stainless steel pipe with one end capped with a dome which was welded into place, and the other end attached to a flange (25). The lid of the vessel, was made from a second flange was constructed with multiple lines to allow for both vacuum and flowed gas drying to the conducted. A PXM319 pressure transducer from Omega was installed, with a 0-2 BarA range for the vacuum drying. K-type thermocouples, one attached to the vessel and the other left loose in the vessel chamber and could be attached the external surface of a sample. To provide external heating to the samples a 4” Mineral Insulated band heater along with a temperature controlled were acquired from Watlow. To measure the flow a Bronkhorst High-Tech B.V. series mass flow meter is connected to the vacuum line. This provides a percentage reading for the gas flow based on 100% being equal to 1.997 g/min of air. This, therefore, cannot be used for obtaining a direct measurement of mass flow but it is suitable for providing an indication of the flow being experienced.

The initial work carried out on the vacuum drying rig was conducted using the set-up as shown schematically in Figure 91 and in a photograph in Figure 92. This had undergone a slight modification since its initial construction by *J. Goode*. These modifications were made by *M. Jackson* for his project and involved removing the condenser which was present and the addition of a heating wire and insulation covering the line in order to prevent the condensation of the vapour in the pipework.

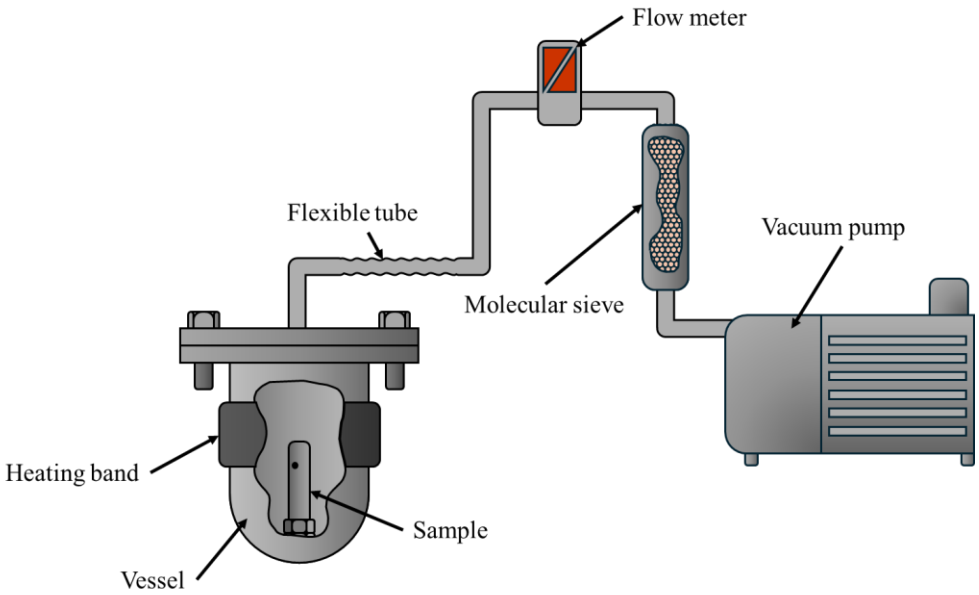

Figure 91: Schematic of the vacuum drying rig.

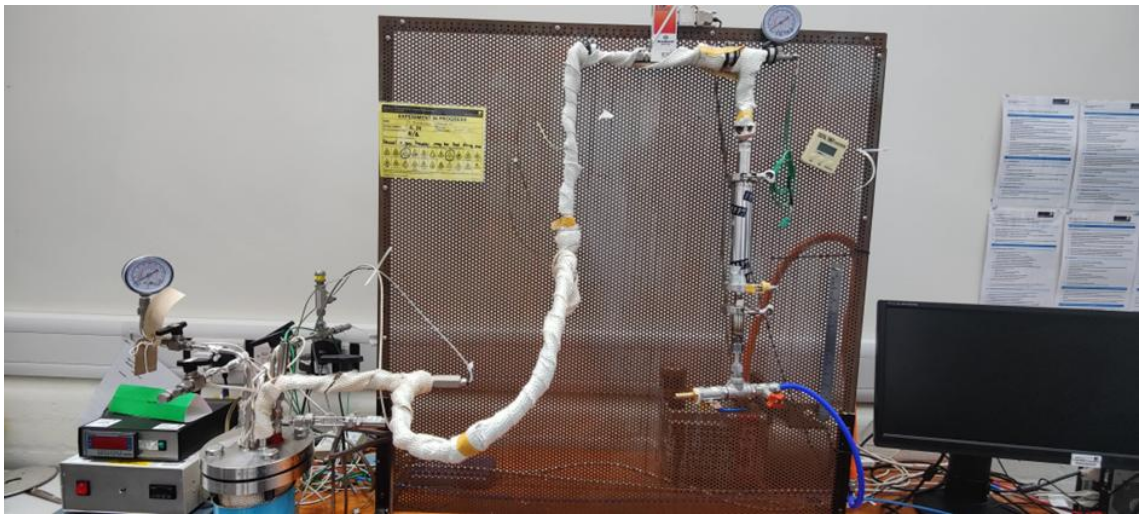

Figure 92: The first generation vacuum drying rig built by J. Goode.

7.1.2 Second Generation Rig

The first generation of the drying rig presented several challenges to the efficient operation and was more limited in its capacity for data collection. The upgrades to the rig sought to fix this. The first change was to simplify the pipework on the rig to reduce to points at which condensation could occur and result in pools of liquid water building up as this would give inaccurate readings in the instrumentation. This was achieved by building the vacuum line vertically out of the lid for as short a length as possible before the line turns and heads on a five-degree slope down to the molecular sieve. In addition, the line was heated by a heating wire reaching a temperature of 70°C, ensuring no condensation occurred. Secondly, the flexible hose was removed as this was a suspected

site of condensation and pooling of liquid water. On the first generation of rig, this flexible hose was required in order to remove the lid of the vessel to access the internal volume of the vessel and the sample inside. This was a slow and cumbersome process, so to speed up the operation an electric lab lift was added. This allowed for the lid of the vessel to be fixed into place and the vessel and associated components to be raised and lowered for access, greatly speeding up the set-up process. Finally, a sample line was added. This allows for the sample under investigation to be monitored throughout the experimental run as well as the internal temperature of the sample which was not possible before the upgrade. A schematic of the upgrades is shown schematically in Figure 93 and as a photograph in Figure 94.

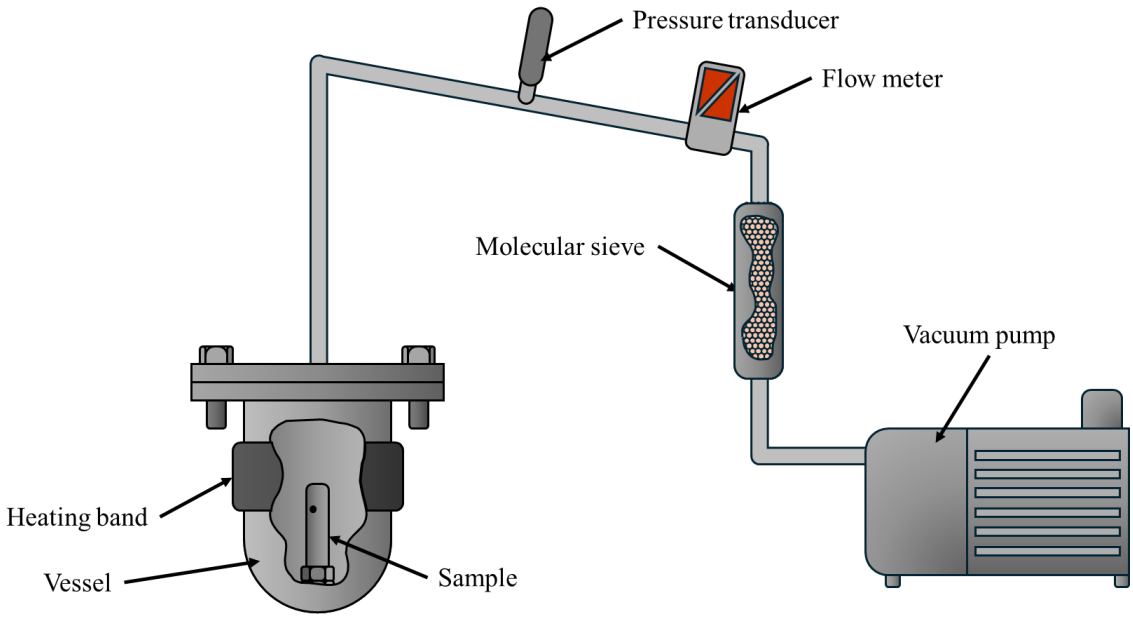

Figure 93: A schematic of the second generation of vacuum drying rig used for this work.

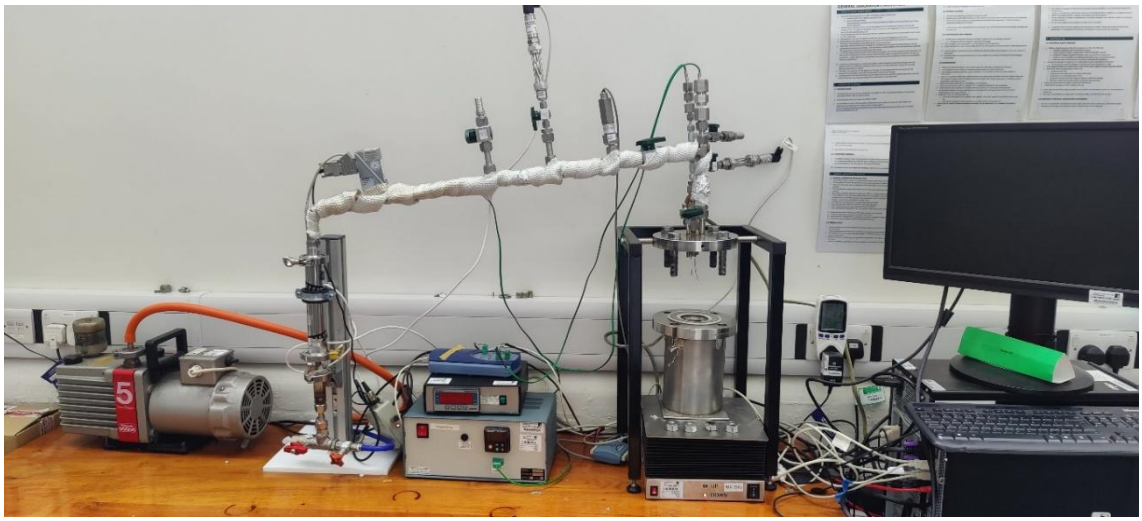

Figure 94: The second generation of the vacuum drying rig featuring the upgrades made by M. Jackson and M. Lovett with consultation from myself.

Some limitations found in the first generation of the vessel were unable to be rectified in the upgrade. Chief among these is that the vessel, being constructed from a large quantity of stainless steel has a large thermal lag, so the temperature moderation can be difficult. As the vessel was heated the low heat conduction of the stainless steel results in the heater supplying more thermal energy than required. By the time the thermocouple attached to the vessel logged the temperature of the vessel being at the desired point, the area around the band heater is several degrees above.

7.2 Methodology

This section will cover the methodology used for the vacuum drying tests. It is split into a general methodology which covers the basics of undertaking a test using the vacuum drying experimental rig with the subsequent sections of the methodology covering the adaptations made to the methodology for the different samples tested.

7.2.1.1 General Methodology

Initially the sample is placed into the vessel without any water present and left to reach the test temperature after which it is removed and weighed. During the period in which the sample is being heated, the molecular sieve can be dismantled and the sieve beads weighed before being returned or replaced and the sieve reassembled. If the molecular sieve beads have gained 15 g then they are considered saturated and will need to be replaced and regenerated before further use.

At this point the mass of water can be added to the sample which is then sealed. A thermocouple is then taped onto the sample and it is returned to the vessel, the vessel itself sealed and the sample monitored until it reaches the test temperature. Once the desired temperature has been reached, the data loggers are started and the vessel is then evacuated.

After the test has been concluded, either due to the desired time elapsing or the indications from the dataloggers showing that the sample has dried, the vacuum pump is switched off and the vessel and pipework isolated. The pressure is then monitored as a vacuum rebound test can be undertaken to assess if the sample is dry.

7.2.1.2 Loose Samples

For the tests undertaken using the loose samples, shown in Figure 95 and Figure 96, the test piece was placed with the Swagelok fitting on the base of the vessel leaving the sample stood upright. Care was taken to avoid the sample falling and coming into

contact with the edge of the vessel to prevent orientation being a factor in the tests however, upon opening the vessel at the end of the tests the sample was routinely found to be slanted and touching the wall of the vessel.

Figure 95: The first generation of loose sample constructed by M. Jackson featuring a 227 µm diameter pinhole drilled into a section of AGR cladding.

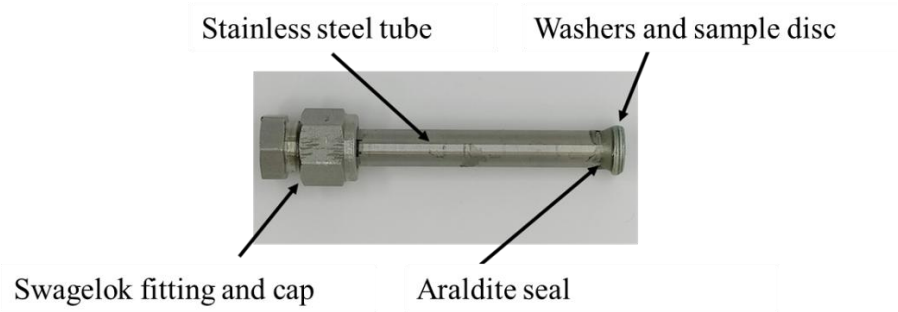

Figure 96: The second version of the loose sample design used to hold the pinhole discs purchased from Edmund Optics featuring an araldite seal.

The first generation of loose sample, shown in Figure 95, is formed from a 40 mm section of AGR cladding sealed at one end with a 25 mm section of stainless-steel tube and at the other, a 30 mm section of stainless steel capped with a Swagelok compression fitting. This fitting allows for the addition of water into the sample and then restricting the flow of liquid or gaseous water through the defect. In this sample that defect consists of a 227µm pinhole drilled through the cladding allowing for a comparison to work conducted by *J. Goode* and *M. Jackson* (25; 156).

For the second generation of the samples a smaller diameter defect was desired. To achieve this the pinhole discs purchased from Edmund Optics, an example of which is shown in Figure 82L. Initial samples were constructed using these discs measuring 0.1mm thick, constructed from stainless-steel, and with a diameter of 9.5mm featured were purchased with pinhole diameters of 1µm, 5µm, 10µm, 20µm, 50µm and 100µm. These discs were attached to a 8 cm length of stainless-steel tubing and a Swagelok

compression fitting attached to one end. Taking care not to block the pinhole, the disc was attached to the other end using Araldite.

During initial tests with these samples it became apparent that the Araldite alone was unsuitable for providing an air-tight seal between the discs and the tube. The pressure differential across the pinhole combined with the sample being heated resulted in the failure of the sample, either partially, with the disc peeling away from the tube or becoming detached entirely. To solve this, two washers, one either side of the disc, were fastened to the tube, again with Araldite. This proved effective at preventing the disc from separating from the rest of the sample construction. Though at higher temperatures the softening of the Araldite was still an issue. An example of one of these second versions of the samples is shown in Figure 96.

7.2.1.3 Hanging Sample

After the rig was upgraded, changes were made which would allow for the sample to be suspended from the lid of the vessel thereby eliminating the orientation and positioning of the sample as a variable to be considered. For these samples, it was also desired that the sample not be placed on the base of the tube to prevent the leakage of water through the defect during preparation. This resulted in the use of a Swagelok union tee section being used to house the disc. The samples are held in a similar fashion to the set-up shown in Figure 83. The lower portion of the tee was capped, as with previous samples to allow for a quantity of water to be added to the test piece. When used for testing, the sample can be attached to a sample line in the vessel itself in a change from previous samples which would rest in the vessel thereby allowing for pressure and temperature readings to be taken from inside the sample.

7.2.2 Testing

7.2.2.1 Key Features of the Vacuum Drying Plots

Despite the changes between experimental runs such as the size of the defect, the temperature and the mass of water added to the sample there are several features, highlighted in Figure 97, which are present across all the tests. These will be explained here to prevent repetition.

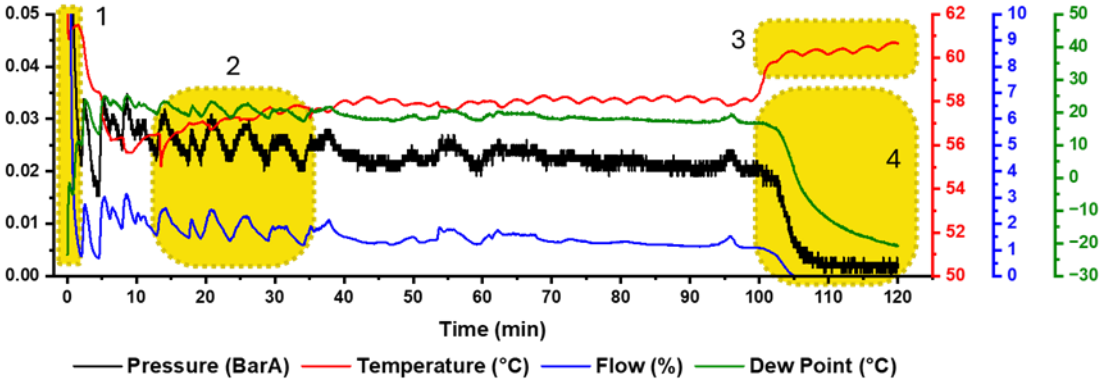

Figure 97: An example plot from a vacuum drying test with regions highlighted for discussion.

1) The initial evacuation of the vessel at the beginning of the experiment. The pressure decreases from atmosphere (1 BarA) and after an initial spike in the flow rate as the bulk of the air is evacuated, the flow rate decreases.
2) This region highlights the behaviour of the rig once the bulk of the air has been removed. In this region the relationship between the flow, pressure and dew point is seen. As some of the water is evaporated, this prompts an increase in the pressure. As the pressure increases, so does the dew point. At the same time, an increase in the flow rate is observed as the water vapour is removed.
3) In region three, the behaviour of the heater used to heat the vessel is shown. This applies across the test but this region was chosen to avoid overlapping with other features. Ideally the temperature of the sample and vessel would remain constant throughout the test however this is not observed, instead there is a “bounce” in the profile. It is theorised that this occurs due to the thermal lag caused by the large mass of stainless steel making up the vessel. The heating band is attached near the top of the vessel, however the thermocouple used to control this temperature is attached to the base of the vessel. This results in the vessel heating up beyond the desired temperature and then falling below this temperature before the heater can respond.
4) Unlike the other highlighted regions, this was not observed on all of the tests however, it was hoped that this feature would be seen. When the pressure, flow rate and dew point all drop off and do not show any signs of increases then it is a good indication that the sample has fully dried as no more water vapour is being detected by the flow meter and the pressure has reduced below the baseline while the drying was occurring.

7.2.2.2 Initial Tests

A range of tests were performed starting with a mass of water in the base of the vessel, not contained within a test piece at a variety of temperatures, 40°C, 50°C and 60°C to assess the unhindered drying rate and to ensure the rig worked as expected. Following this, tests were performed using the sample shown in Figure 95. This sample was used to gain familiarity with the rig and to provide corroboration with results obtained by *J. Goode* and *M. Jackson* (25; 156).

7.2.2.3 Tests with the Pinhole Discs

Following the construction of the first generation of pinhole disc samples tests with approximately 2 g of water being added to the sample prior to the drying test being performed with this sample tested at 40°C, 50°C and 60°C. The second generation of test samples, such as that shown in Figure 96, featuring the washers, were also tested but at a greater range of temperatures – up to 90°C set on the temperature controller.

7.2.2.4 Commissioning of the Upgraded Drying Rig

To commission the upgraded drying rig, basic tests were performed by *M. Lovett* focusing on different approaches that could be used and testing to see whether the rig behaved as expected (157). Initial testing was undertaken with a bulk water test with further testing performed using a loose sample as was used prior to the upgrades to the rig and with the sample fixed to the lid using the new sample line attachment. Finally, several tests were carried out to assess the effectiveness of an air bleed approach.

7.2.3 Analysis

To assess the drying trials, all the data gathered is exported into csv or txt files. These are then imported into excel and a time stamp (in seconds) added. As each piece of logging software is started in sequence an offset is added to ensure the traces match up with each other. Once aligned, the data is trimmed to remove the downtime at the beginning before the vacuum pump is started and at the end while the experiment is being terminated and the logging software stopped. At this point, there are four different data sets to plot; pressure, dew point, flow and temperature of the sample. In the upgraded rig, a fifth data set was added, the temperature inside the sample. As Microsoft Excel is only capable of plotting graphs with two vertical axis ,the data is transferred to

7.3 Results and Discussion

This section will cover selected results obtained from the vacuum drying trials highlighting key features and discussing the trends seen across the tests.

7.3.1 Large Defect Sample

Testing of the sample shown in Figure 95, 7g of water was loaded into the sample and the system was left to reach the test temperature of 60°C. Once the sample temperature had stabilised the vessel was evacuated. Figure 98 shows the results from this experiment. Of note with this test was the sharp drop off in the temperature at the beginning of the run which has been attributed to adiabatic cooling of the sample as the vessel was evacuated. Over the course of the experiment, the temperature does begin to recover however it is noted that the target temperature of 60°C was not achieved again during this run. During the initial evacuation of the vessel there is a large spike in the flow rate which is attributed to the air in the vessel being removed. Following this, there is a period of time where the water is being forced out of the sample via the expansion of the air also trapped within the sample. This phenomena was noted by *J. Goode* who reasoned that water was being forced out of the sample and pooling inside the vessel contributing to a increased baseline flow rate. Once this ejected water has been evaporated the flow rate would then fall and this drop off in the flow is observed here at around the 50 minute mark (25). The dominant behaviour after this drop off is the slug flow. This occurs when the water level is near to the defect. As the water boils, bubbles spit water towards the defect and a “slug” ejected and evaporated. This behaviour explains the sharp spikes in the flow observed from 50 minutes until approximately 80 minutes and shown in detail in Figure 99. After this point the flow, pressure and dew point are all observed to decrease substantially. With the lack of any further spikes in either the pressure or the flow which would indicate the presence of water remaining in the sample the test was halted and the sample weighed confirming the drying process had been accomplished.

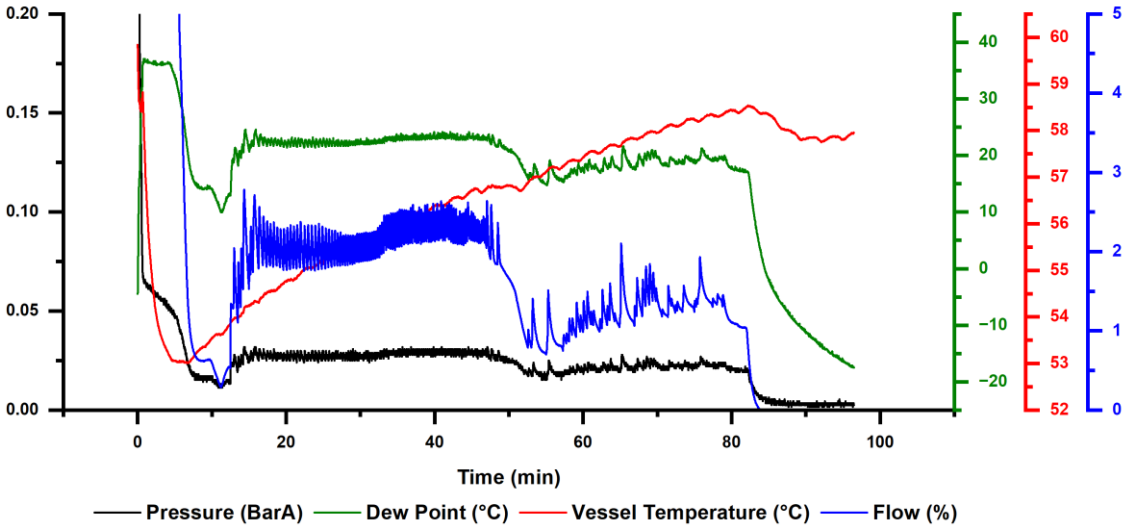

Figure 98: A test conducted at 60°C using the large defect sample (shown in Figure 95) using 7g of water and the first generation drying rig.

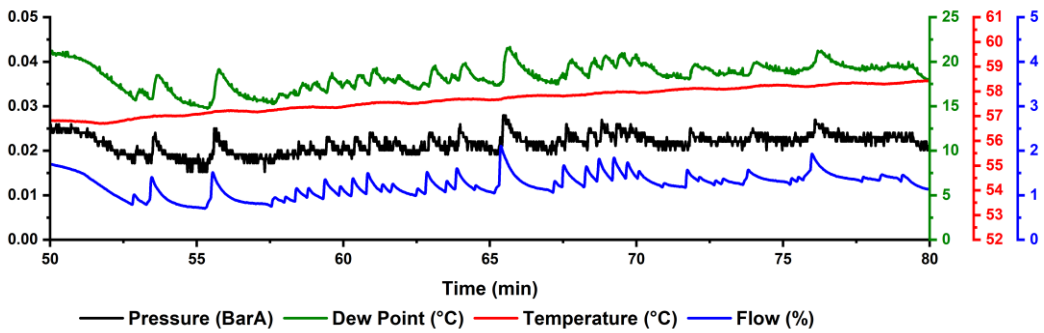

Figure 99: A cropped section of Figure 98 showing the period from 50 minutes to 80 minutes in detail.

In tests across multiple temperatures, as shown in Table 16, a consistent drying rate of approximately 0.02 g/min was achieved. While the increase in temperature was expected to result in an increase in the drying rate, the sample cooling observed and the slow recovery likely contributed to the consistent rate observed across all the tests.

Table 16: A summary of the tests undertaken using the large defect sample (Figure 95) detailing the temperature of the test, the mass of water added, the duration of the test and the drying rate determined.

Temperature (°C)	Mass of Water (g)	Duration (min)	Drying Rate (g/min)
30	7.041	123.83	0.021
40	7.027	123.50	0.015
50	7.037	120.58	0.018
60	7.023	124.83	0.023

7.3.2 Pinhole Discs

The first generation of pinhole disc samples, as discussed earlier, are composed of a short length of stainless steel tube with a Swagelok fitting and cap on one end and the pinhole disc sealed on with Araldite on the other.

During testing with these samples various concerns were raised. In a test of the 1 µm diameter pinhole disc, the indications from the data being graphed in real time suggested that the sample had fully dried within 60 minutes of the test starting. The data from this test is shown in Figure 100. With the equivalent test being performed using the large defect sample - Figure 95 – which took 80 minutes to dry the test was halted and the sample weighed. This confirmed that the sample was indeed dry. After examining the sample to confirm that the Swagelok fitting had been correctly installed and the cap suitably tightened, focus turned to the disc itself. Here it was noted that one portion of the disc had become separated from the stainless-steel tube. This likely led to the faster than expected drying time. During a test of the one micron diameter pinhole, the results of which are shown in Figure 100, three spikes were observed in the flow rate with very little flow recorded otherwise. Examination of the sample afterwards determined that the disc had almost fully detached from the rest of the sample. As a result of the frequent failures of these samples and the potential for undetected failure it was decided to discount the results obtained using this sample design.

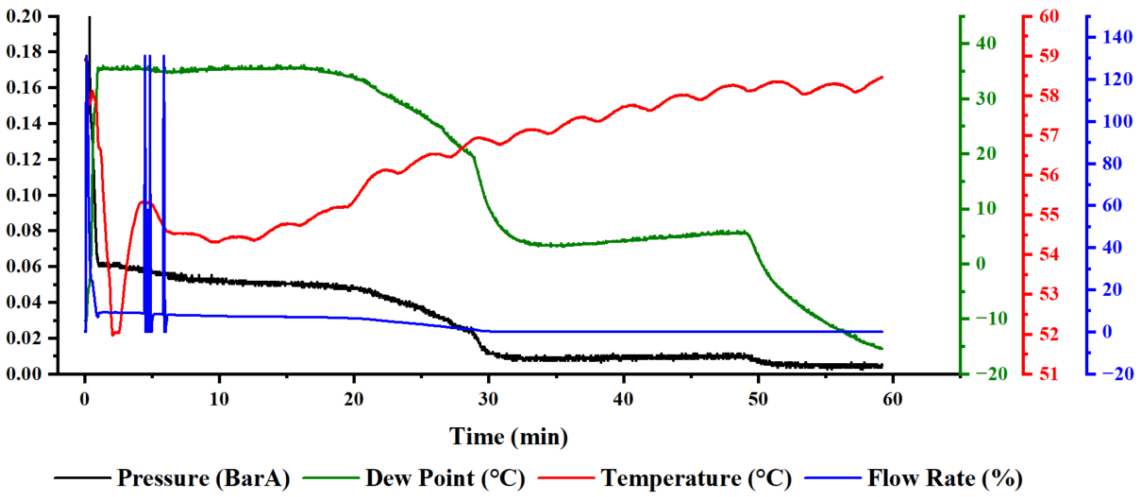

Figure 100: A graph showing the pressure, dew point, sample temperature and flow rate for a test conducted using the first generation of pinhole disc samples. The 1 micron diameter pinhole disc was used with the vessel temperature set to 60°C

After re-enforcing the discs by sealing them between two washers and then onto the tube further tests were undertaken. For the tests shown here - Figure 101, Figure 102

and Figure 103 - each sample was loaded with 2g of water and the vessel was set to 60°C.

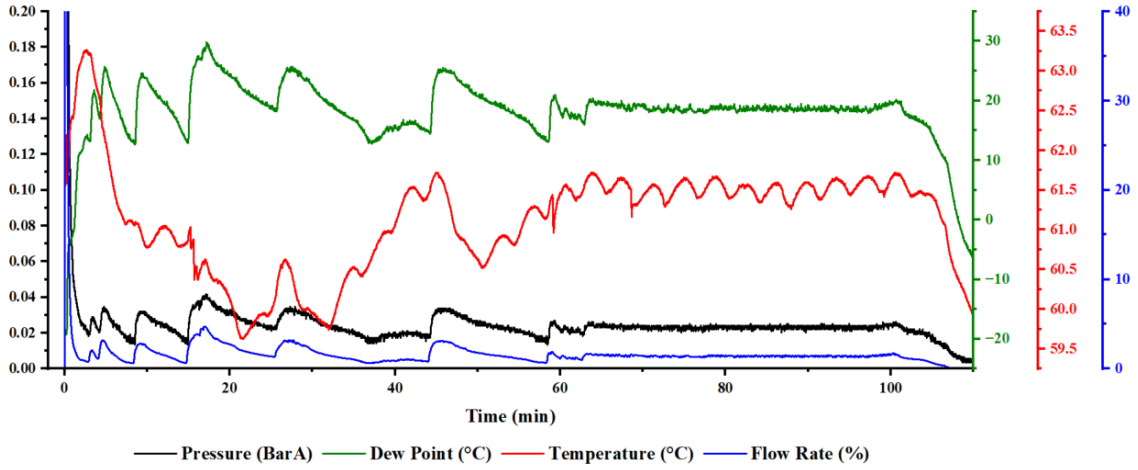

Figure 101: A graph of the pressure, dew point, temperature and flow rate of a test conducted using the second generation of pinhole disc samples. The 10 micron diameter pinhole disc was used with the vessel temperature set to 60°C

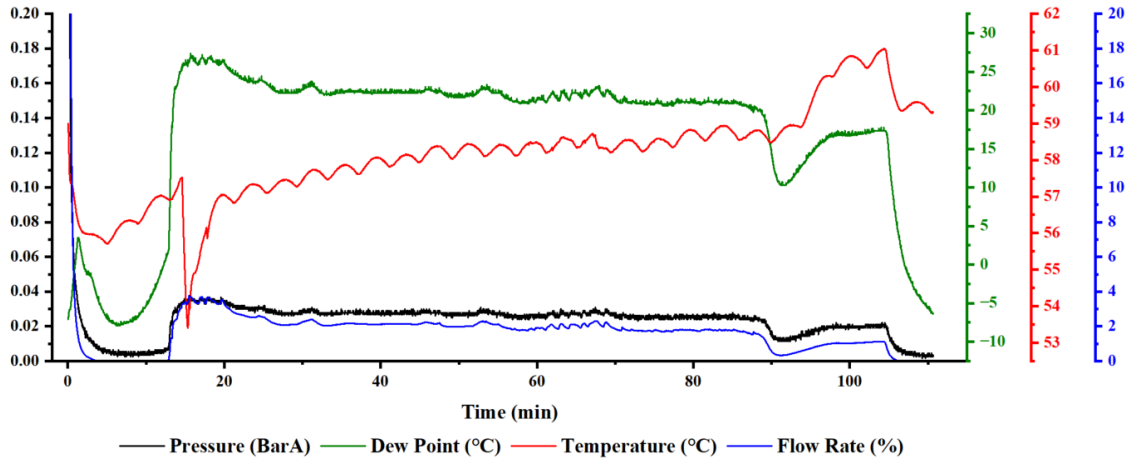

Figure 102: A graph of the pressure, dew point, temperature and flow rate of a test conducted using the second generation of pinhole disc samples. The 20 micron diameter pinhole disc was used with the vessel temperature set to 60°C

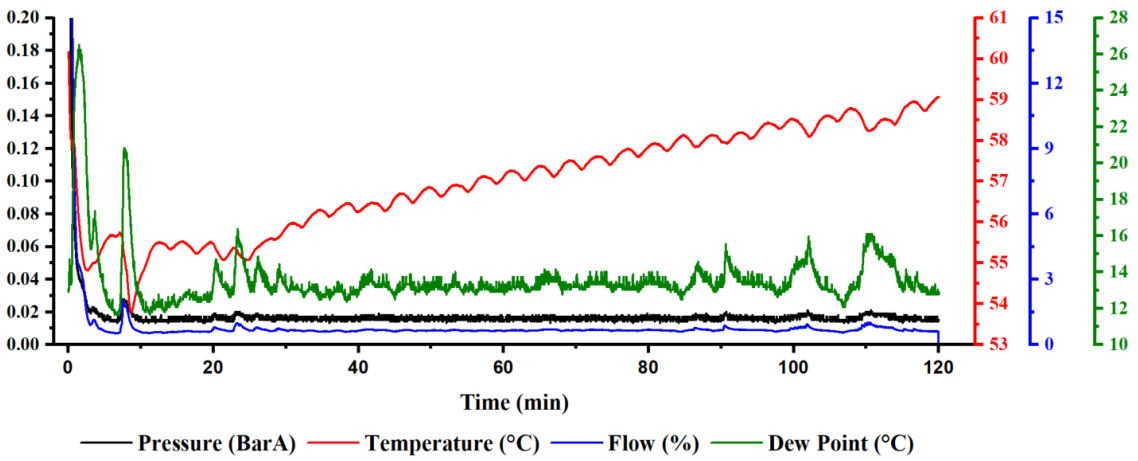

Figure 103: A graph of the pressure, dew point, temperature and flow rate of a test conducted using the second generation of pinhole disc samples. The 50 micron diameter pinhole disc was used with the vessel temperature set to 60°C

Comparing these three tests we see that for the 10 µm and 20µm the sample dried in a similar time. However, when the 50 µm sample was tested (Figure 103) was not dry after the same duration under the same conditions. There was no obvious damage to any of the samples tested that would contribute either to a faster than expected drying time for the smaller diameters or that would lead to slower drying for the 50 µm.

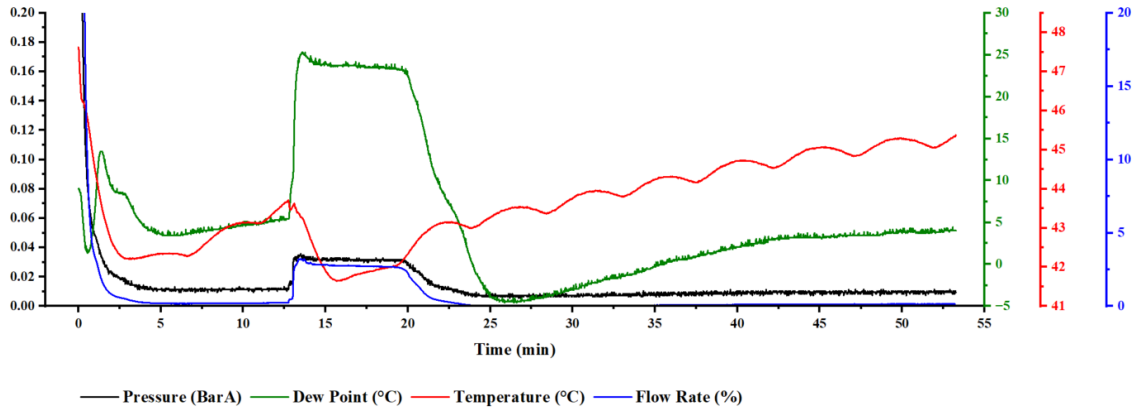

Figure 104: A graph of the pressure, dew point, temperature and flow rate of a test conducted using the second generation of pinhole disc samples. The 100 micron diameter pinhole disc was used with the vessel temperature set to 50°C

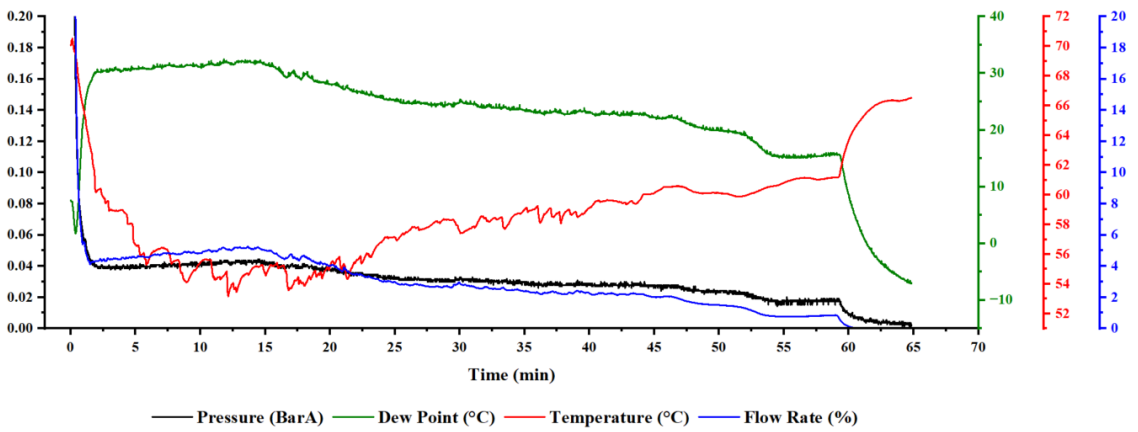

Figure 105: A graph of the pressure, dew point, temperature and flow rate of a test conducted using the second generation of pinhole disc samples. The 100 micron diameter pinhole disc was used with the vessel temperature set to 70°C

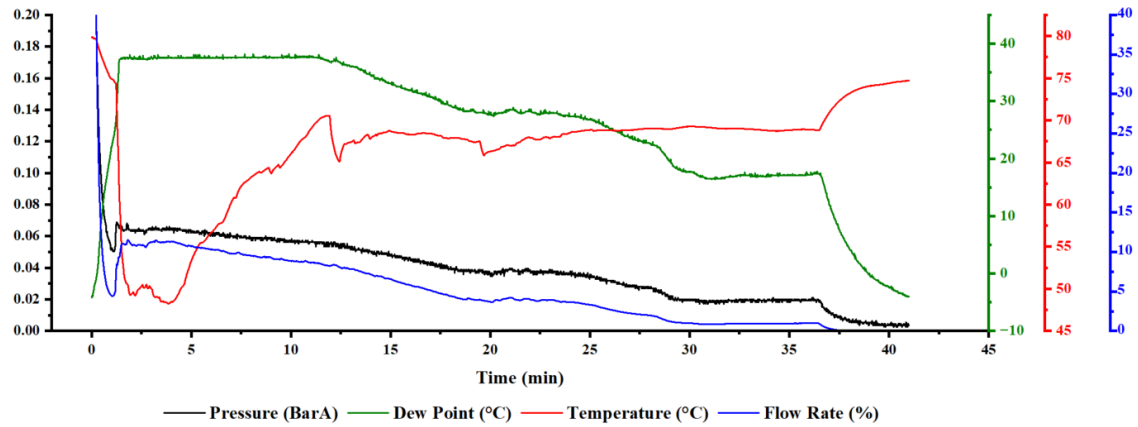

Figure 106: A graph of the pressure, dew point, temperature and flow rate of a test conducted using the second generation of pinhole disc samples. The 100 micron diameter pinhole disc was used with the vessel temperature set to 80°C. The first run with these conditions.

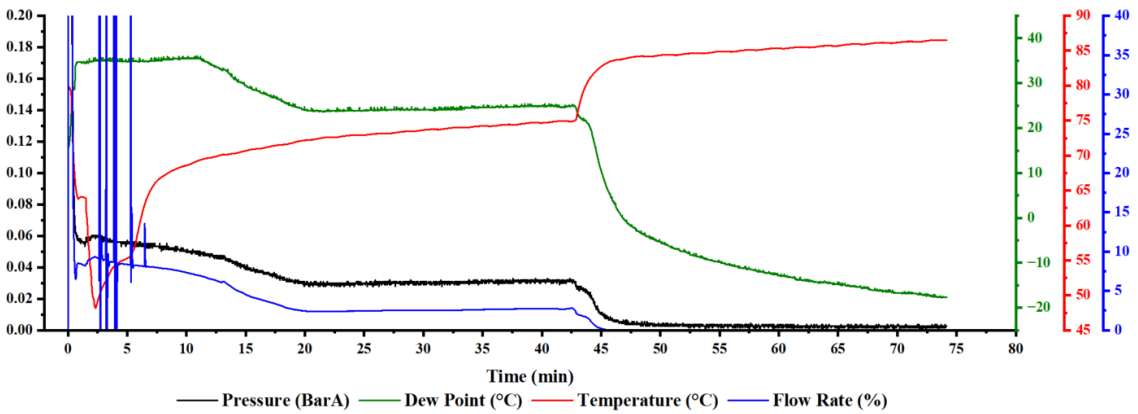

Figure 107: A graph of the pressure, dew point, temperature and flow rate of a test conducted using the second generation of pinhole disc samples. The 100 micron diameter pinhole disc was used with the vessel temperature set to 80°C. The second run with these conditions.

Figure 104, Figure 105, Figure 106 and Figure 107 show the impact of temperature on the drying rate. Prior to the tests being performed it was expected that by increasing the temperature, the drying rate would be increased. However, as seen in Figure 104, Figure 105, Figure 106 and Figure 107 this was not the case with the drying time being roughly equal for all the tests undertaken. The second 80°C test, Figure 107, shows the same spikes in pressure that were seen when the previous generation of sample (without the washers) failed - Figure 100. Upon examination of the sample it was found to have shifted in the vessel and come into contact with the vessel walls. The elevated temperatures compared to the previous tests and the direct contact of the araldite to the vessel wall resulted in the washers and disc detaching from the tubing.

When compared to the tests performed using the drilled, 227 µm diameter hole sample (Figure 95), there is a notable change in the drying behaviour. This was attributed to the

change in the position of the defect shown schematically in Figure 108. In the 227 µm defect sample, the location on the side of the tube allows for the behaviour described in Section 7.3.1. In contrast, by mounting the defect at the end of the tube, the samples used here will not demonstrate the first two regimes the other approach does. In this sample design, as there is no water above the defect, the increased pressure in the sample during the initial evacuation is unable to force out any water giving that initial high flow rate once the vessel has been evacuated. In addition to this, it is considered unlikely that any water will be lost as a "slug", as theorised by *J. Goode* and considered likely to occur when the water level is just below the defect location. Therefore, all the water lost from this sample set-up will occur through evaporation. This approach can also be accomplished by adding less water to the 227 µm diameter defect sample.

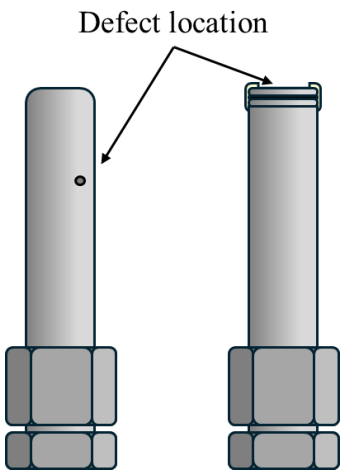

Figure 108: Schematic of two of the different sample designs used. (L) The large defect sample shown in Figure 95 with the defect located on the side of the tube. (R) The sample design used for the pinhole discs.

In order to accurately assess the impact of the temperature on the drying rate, the 20 µm pinhole test piece was loaded up with 2 g of water and drying experiments performed at 50 °C, 60 °C, 70 °C and 80 °C. For the lower temperatures, it was decided that a mass measurement would be taken every 30 minutes while this would be reduced to every 10 minutes for the tests at 70 °C and 80 °C owing to the reduced drying time. Figure 109 shows the results of this test, plotting the mass of water remaining as recorded at intervals. In order to take the mass measurements the test had to be halted, returned to atmospheric pressure while the sample was removed, weighed and re-inserted. After the mass measurement was taken and the sample was returned to the vessel and left to return to the test temperature prior to the evacuation of the vessel. This likely introduced some error in the results, especially at the hotter temperatures where more evaporation

will have occurred when the sample was not under vacuum. However, this is not expected to have resulted in a significant error.

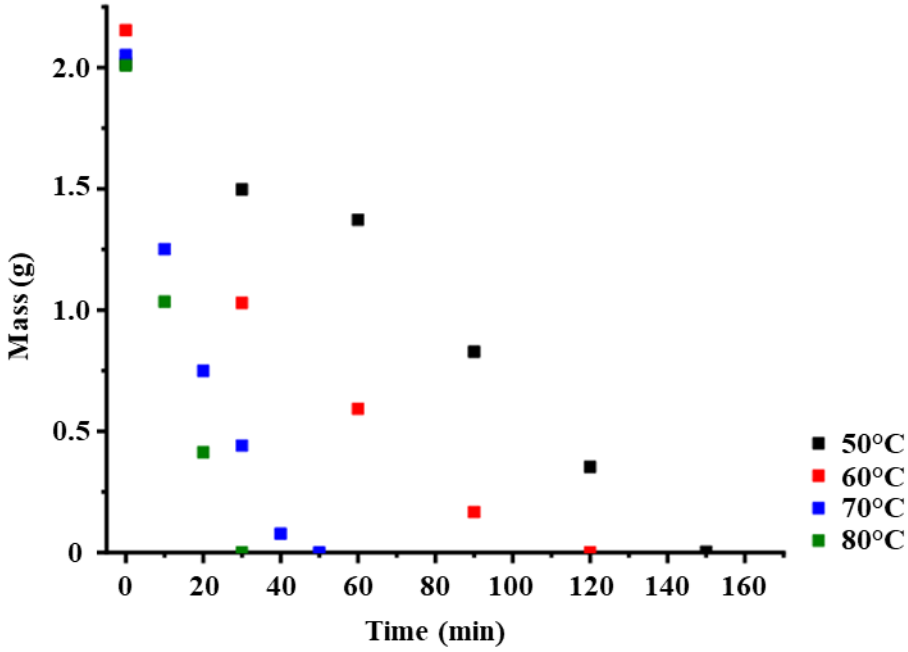

Figure 109: A scatter plot showing the mass of water remaining in a second generation pinhole disc sample over the duration of a test. This test was undertaken using the 20 µm diameter pinhole and 2 g of water

7.3.3 Commissioning of the Upgraded Drying Rig

With the upgrade to the vacuum drying rig - Figure 94 – completed, a set of commissioning tests were undertaken with these summarised in Table 17. These were primarily designed to provide a point of comparison to the original design of the vacuum drying rig - Figure 92.

The first test consists of a 10 g mass of water being placed into the vessel and not contained within a test piece. The result of this test gave a drying rate of 0.12 g/min with this sitting at the top end of the range of drying rates calculated by *J. Goode* although it should be noted that the result gathered here were achieved at a higher temperature (25).

Table 17: Summary of tests undertaken to commission the upgraded drying rig. Tests designed and undertaken in conjunction with M. Lovett (157).

Method	Mass of Water (g)	Temperature (°C)	Drying Rate (g/min)
Bulk Water	10	60	0.12
Loose	2	100	0.018
Fixed	7	60	0.021
Fixed	7	80	0.021
Fixed	2	80	0.007
Single Bleed	2	80	0.006
Multi Bleed	2	100	0.009

Having shown that the rig was successfully operating and able to handle a large mass of water, tests with samples were performed. The first of these was to test a pinhole sample left loose in the bottom of the vessel in a similar fashion to tests conducted prior to the upgrade to the rig. The result of this is shown in Figure 110.

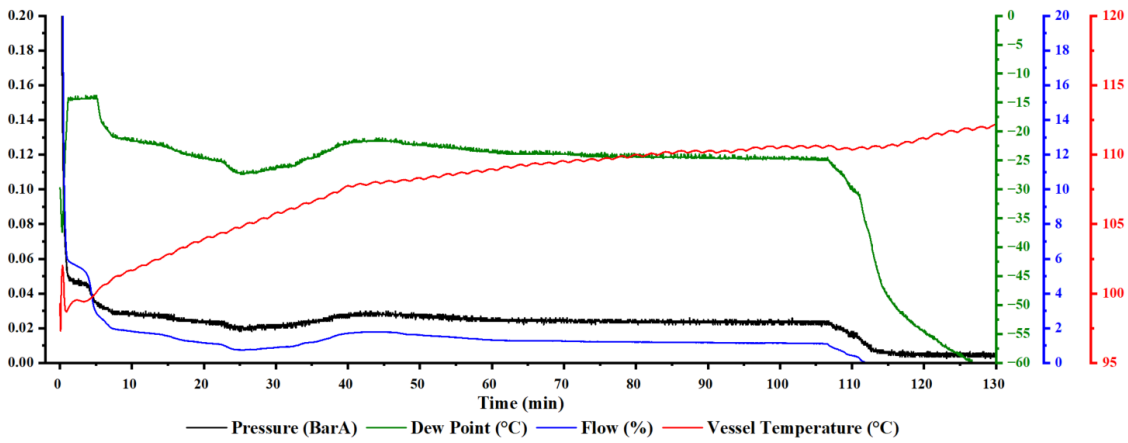

Figure 110: Testing of a sample loaded with 2g of water left to rest loose in the bottom of the vessel. The vessel was set to 100 °C. The pressure recorded in this test is the pressure in the vessel.

The tests conducted with this sample showed a similar drying rate to the tests conducted prior to the rig upgrades however it was noted that the pressure, flow and dew point displayed no indication of the spikes seen in previous tests undertaken. However, the flow, pressure and dew point did drop off in the style that indicated the sample was fully dry. This was confirmed by weighing the sample.

Testing then turned to commissioning the approach that is envisioned to be used going forward when using the upgraded rig. In these tests, the 227 µm was attached to the new mounting point on the lid of the vessel once loaded with water and left to reach the test

temperature before commencing the drying trials. The result of which is shown in Figure 111. As with the samples used prior to the rig upgrade, an initial drop in the temperature is observed before it recovers. However, unlike previous tests, the temperature then decreases across the test rather than remaining at or near the set point. Additionally, the tests undertaken with this sample were seen to exhibit the same pulsed behaviour as prior to the rig upgrade and that isn't seen with the pinhole discs. This suggests that either the defect location is a contributing factor to the pulses or that the defect size is responsible.

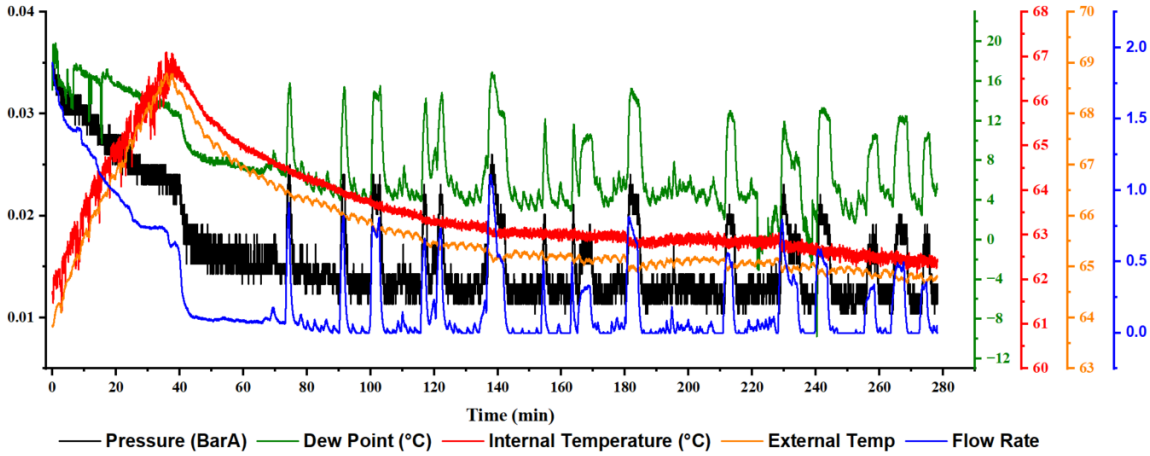

Figure 111: A test of the 227 micron diameter defect sample attached to the lid of the vessel in the style that would be used going forward with the rig. The vessel was set to 80 °C.

The final batch of experiments conducted were so called "bleed" tests. It was suggested by *M. Lovett* that the reduced drying rate observed from the suspended samples could be due to the initial temperature drop and the struggle to recover and maintain the test temperature. Therefore, building on the work by *S. Saha et al*, conducted two tests where a small leak was introduced to the vessel allowing for increased heat transfer between the vessel and the sample (158). These bleed tests were conducted manually and therefore, unlike the work by *S. Saha et al.* the evacuation could not be achieved in a step-like manner. Therefore an adaption was made by *M. Lovett* to try to replicate the approach as best as possible. The result of the first test operating with a single bleed is shown in Figure 112.

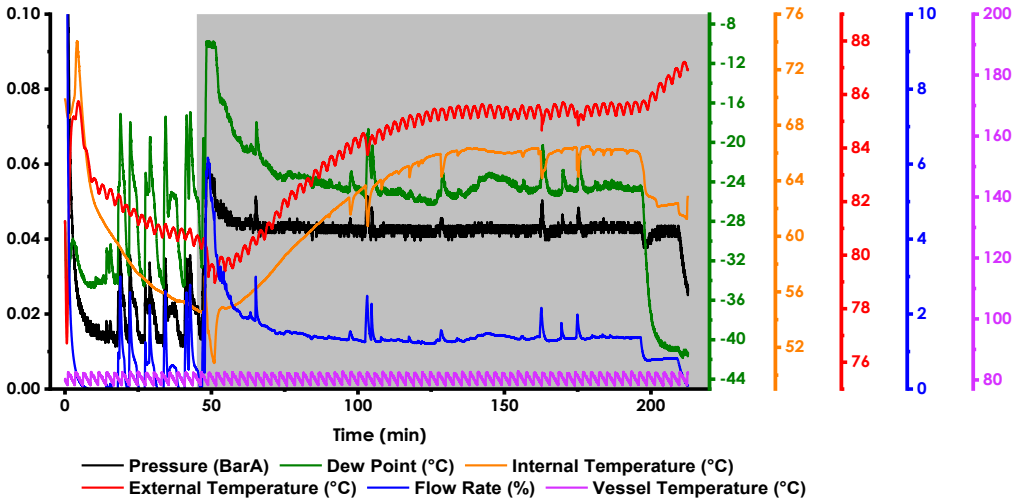

Figure 112: A bleed test conducted by M. Lovett. The vessel temperature is set at 100 °C and 2 g of water had been loaded into the sample. The grey shaded region denotes the period where the leak was introduced.

While this approach did allow for the temperature to climb and remain relatively steady for the remaining duration of the test it did not reach the 100 °C set point and the technique was determined to have not increased the drying rate as desired. A second iteration of this approach was also tested. In this iteration of the test, shown in Figure 113. This time, the vessel was evacuated and the flow allowed to settle before a leak was introduced. The vacuum pump was kept on throughout the test. After the sample returned to the test temperature the valve was closed and the bleed process stopped resulting in the vessel being evacuated again.

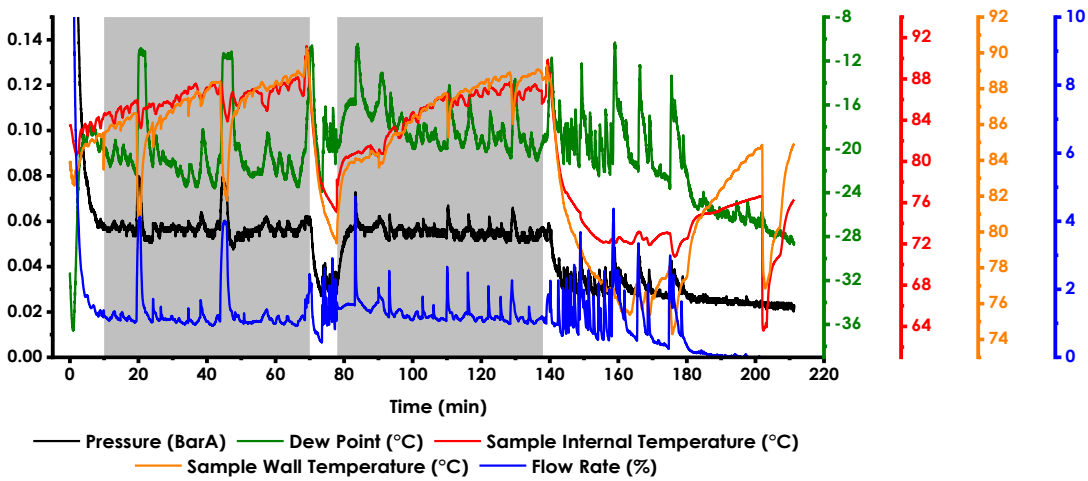

Figure 113: A multi-bleed test undertaken with the vessel temperature set to 100 °C and 2 g of water loaded into the sample. The grey shaded regions denote the periods where the bleed leak of air was in progress.

This approach resulted in an increased drying rate, though still lower than the samples left in the rig loose. While the approach showed some promise the rig would require further upgrades in order to ensure any test undertaken following this method was

repeatable as with the rig in its current set up the bleed was introduced manually by opening a valve.

Comparing the results achieved with the commissioning, and detailed in Table 17, to those from *J. Goode*, using the original design of the rig where drying rates in the range of 0.0095 g/min to 0.011 g/min were achieved at 60 °C, the same test undertaken with the sample now suspended from the lid of the sample showed an increase in the drying rate to 0.021 g/min. One possible reason for this increase is the location of the defect. It is unknown as to the orientation of the sample used by *J. Goode* however it is likely that the Swagelok fitting was placed onto the base of the vessel leaving the defect towards the top portion of the sample tube. In the tests undertaken with the same sample here, the defect was located towards the base of the vessel which likely had some impact though the rig is likely still performing to the same effectiveness if not increased.

7.3.4 Corroded Samples

The final tests conducted as part of this work concern the vacuum drying through the corrosion defects produced – labelled as Disc 1-4 and shown in Figure 61, Figure 62, Figure 63, Figure 64, Figure 65, Figure 66, Figure 67, Figure 68, Figure 69, Figure 70, Figure 71, Figure 72 and Figure 73. Two tests were performed on each sample, with 2 g of water loaded into the sample each time. With the potential influence of the orientation and contact with the vessel walls it was decided that the sample would be attached to the lid of the vessel, this set-up is shown in a schematic in Figure 114.

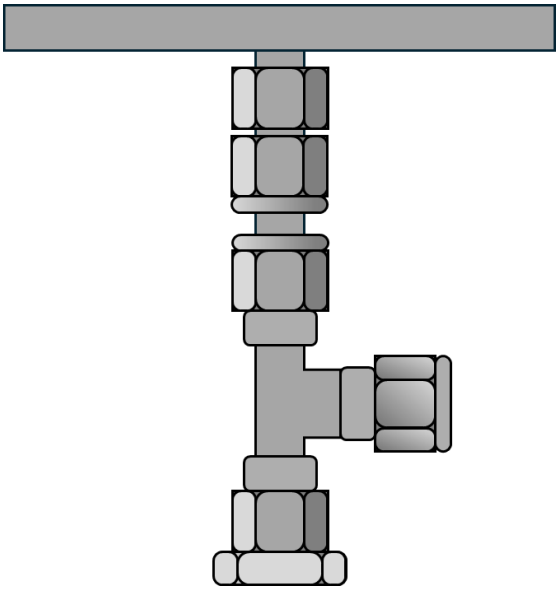

Figure 114: A schematic showing the set-up of the sample attached to the lid of the vessel. The sample to be tested is located in the right hand portion of the T-junction.

In commissioning the upgraded drying rig it was noted that the samples took a lot longer to reach the desired test temperature. This was attributed to the lack of conduction taking place between the vessel wall and the sample directly. This caused a concern that, with the elevated temperatures used in these experiments, the 120°C test in particular, that evaporation while the system is not under vacuum, would be a significant factor. Therefore it was decided that the samples would be left to heat up for an hour before starting the test.

In addition, due to the upgrades to the experimental set-up the internal pressure was able to be logged and it is this which is shown in Figure 115, Figure 116, Figure 117, Figure 118, Figure 119, Figure 120, Figure 121 and Figure 122.

Disc 1:

Unlike previous tests in which a decrease in the sample wall temperature was observed followed by the sample slowly returning to the test temperature over the course of the experiment, the 70 °C test, shown in Figure 115, displayed a rapid recovery to and then exceedance of the vessel set point. This rapid rise in the sample wall temperature was also observed in the 120°C set point test - Figure 116. In both tests, the pressure in the system was observed to increase during the test, this is not unexpected as the evaporation of the water in the sample will cause an increase in the vessel pressure. However, unlike other tests the increase in the pressure was sustained and constant rather than in spikes as seen with previous tests where the vessel pressure was measured. In the test at 120 °C (Figure 116) the pressure rise was noted during the experiment. With the live plot of the flow showing no flow through the system the heater was turned off and the system left to cool and the pressure also began to drop.

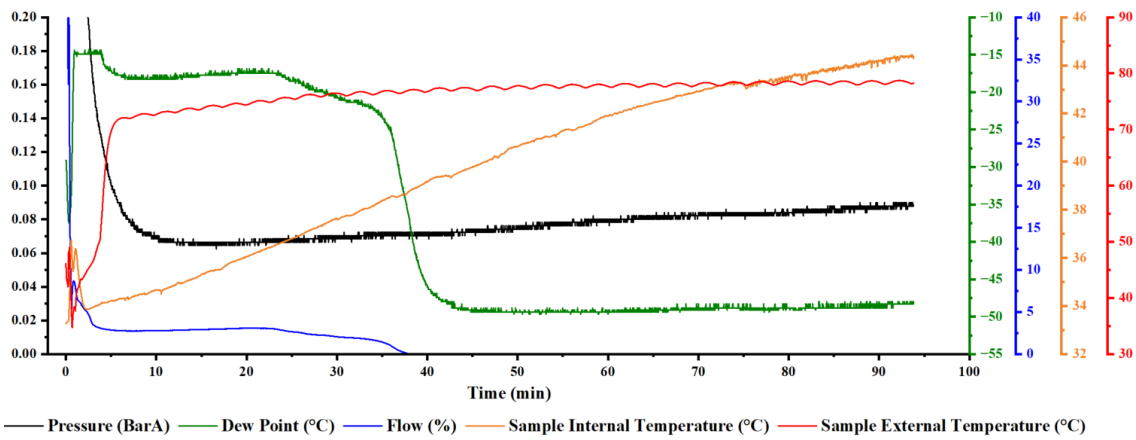

Figure 115: A vacuum drying test conducted with 2 g of water, disc 1 and the sample attached to the vessel lid. The vessel was set to a temperature of 70°C.

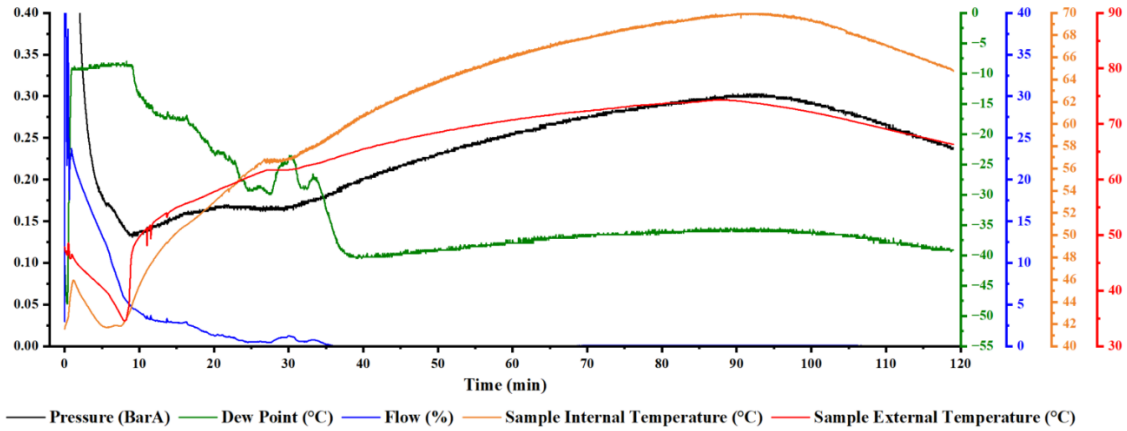

Figure 116: A vacuum drying test conducted with 2 g of water, disc 1 and the sample attached to the vessel lid. The vessel was set to a temperature of 120°C.

Disc 2:

As with the tests conducted on Disc 1, following the initial decrease in the pressure remained elevated for a period before dropping after 30 minutes. Following this a slight rise in the internal pressure was recorded on both the 70 °C test (Figure 117) and the 120 °C test (Figure 118). On each test however, the flow dropped to 0 % after 30 minutes. As with the 120 °C test using Disc 1, the heater was turned off after 110 minutes for the 120 °C test using Disc 2 and a similar drop in the temperature and pressure was observed.

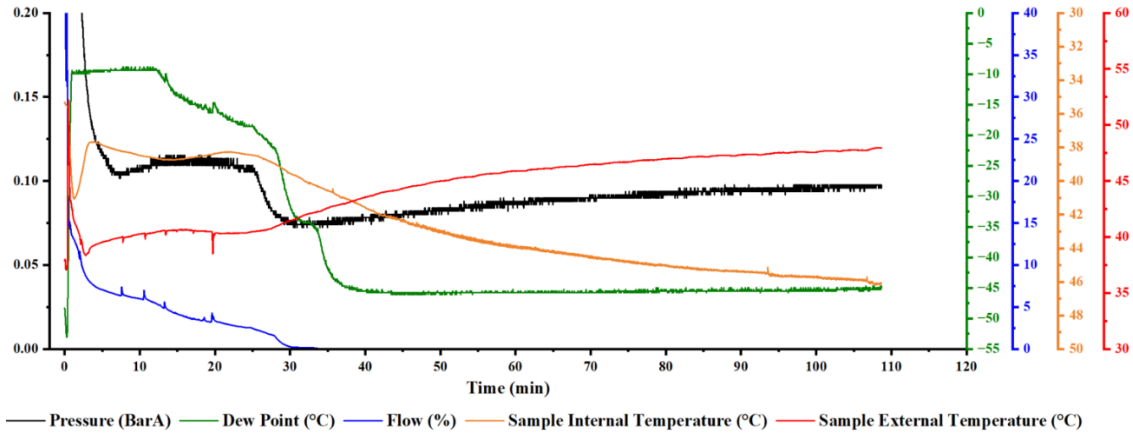

Figure 117: A vacuum drying test conducted with 2 g of water, disc 2 and the sample attached to the vessel lid. The vessel was set to a temperature of 70°C.

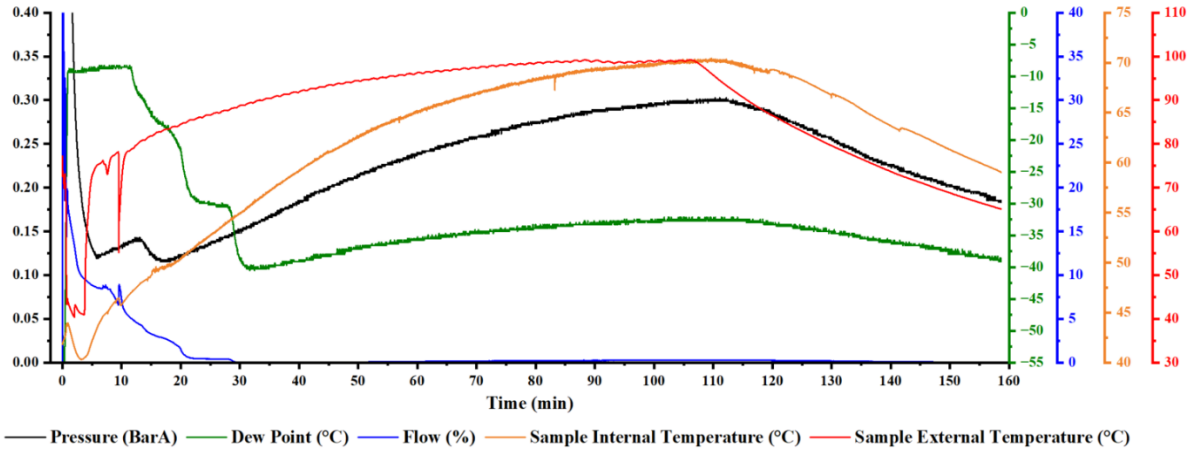

Figure 118: A vacuum drying test conducted with 2 g of water, disc 2 and the sample attached to the vessel lid. The vessel was set to a temperature of 120°C.

Disc 3:

The tests conducted on Disc 3 displayed similar behaviours to the prior tests conducted on Discs 1 and 2 with the flow dropping away to 0 % early on and an overall trend of the pressure in the sample increasing of the course of the test after an initial spike. When compared to the pressure increases seen in the 120 °C tests, the 70 °C both with this sample, as shown in Figure 119 and Figure 120 and the tests undertaken on Disc 1 and Disc 2, show a much more gradual increase in the internal pressure of the sample over the course of the experiment once the initial evacuation and pressure increase have passed. This suggests that some artefact or process taking place inside the crack network is blocking the channel and preventing the flow of water vapour from being evacuated. This is backed up by the faster and more pronounced pressure change seen in the 120 °C tests, as the hotter samples will result in an increased rate of evaporation. Additionally, a blockage would explain the false observation of fully drying that is presented from the plot of the flow rate.

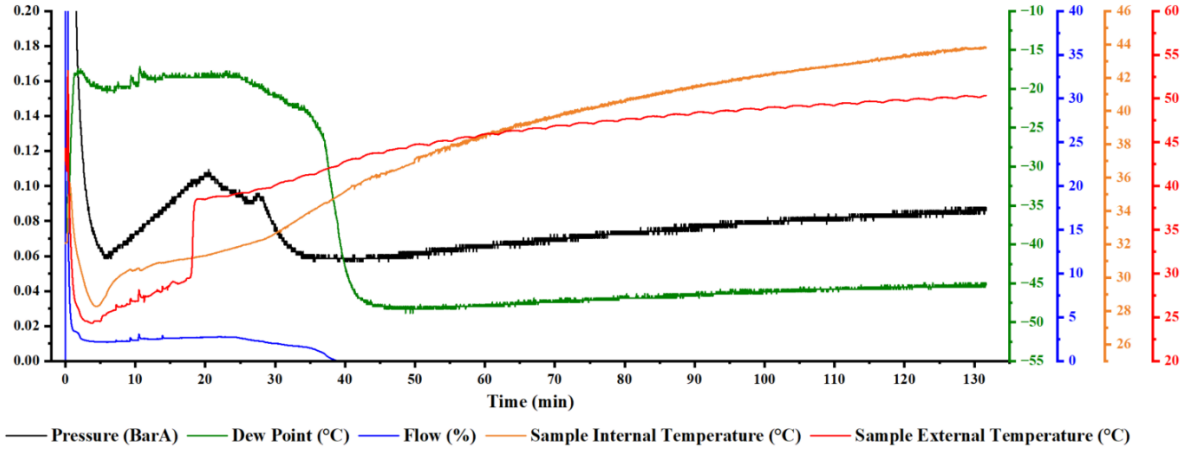

Figure 119: A vacuum drying test conducted with 2 g of water, disc 3 and the sample attached to the vessel lid. The vessel was set to a temperature of 70°C.

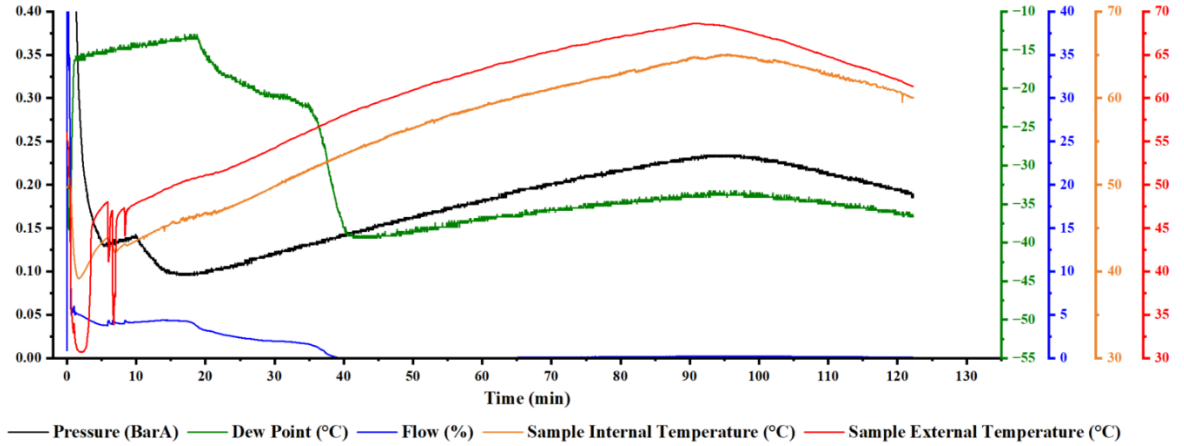

Figure 120: A vacuum drying test conducted with 2 g of water, disc 3 and the sample attached to the vessel lid. The vessel was set to a temperature of 120°C.

Disc 4:

The tests using Disc 4 showed different behaviour when compared to the others. In the test conducted with a vessel set point of 70 °C and 120°C, shown in Figure 121 and Figure 122 respectively, rather than the initial drop in pressure followed by a period of elevated pressure before a decrease and then a trend towards an increase in the pressure this disc there is an initial slow decrease before a smooth evacuation of the sample as would be expected if the vessel pressure was being logged on a leak test – i.e. no sample or drying taking place.

Furthermore, in the 70 °C test (Figure 121) a large increase in the dew point is present however no corresponding change in the internal pressure (a dip would be expected as some vapour leaves the sample) or increase in flow is observed. When the disc was

tested a second time with the vessel set to 120 °C, a longer initial slow decrease in the pressure was recorded followed by a decrease as expected. However, this decrease in the pressure was not as drastic as the others resulting in a higher baseline – 0.4 BarA compared to the 0.2 BarA low point in the 70 °C test. During this test – shown in Figure 122, several large spikes in the dew point occurred in the 40 minute to 75 minute range. Unlike changes observed in tests conducted with other Discs and indeed with this disc at 70 °C, this time a corresponding increase in the flow was detected though there is no discernible decrease in the internal pressure of the sample.

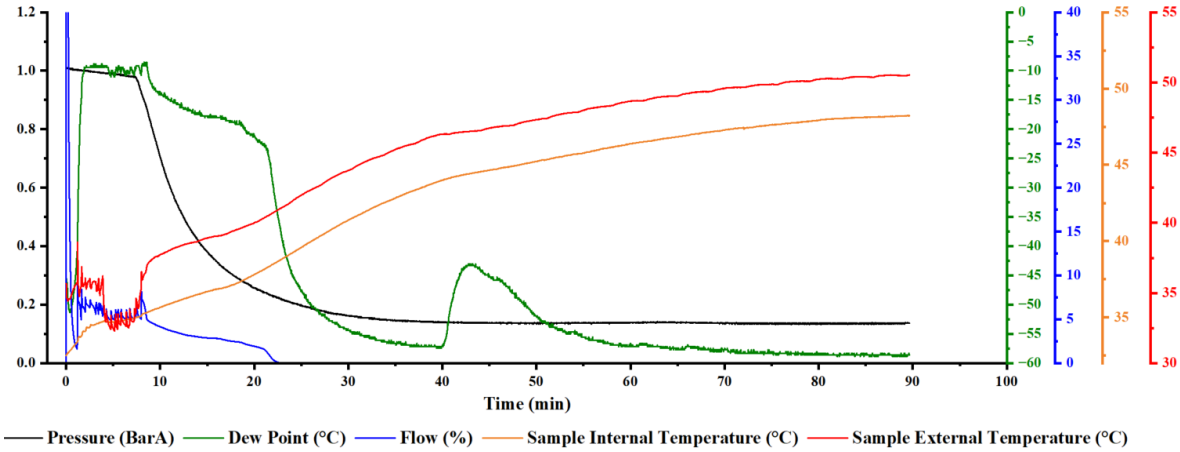

Figure 121: A vacuum drying test conducted with 2 g of water, disc 4 and the sample attached to the vessel lid. The vessel was set to a temperature of 70°C.

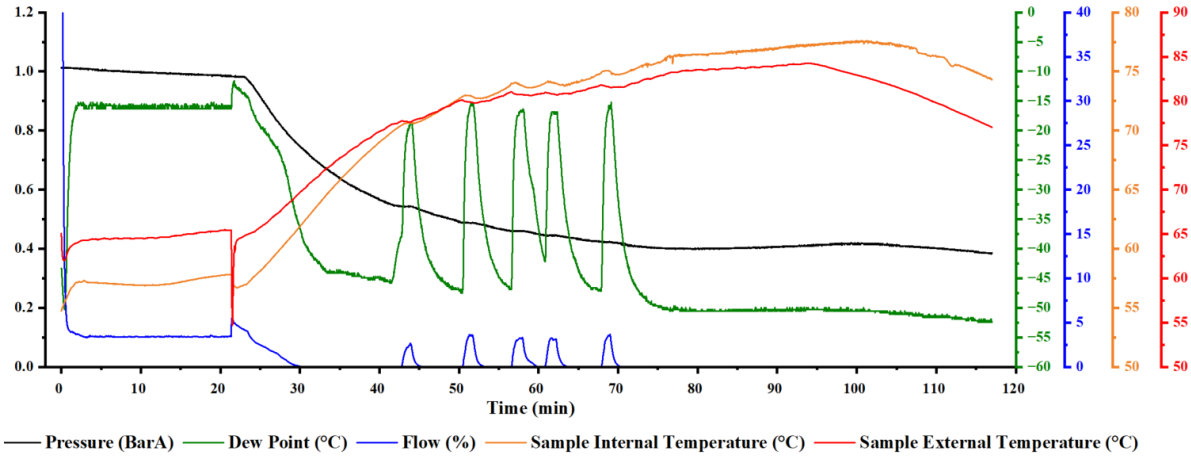

Figure 122: A vacuum drying test conducted with 2 g of water, disc 4 and the sample attached to the vessel lid. The vessel was set to a temperature of 120°C.

7.4 Summary

Initial tests undertaken with the vacuum drying rig in its first-generation set-up using the large defect sample - Figure 95 – showed behaviour which was observed in previous

work undertaken using this rig and sample. As some modifications had been made prior to undertaking this work, the presence of the drop off in the flow, pressure and dew point which indicated the sample was fully dry was reassuring as it provided a means of determining the progress during the testing.

Despite the initial problems which arose with testing the pinhole discs, the samples performed well and allowed for a comparison of the drying rate through the different sized defects. This sample design also eliminated two of the flow regimes identified by *J. Goode* where the water in the sample can be forced out of the sample by the expanding air as the vessel is evacuated. The second regime eliminated is the slug flow. In the large defect sample, this regime occurs when the water level is close to the level of the defect. By mounting the disc on the top of the tube this meant that the only flow of fluid through the defect was evaporated water vapour. This had the consequence of a smoother profile for the pressure though some spikes are still observed. This could be due to an intermittent, undetected failure of the sample however this is deemed to be unlikely as the disc was reinforced by the addition of the washers for these tests. This was a known issue with the first generation of pinhole disc samples hence the construction of the second generation of test piece.

After the second generation of the vacuum drying rig was constructed, the commissioning tests undertaken showed that the rig was still able to achieve the same ultimate vacuum pressure as prior to the upgrades. The decision to suspend the sample from the lid of the vessel resulted in the re-introduction of one regime identified by *J. Goode* as, once again the air trapped in the sample would expand as the pressure was reduced potentially forcing some of the water to flow through the defect as a liquid. Depending on the mass of water added it is also possible that the slug flow regime could be reintroduced as a consideration when suspending the sample as shown in Figure 114.

The final aspect of the work conducted with the vacuum drying rig is the tests undertaken using the corroded discs. In these tests it was possible to measure the internal pressure of the sample. It was expected that, when the water was removed this would, rather than as seen previously where a spike was seen in the pressure, result in a drop off in the pressure which would then increase as more vapour was produced. This did not occur. However, spikes in the dew point and flow were observed which indicate the removal of water from the system. The main concern with the corroded discs was the apparent drying of the sample. In previous tests, a lack of flow, a steady flat line dew point and a low but stable pressure was used as an indication that the sample had dried

out. With the system now measuring the internal sample pressure, one of the indications was no longer available. However, the flow was still being graphed live. In multiple tests, the flow dropped to 0 % and no spikes were observed indicating flow. Upon examination of the sample there was still water present. It is theorised that the cracks had become blocked creating the impression of the sample drying. Ice was originally suspected as the likely cause of a blockage however with the sample at 70 °C - 100 °C this was deemed unlikely. One other option considered was that the drying process had dislodged some corrosion product. This is unlikely to explain the initial pressure drop seen on the second test which was conducted immediately after the first.

This false end point is a key finding from this work as it shows how the measurements that would be available to an operator on a vacuum drying plant could assume that a container was suitable dried when a significant volume of water was still present in the system.

8 Modelling of the Vacuum Drying Process

This chapter will focus on the development and testing of the computational model produced in to assess the vacuum drying procedure. A focus is given on modelling the flow of fluid – in this case gas – through the defect. The three key models considered are presented here. Following this, the approach taken to the coding and the methodology applied to the code is discussed. Finally, the chapter will discuss the comparison of the model with data gathered from experimental runs with the pinhole discs and the corroded sample discs.

8.1 Theory

The three models which were deemed to be worthy of continued investigation are presented here. The first, by *Bomelburg*, is an orifice flow equation with a large pressure difference between the internal and external volumes (124). The second two, by *Beck et al.* and *Taggart and Budden*, are both leak-before-break models which take into account factors such as the surface roughness and tortuosity of the flow pathway.

8.1.1 Bomelburg Fluid Flow

The model set out by *Bomelburg* assumes that a closed container is filled with a perfect ga and a smooth cylindrical hole is present in the container wall (124). For the adiabatic scenario considered, the mass flow rate is given by:

$$Q_m = \alpha \cdot A \cdot \left(\frac{P_o}{P_s}\right)^{1/\gamma} \cdot \sqrt{\frac{\gamma}{\gamma - 1} \cdot \left[1 - \left(\frac{P_o}{P_s}\right)^{1/\gamma}\right]} \cdot \sqrt{2 \cdot g \cdot P_s \cdot \rho_s} \qquad \textit{Eq. 31}$$

Where, γ is the ratio of the specific heat capacities ${c_p}/{c_v}$.This can then be simplified to obtain an equation for the mass flow rate of:

$$Q_m = \alpha \cdot A \cdot \chi_{max} \cdot \sqrt{2 \cdot g \cdot P_s \cdot \rho_s} \qquad \textit{Eq. 32}$$

and X_{max} is given by:

$$\chi_{max} = \left(\frac{2}{\gamma + 1}\right)^{1/(\gamma - 1)} \cdot \sqrt{\frac{\gamma}{\gamma + 1}} \qquad \textit{Eq. 33}$$

The work presented by *Bomelburg*, considers a defect of 100 µm diameter which is representative of the pinhole discs used in the initial testing however the corrosion defects produced are much narrower. In addition the model does not take into account the tortuosity or the surface roughness of the defect. This will result in an overestimation of the flow rate as these factors would act to slow down the passage of gas through a leak path.

8.1.2 Taggart & Budden Fluid Flow Model

In order to assess defects in materials, the R6 procedure has been developed continuously since 1976 (159). A portion of this procedure deals with the determination of a leak rate arising from a single-phase, isothermal compressible flow through a crack (136). The standard program used by the nuclear industry within the R6 framework – DAFTCAT – assumes a rectangular crack cross-section. This model uses the following equation,

$$Q_m = C_D \cdot (P \cdot \rho)^{1/2} \cdot \overline{w} \cdot L \qquad \textit{Eq. 34}$$

with C_D, the discharge coefficient, related to the sum of the pressure losses experienced by the fluid as it passes through the crack; frictional – Eq. 35, inertial - Eq. 36 and arising from recirculation - Eq. 37. Figure 123 shows a simplified example of a crack along with the key parameters.

$$F_{fric} = \frac{f \cdot l_{eff}}{2 \cdot w_{eff}} \qquad \textit{Eq. 35}$$

$$F_{inert} = \frac{w_{eff}}{w} \cdot N \cdot 2 \cdot \theta \qquad \textit{Eq. 36}$$

$$F_{recirc} = N \cdot \left(1 - \left(\frac{w_{eff}}{w}\right)^2\right) \qquad \textit{Eq. 37}$$

and C_D being defined as:

$$C_D = \frac{1}{1 + \sqrt{F_{fric} + F_{inert} + F_{recirc}}} \qquad \textit{Eq. 38}$$

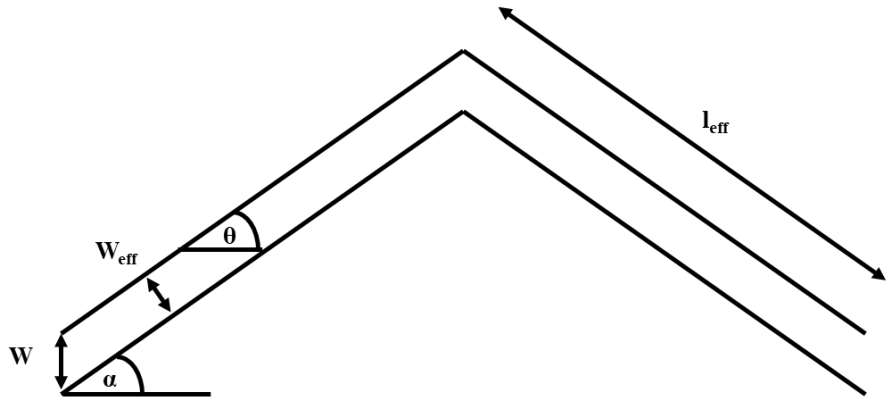

Figure 123: Simplified diagram showing the parameters for the model presented by Taggart and Budden. Simplified to show the variables used in the work. Original graphic from (136).

In order to calculate the number of turns, N, in a simplified crack network it is a relatively simple task as shown in Figure 124. However, once a real defect pathway is considered this would become very difficult to determine. Therefore, in the work presented here, the number of turns was treated as a fitting factor that could be adjusted.

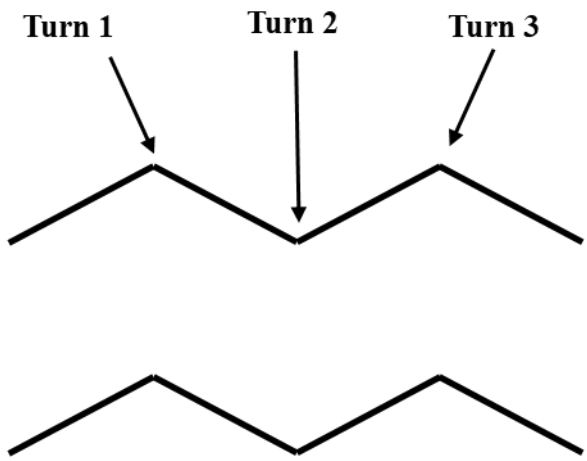

Figure 124: An schematic of a crack showing how the number of turns is determined.

The friction factor, f, is defined in the form:

$$f = \left[a_1 \cdot \log_{10}\left(\frac{a_2 \cdot COD}{R_a}\right) + a_3\right]^{-2} \qquad \textit{Eq. 39}$$

It is acknowledged by *Taggart and Budden* that different sources use a different value for the three constants when calculating the friction factor and these have been summarised in Table 18 with no preference stated in the article though it is noted that the constants as defined by Spence et al., gave better results than those defined by *Button et al*.

Table 18: Friction factor coefficients. Information contained in this table was sourced from (136)

Source	a_1	a_2	a_3
Spence et al	1.82	1	-0.77
Spence et al (modified)	2.035	1	-0.657
Gardiner & Tyrell	3.64	2	-2.636
Button et al	2.25	1	-0.573

Taggart and Budden have shown that there is good agreement between the R6 leak rate equation set out in the paper and the leak rates measured to provide validation.

8.1.3 Beck Fluid Flow Model

The approach set out by *Beck et al.* is built off the leak-before break procedure (135). In this approach, the volumetric flow rate, Q_v is given by:

$$Q_v = v \cdot w_{eff} \qquad \textit{Eq. 40}$$

as with the model set out by *Taggart and Budden*, the model by *Beck et al.* considers the dissipation of pressure across the crack arising from three sources; the fluid viscosity - Eq. 41, the inertia force - Eq. 42, and by expansion of the fluid in regions of lower pressure - Eq. 43. These parameters for this model are set out in Figure 125.

$$\Delta P_{visc} = \frac{12 \cdot \mu \cdot \ell_{eff} \cdot \bar{u}}{{D_{eff}}^2} \qquad \textit{Eq. 41}$$

$$\Delta P_{inertial} \cdot D = N \cdot D_{eff} \cdot \frac{\rho \cdot \bar{u}^2}{2} \cdot 2 \cdot \Gamma \qquad \textit{Eq. 42}$$

$$\Delta P_{exp} = N \cdot \frac{\rho \cdot \bar{u}^2}{2} \cdot \left(1 - \left(\frac{D_{eff}}{D}\right)^2\right) \qquad \textit{Eq. 43}$$

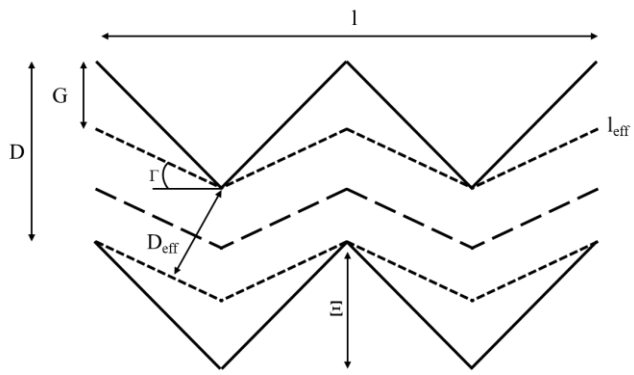

Figure 125: A schematic of an idealised section of crack showing the parameters. Adapted from (135).

Unlike the other approaches considered, the approach set out by *Beck et al.*, considers the impact of the surface roughness of the crack and the impact this has on the flow pathway noting that as the crack widens out the fluid will take a straighter path through the crack with l_{eff} eventually being equal to l. The width of the flow pathway, D_{eff}, also impacts which of the pressure loss terms (Eq. 41 to Eq. 43) dominates the flow characteristics.

For the narrowest cracks considered, between $1x10^{-5}$ and $3x10^{-5}$ m wide, the velocity of the fluid is given by:

$$0 = \frac{2 \cdot v}{\rho} \cdot \left[\frac{12 \cdot \mu \cdot l_{eff}}{w_{eff}^2}\right] - \Delta P \qquad \textit{Eq. 44}$$

In this regime, the flow is primarily influenced by the viscosity of the fluid. As the crack diameter increases to between $3x10^{-5}$ and $6x10^{-5}$ m, it becomes less tortuous and as a result the inertia pressure becomes important, with the velocity given by:

$$0 = \frac{\rho \cdot v^2}{2} \cdot \left[N \cdot 2 \cdot \theta \cdot \frac{w_{eff}}{d}\right] + \frac{2 \cdot v}{\rho} \cdot \left[\frac{12 \cdot \mu \cdot l_{eff}}{w_{eff}^2}\right] - \Delta P \qquad \textit{Eq. 45}$$

As the defect diameter is increased further to the region of $6x10^{-5}$ to 10^{-5} m the inertia forces are now considered to be minor, and the expansions and contractions of the fluid need to be accounted for resulting in the equation:

$$0 = \frac{\rho \cdot v^2}{2} \cdot \left[N\left(1 - \left(\frac{w_{eff}}{w}\right)^2\right)\right] + \frac{2 \cdot v}{\rho} \cdot \left[\frac{12 \cdot \mu \cdot l_{eff}}{w_{eff}^2}\right] - \Delta P \qquad \textit{Eq. 46}$$

Finally, for a crack opening area above $9x10^{-5}$ m, the flow becomes turbulent with the pressure losses experienced by the fluid almost entirely arises from the expansions and contractions giving a simplified equation for the velocity of

$$0 = \frac{\rho \cdot v^2}{2} \cdot \left[N\left(1 - \left(\frac{w_{eff}}{w}\right)^2\right)\right] - \Delta P \qquad \textit{Eq. 47}$$

This model was shown by *Beck et al.*to be capable of providing a good estimation, albeit an underestimation of the crack flow through a crack assuming that the surfaces are parallel and smooth. Although this is not the case with the cracks produced in this

work, modelling the nature of these cracks would be very difficult so assuming an idealised crack is a valid assumption to make.

8.2 Computational Work

8.2.1 Fluid Flow Modelling

In order to model the evacuation of the sample, the initial pressure inside the sample is required, this was assumed to be 1 BarA for the purposes of this investigation due to the sample being sealed at room pressure. From this initial pressure, the mass of air inside the sample is calculated. This is then used, along with the pressure difference between the internal and external volumes to calculate a mass flow rate over a one second period. For the purposes of this work the external volume is assumed to be infinitely large and therefore the fluid being evacuated from the sample does not cause a rise in the external pressure. With the mass flow calculated a new pressure inside the sample can be determined. This process is repeated using a loop for a user determined number of iterations with each iteration covering one second of flow.

It was desired that the evacuation of the vessel would be modelled in a similar fashion. The starting pressure of the vessel is known – again 1 BarA – and the equation for the pressure of a container after time, t is given by (160) :

$$P_2 = \frac{P_1}{e^{V/tq}} \qquad \textit{Eq. 48}$$

and q is the volume flow capacity of the vacuum pump.

8.2.2 Incorporation of Evaporation

The final aspect of the model would have been to incorporate the evaporation of water into the code using a similar method. The one second time step would have been used to calculate the mass of water evaporated and that used to calculate a mass of water vapour present in the sample. Initially the water vapour would have been assumed to be air for testing purposes with the plan then being to treat the two fluids, air and water vapour, independently and devise a means of determining the mass of each removed for each iteration of the code.

8.3 Results

8.3.1 Comparing Flow Models

In order to assess the three approaches, the results were plotted alongside the experimental data gathered from the pinhole flow rig. Figure 126 shows the comparison in a Pressure vs Time graph. Of not here is the Bomelburg model which does not follow the profile of the pressure. As a result, this was therefore discounted from further consideration. However, the models presented by *Beck et al.* and *Taggart & Budden* in addition to the average of the two approaches are close matches to the experimental data (135; 136).

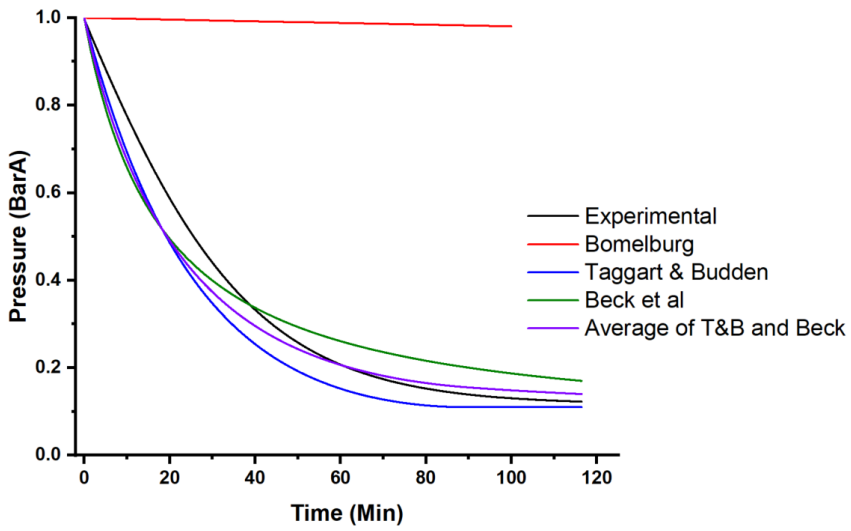

Figure 126: Comparison of the three main models with the experimental data gathered. In addition the average of the models proposed by Beck et al. and Taggart & Budden models is presented.

A second graph, Figure 127, has been plotted and shows the models plotted against the data gathered from experiments. Therefore, if a model was a perfect match to the experimental results, the line Y = X would be followed. Neither model or the average of the two showed a perfect match or indeed gave indication of a preference between the two. At low pressure, the traces in Figure 127 show that the model from *Beck et al.* provides a closer match to the Y = X line while at the higher pressures the model from *Taggart & Budden* is a closer approximation.

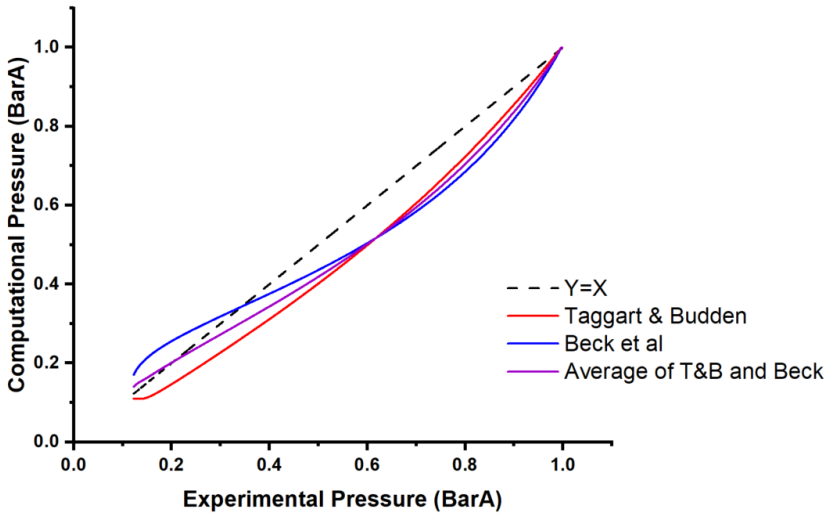

Figure 127: A plot of the computationally determined pressure against the experimentally determined pressure for the two different models and the average of both models.

8.3.2 Comparison to Initial Evacuation of the Vessel

The first comparison used to assess the model was to compare the computational results from atmosphere down to the pressure achieved during the initial pump down of the vessel. This was undertaken for two temperatures on a 50µm pinhole, 40°C , shown in Figure 128, and 50°C, as can be seen in Figure 129. The starting pressure was set to 1 BarA and the final pressure was set to the lowest pressure achieved during the pump down, 0.04 BarA.

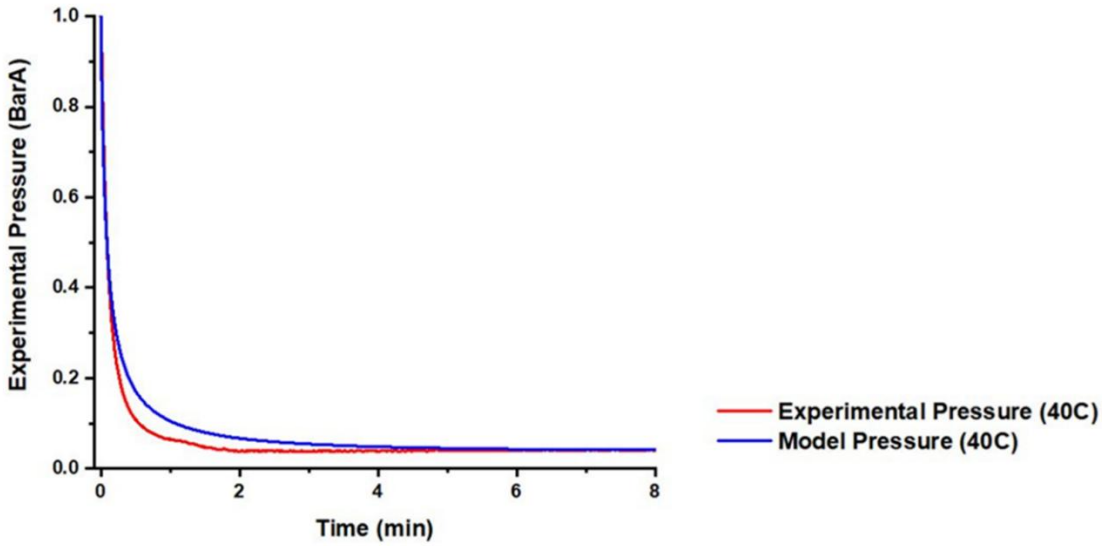

Figure 128: Comparison between the average Taggart & Budden model and the Beck et al model, compared pressure recorded during the initial pump down at 40°C.

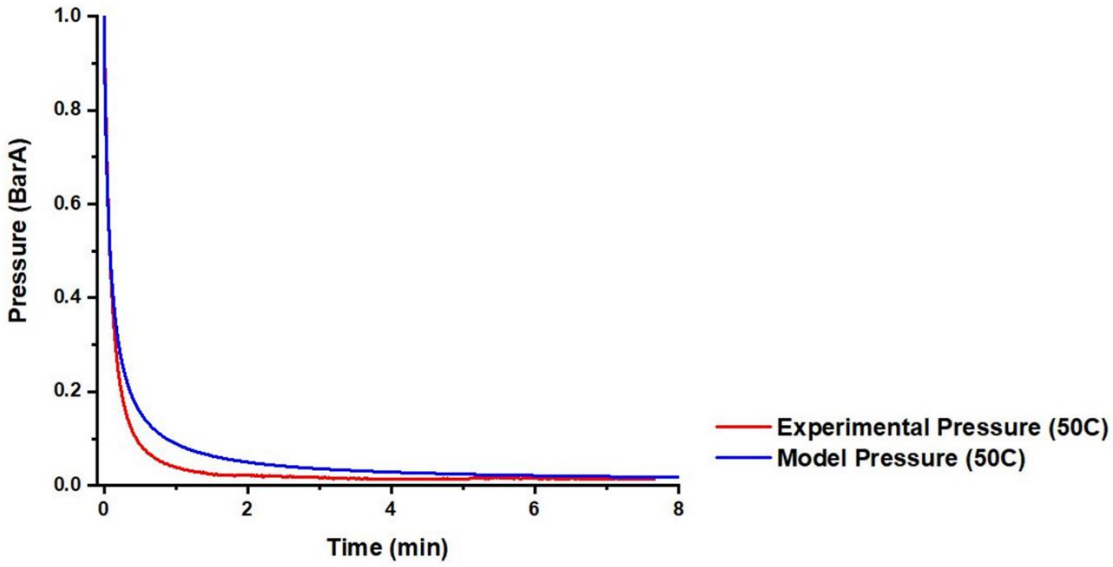

Figure 129: Comparison between the average Taggart & Budden model and the Beck et al model, compared pressure recorded during the initial pump down at 50°C.

These comparisons show a good level of agreement between the model devised and the initial pump down portion of the vacuum drying trials, which is as expected based on the results seen when comparing the model to the data gathered from the pinhole flow rig. In both cases however, the curve was shallower than expected however this was deemed to be a suitable match when taking into account the factors such as water level and evaporation which are not considered by the model.

8.3.3 Comparison to Peaks in the Vacuum Drying Process

In order to provide further validation, the *Beck* and *Taggart & Budden* models along with the average of the two, were plotted against data taken from experimental tests undertaken using the drying rig. This analysis was carried out using the results gathered from testing of pinhole discs as well as Disc 2 and Disc 3 (Figure 61 and Figure 65, Figure 66, Figure 67, Figure 68, Figure 69 and Figure 70).

To conduct these comparisons, the experimental data was examined to determine the final pressure of the system in the manner shown in Figure 130. Here, P_1 and P_2 are the initial pressure and final pressure while t_1 and t_2 define the time frame. Here $t_1 = 0$ seconds and t_2 is the elapsed time and therefore the number of iterations the code will run for.

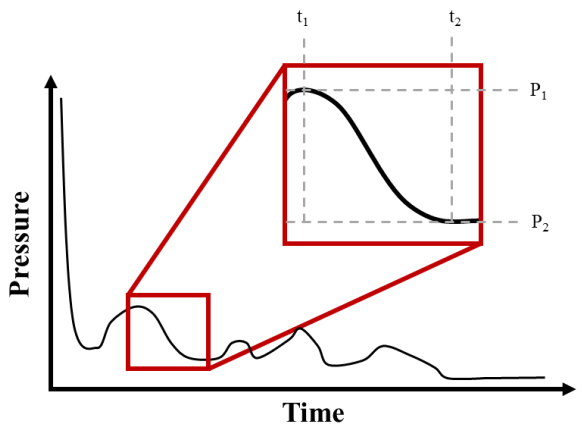

Figure 130: A representation of an evacuation trace and how the conditions and sections of graph were chosen for analysis in this section.

In comparison to the pinhole discs - Figure 131 and Figure 132 – the variable nature of the two main models is seen however in neither Figure is there an exact match to the experimental result. In Figure 131, the model by *Beck et al.* is the closest match however both models predicted a liner decrease in the pressure while a slight curve is seen in the data. This is again seen when comparing to a the reduction in pressure as shown in Figure 132 with the two models showing a linear decrease in the pressure while the data follows a curved path.

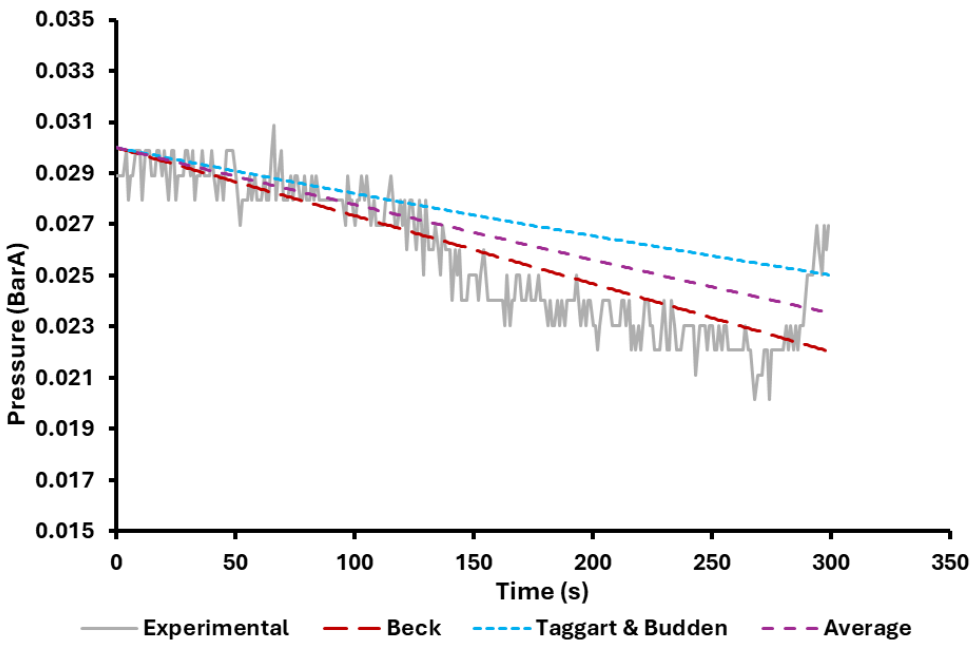

Figure 131: Comparison between the Beck, Taggart & Budden and the average approaches along with the evacuation from a peak in the pressure during a test of a 10 micron pinhole at 60°C.

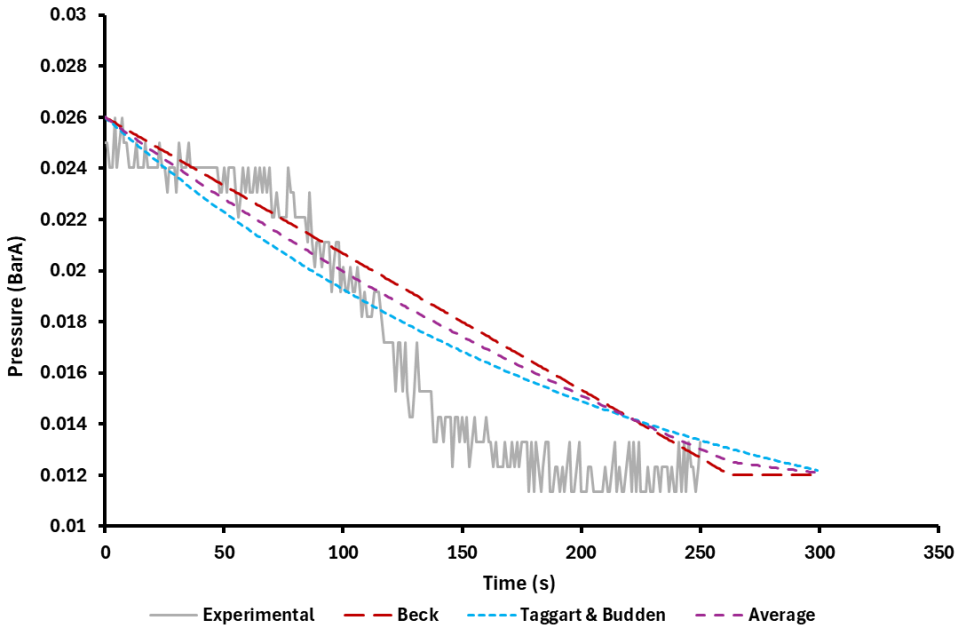

Figure 132: Comparison between the Beck, Taggart & Budden and the average approaches along with the evacuation from a peak in the pressure during a test of a 20 micron pinhole at 60°C.

Comparisons to the data gathered from the corroded discs was more successful as seen in Figure 133 and Figure 134. The first of these, Figure 133, shows good agreement between the model by *Beck et al*. and the experimental data, while Figure 134 shows the experimental data matching well to the average of the two models.

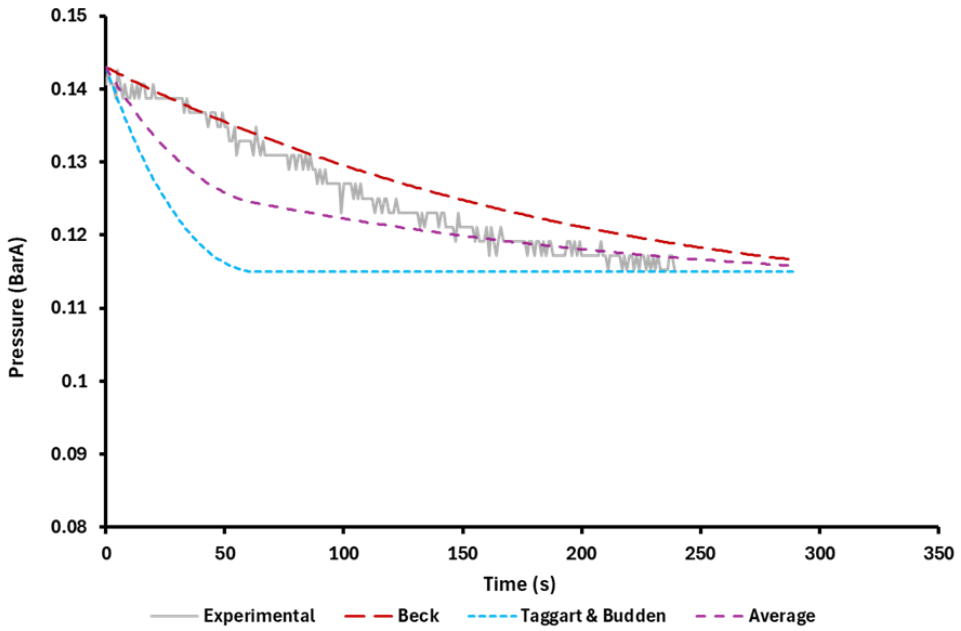

Figure 133: Comparison between the Beck, Taggart & Budden and the average approaches along with the evacuation from a peak in the pressure during a test of disc 2 at 120°C.

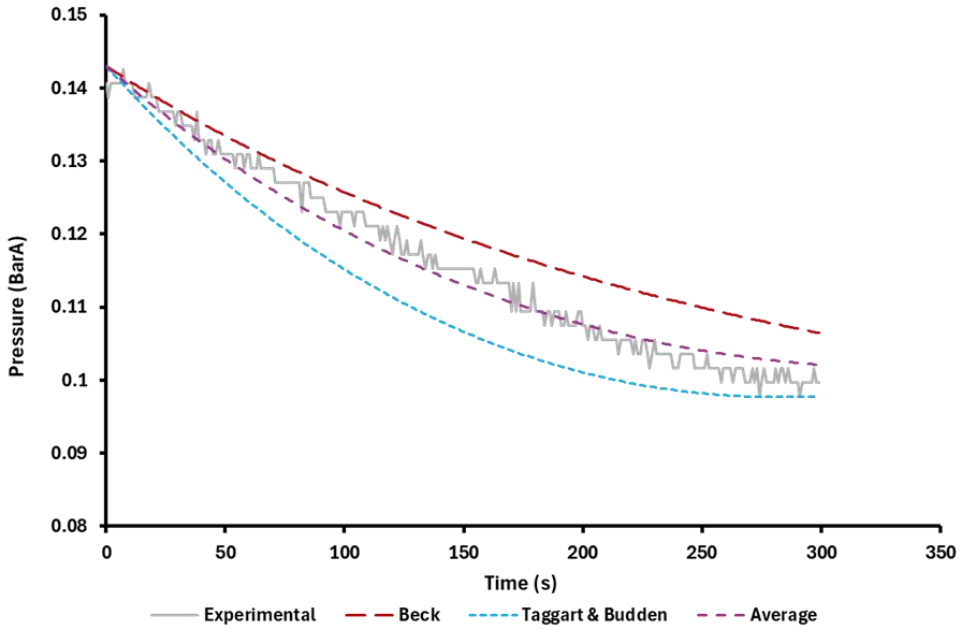

Figure 134: Comparison between the Beck, Taggart & Budden and the average approaches along with the evacuation from a peak in the pressure during a test of disc 3 at 120°C.

It is worth mentioning that due to the complex interaction between the different variable present in the system that no perfect match was expected and any model produced will inevitably have to make assumptions and lack the fidelity to predict individual spikes at the right time. However, with the limitations of the model used to produce the traces in Figure 131, Figure 132, Figure 133 and Figure 134 the average approach looks like a promising approach however, with refinement one of the models may prove to be more suited.

8.4 Summary

When the three flow models were compared to each other, shown in Figure 126, the approach set out by *Bomelburg*, was seen to be unsuited for modelling the flow in the pressure ranges used in this work as it vastly underestimated the flow rate and was therefore discounted from further consideration. The models by *Beck et al* and *Taggart & Budden* showed reasonable agreement. Both the models overestimated the flow rate to a similar degree in the pressure range 1 – 0.5 BarA, at which point a divergence is observed. The approach by *Taggart and Budden* continues to overestimate the flow rate leading to the final pressure being achieved sooner than the experiment while the model set out by *Beck et al*, switches to an underestimation and remained elevated compared to the experimental data.

By plotting the experimental data against the computational data a clearer picture of the difference between the two models is presented however, both provide reasonable accuracy. When the approaches are used to model the flow through the pinhole disc, the consideration given to the tortuosity and the surface roughness becomes clear with this resulting in the models underpredicting the flow rate. However, when the flow through the cracks is modelled, there is much better agreement between the models and the data.

9 Conclusions

The primary aim of this work was to develop the understanding of the behaviour of failed spent AGR fuel during the vacuum drying process. This chapter assess the different aspects of the work conducted and reported on throughout this report.

9.1 Experimental Work

9.1.1 Production of Defects

From the tests undertaken as part of this work it has been shown that the DET method is capable of producing corrosion damage in 316 and 304 stainless steel though the method needs to be refined to be reliable, primarily with the concerns around the heaters corroding. While the defects produced were not the very narrow, intergranular stress corrosion cracks we would expect to find in AGR cladding which has failed due to IGSCC, they are similar to that presented by *Kyffin et al*, which is noted to be 50 µm wide – shown in Figure 5. However this degradation is far beyond what is expected in any AGR fuel cladding since the introduction of the caustic dosing regime.

<u>Automated Drop Evaporation Technique:</u>

The first batch of experiments utilizing the drop evaporation rig used NaCl, following the approach used in the literature. This lead to minimal levels of corrosion being observed on the surface of the samples. With promising results, samples of stainless steel were sensitized and exposed to the NaCl solution which led to increased corrosion observed. Swapping to the more aggressive $MgCl_2$ resulted in pits reaching a substantial depth into the samples. However, issues with the approach became apparent. The specifics of the technique used in this work, when compared to the variations used in literature varied, primarily concerning the means by which the sample is heated. In this work external cartridge heaters were used which left them exposed to the corrosive solution. It is hypothesized that this caused several of the problems encountered owing to the corrosion of the heaters and associated wiring. A further reason for using an alternative heating method is to prevent the formation of any unintended products as seen upon switching to $MgCl_2$. However, with the evidence gathered during this work, it is expected that further refinement of the approach, the production of highly tortuous stress corrosion cracks would be possible.

Constantly Wetted Technique:

With the corrosion of the rig and heaters causing ongoing issues both for the operation of the rig and continuous electrical issues plaguing the rig an alternative approach was sought. This culminated in the decision to manually stress the samples and use tape to maintain the deflection. A few samples were tested using the rig to apply and maintain the stress. While a target temperature of 120°C was used for the initial experiments undertaken with the rig, these tests were undertaken at a reduced temperature of 70°C, limited by the drying oven at our disposal. With the results from the rig tests showing that the increased chloride content from the $MgCl_2$ having a marked effect on increasing the rate at which corrosion occurred it was decided that all tests done using this approach would be conducted with $MgCl_2$ as the corrosive media. The reduced temperature also allowed for a slight alteration to the drop evaporation technique, instead of waiting for the solution to fully evaporate prior to the next droplet arriving, we were able to manually add solution as required and in targeted areas. This resulted in a higher chloride concentration being achieved than would have been possible with the automated rig approach. As a result, we found increased number of pits present in the samples and said pits were analysed under optical and confocal microscopes to obtain dimensions and a topographical map which provided the depths of the pits. This method proved to be successful at corroding pits in sensitised 316 stainless steel and it is expected that, if a longer test was conducted these pits could eventually propagate through the full thickness of the sample. However, it is worth commenting on the drawbacks of this approach. The most prominent being the manual application of the solution which proved to be extremely time consuming. This is however, a relatively straightforward problem to solve with the addition of a pump to deliver the solution which was not viable in this scenario due to the number of samples being tested at a time. The second drawback is that to assess the corrosion extent present in the samples the test had to be temporarily halted, the deflection removed and the samples cleaned to remove any salt. It was observed that, post examination, it was rare to see a noticeable change in a previously observed corrosion feature. It is theorised that during the cleaning and examination of the sample the exposed metal had re-passivated preventing further corrosion from occurring in that location. Assessing the sample without cleaning was trailed however, this was not considered to be a valid technique as salt was found to remain trapped in the pits and therefore impede examination.

9.1.2 Vacuum Drying Process

The vacuum drying process has been shown in literature to be a viable means of removing a quantity of water from a container with a through-wall defect present. This work adds to that literature with the process proving to be viable across a range of defect sizes, as shown by the testing conducted with the pinhole discs. However, the upgrade to the rig set-up exposed several issues which would need to be addressed prior to an upscale to a pilot scale experiment or operational facility.

The first of these is the issue of the temperature and heating the sample or fuel pin. In the first generation rig set-up, used initially, the samples were in contact with the heated vessel allowing for a rapid temperature rise. However, the heating of the sample via conduction became severely limited once the sample was suspended from the lid of the vessel. While this eliminated the impact of the sample orientation and the possibility of the sample moving while in the vessel to bring more into contact with the wall it introduced a new concern. The reduced sample heating rate resulted in the elongation of the down time between adding the sample and the start of the test which, at higher temperatures, likely resulted in more of the water present int eh sample evaporating and therefore being removed at a faster rate.

Of greater concern to any future plans to use vacuum drying is the behaviour observed during testing with the corroded discs. The CT scan of the discs showed that a defect pathway was present and this was confirmed by the testing on the fluid flow rig where a flow was detected and the evacuated chamber returned to atmospheric pressure.

When these discs were tested in the vacuum drying rig, while initial indications were promising upon weighing the samples after the tests were performed showed very little drying had taken place. Looking a the data gathered during these experimental runs all the indications suggest that the sample had fully dried, the flow had been elevated after the initial spike as the vessel is evacuated, before falling to 0 % which would indicate that the sample is dry. Additionally the dew point dropped off, which as seen in tests conducted using the pinholes is usually a sign the sample has dried. The only metric available which shows the sample had not dried was the internal pressure reading and this would not be accessible in a process scale drying facility and therefore it could be falsely assumed that the fuel had been adequately dried.

9.1.3 Analysis of Defects

In analysing the defects and corrosion damage the stereomicroscope proved to be very useful in providing a quick means to assess a large area of the sample for corrosion. The external, posable lights allowed for manipulation of shadows to highlight the surface features. The CLSM was vital in determining the extent of the pits being produced with the topographic scan functionality. It was determined however, that the process of analysing the samples was causing passivation of the stainless steel in the pits and preventing further corrosion. The CT scans also proved useful to an extent. Higher resolution scans would have been ideal but this was not possible using the CT machine available at the time without cutting away more of the disc and thereby rendering it ineffective for the vacuum drying rig.

9.2 Computational Work

9.2.1 Determination of Defect Dimensions

While initially an automated process was desired, it was deemed to be unviable to automate the entire process due to the measurement methodology. During the testing on the straight channels, the approach was able to determine the length and the width with a variation of under 6%. While this variation did increase as more complex defects were analysed, there was still a suitably low variation to be confident in utilising the process to analyse the defects produced in this work. In testing with the defects produced via the adapted drop evaporation technique, it was determined that the resolution of the CT images obtained was insufficient to be able to use the current approach. This is primarily due to the CT machine used and the need to image a large area to avoid needing to section the defect discs and thereby rendering them unsuitable for testing in either the pinhole flow rig or the vacuum drying rig. This could be rectified upon the production of more defects by laser cutting to retain only the defect locations and minimal surrounding material.

9.2.2 Modelling Fluid Flow

Comparing the three models considered for this work; *Bomelburg*, *Taggart & Budden* and *Beck et al*, showed the limitation of the orifice plate model proposed by *Bomelburg* and hence this approach was discounted. Analysis showed that the two leak-before-break models were more successful in modelling the flow. When comparing the models to the results gathered from the pinhole flow rig we see that there is better agreement at alternate ends of the pressure range for the two models. With this in mind, it was

decided that an average of the two be taken. This produced a better overall match to the experimental data gathered from the pinhole flow rig.

Moving to comparing the models to the pressure peaks observed during the vacuum drying procedure, we see once again that the average of the two approaches usually produces a better result. However, it is also clear that there are significant variables that need to be refined and understood in order to produce a model. Chief among these is the evaporation of water at low pressure as any evaporation occurring will impact the rate at which the system returns to vacuum pressure. Secondly, factors such as the number of turns and the roughness of the defect need to be investigated as the values of these have a significant impact on the results.

9.3 Key Findings

The primary result from this work that in the tests using a corroded sample, albeit one which is potentially less tortuous and wider than those which may be found in AGR cladding, there is the potential for false positive readings to be achieved. If the hypothesis is correct that the defect channel became blocked, then it is unlikely that a vacuum rebound test would detect this as the moisture laded fluid would be trapped in the sample and therefore not picked up on the vessel pressure reading. In small scale tests this can be detected using an in-situ balance however, in pilot or commercial operation the natural variation in masses along with any additional mass from carbon depositions could cause this to be missed. Indeed, if the cracks found in the AGR cladding are more tortuous and narrower then this problem could be exacerbated further. Therefore, while vacuum drying has been shown to be effective for large diameter defects, there is a risk that when attempting to dry real spent fuel the morphology of the cracks will result in the need for the spent fuel to be under vacuum conditions for a very long time and a means of determining the dryness of the fuel is required which is still viable in the situation where a pin has become flooded but the defect has become obstructed either preventing drying from occurring or slowing it significantly.

Outside of the implications this has on any drying operations, the work done to produce corrosion cracks in samples is worthy of note. Despite the increased corrosion resistance of 316 stainless steel, the constantly wetted technique was able to produce corrosion damage at low temperatures. It is expected that with further testing a through thickness pit or crack would have developed.

In addition to the above, while the method may not have produced cracks which are representative of SCC, when compared to the images of cracks produced by PCMI and clad restructuring in the paper by *Barker et al.* the morphology and widths are comparable (38).

Finally, considering the computational aspects of this work. While the models used were able to provide reasonable agreement to the experimental data in a few circumstances it is clear that more work needs to be undertaken to refine the parameters used but other models should be considered which are more applicable to the pressure range and crack pathway dimensions expected. There is also a clear lack of literature focusing on the evaporation of water at low pressure with this playing a role in the discrepancy between the computational and experimental results.

10 Future Work

Finally, this Chapter will cover the recommendations and changes that should be made to improve the results gathered using the techniques and equipment which were used in the production of data for this report as well as the gaps which remain to be explored and future avenues of investigation.

10.1 Production of Defects

With the drop evaporation technique showing promise it would be worth pursuing this line of work further. It would be necessary to upgrade the rig in one of two paths. The first would be to place the entire rig into a heated environment, as was achieved by placing the samples into the drying cabinet, to ensure an even and constant elevated temperature. The second would be to persist with the brass heating blocks which showed evidence of being suitable with some refinement. This was shown by the corrosion and subsequent catastrophic failure of one of the samples. In order to improve this approach, it is suggested that larger brass blocks be used to cover the full length of the heaters. This would provide additional protection to the heaters and prevent the corrosive solution coming into contact with them. It is also recommended that the heaters be replaced with heaters which have a thermocouple built in to prevent the overheating seen in this work.

10.2 Simplified Fluid Flow Testing

It is recommended that a flow meter be installed in this rig, between the pressure transducer and the in order to properly assess the flow rate of air through the defect being tested. It would also be useful to adapt the set up to allow for the examination of the flow of water vapour though the system.

10.3 Vacuum Drying Process

Following the upgrade to the rig during the course of this work only minor upgrades to the rig are recommended with the primary one being the introduction of a real time means to measure the mass of the sample. This would reduce the time taken to complete tests and provide valuable insight. A means to introduce water to the sample while the sample is in situ would be another upgrade however this could be challenging to incorporate. By adding this ability however, the sample could be heated to the test temperature and then the test started without the loss of water during the heating time.

10.4 Analysis of Defects

Some refinement to the code is likely possible, primarily this should focus around the openings at either end of the defect where the skeleton produces triangular artefacts and are handled using Pythagoras which is not always suitable but provides a reasonable result. However, it is accepted that this may not be possible due to it being a feature of the skeletonization process. As discussed in section 5.3, the images of the defects, while suitable to confirm the defect pathway under visual examination of the images, the resolution was insufficient to allow for the defect to be detected by the image analysis code. In many places the defect pathway was only one or two pixels wide which is theorised to be the primary reason for this. To resolve this it is recommended that future defects be sectioned out from surrounding material to allow for a larger magnification to be used on the CT scanner. This would require all testing to be completed on the defects prior to the CT scan.

10.5 Fluid Flow Modelling

There is significant work to be done here in order to progress the model. The main influence missing from this work is the evaporation of water at low pressures. While multiple options were considered the evaporation equations primarily seemed to focus on larger bodies of water such as swimming pools and lakes and therefore were not of use in this situation.

Publications and Conference Presentations

Bainbridge, T. O., Hanson, B. C., Hondow, N. S., De La Fontaine, C. Drying of Spent AGR Fuel, In: TRANSCEND Theme Meeting 2020, December 2, 2020, Online.

Bainbridge, T. O., Hanson, B. C., Hondow, N. S., De La Fontaine, C. 2021. Drying of AGR Fuel. In : TRANSCEND Theme Meeting 2021, May 18, 2021, Online.

Bainbridge, T. O., Hanson, B. C. 2021. Drying of AGR Fuel through Stress Corrosion Cracks. In: MRS 2021 - 45th Scientific Basis for Nuclear Waste Management Online, October 25, 2021, Cologne, Germany. Online.

Bainbridge, T. O., Hanson, B. C., Hondow, N. S., De La Fontaine, C. 2021. Drying of AGR Fuel. In : TRANSCEND Annual Meeting 2021 – Harrogate, November 10-11, 2021, Harrogate, UK.

Bainbridge, T. O., Hanson, B. C., Hondow, N.S., De La Fontaine, C. 2022. AGR Fuel and its Behaviour During Drying – 22190 [Poster]. In: WM2022: Waste Management Symposia, March 6-10, 2022, Phoenix, AZ, USA. WM Symposia.

Bainbridge, T. O., Hanson, B. C., Hondow, N. S., De La Fontaine, C. Advanced Gas Reactor Fuel and its Behaviour During Drying, TRANSCEND Theme Meeting, May 24, 2022, University of Lancaster, UK

Bainbridge, T. O., Hanson, B. C., Hondow, N.S., De La Fontaine, C. 2022. Drying of Spent AGR Fuel. In: UNTF 2022: Universities Nuclear Technology Forum 2022, June 20-22, 2022, Bangor, UK.

Bainbridge, T. O., Hanson, B. C., Hondow, N.S., De La Fontaine, C. 2022. Drying of Spent Advanced Gas Reactor Fuel [Poster]. In: NuMat 2022: The Nuclear Materials Conference, October 24-28, Ghent, Belgium. NuMat 2022: The Nuclear Materials Conference

Bainbridge, T. O., Hanson, B. C., Hondow, N.S., De La Fontaine, C. 2022. Drying of Spent AGR Fuel for Storage and Disposal – EN08.10.07, In: MRS Fall Meeting 2022, November 28-30, 2022, Boston, MA, USA. MRS Fall Meeting 2022

Bainbridge, T. O., Hanson, B. C., Hondow, N. S., De La Fontaine, C. 2022. Vacuum Drying of Spent AGR Fuel. In : TRANSCEND Annual Meeting 2022 – Glasgow, November 1-2, 2022, Glasgow, UK.

Bainbridge, T. O., Hanson, B. C., Hondow, N.S., De La Fontaine, C. 2023. Vacuum Drying of AGR Fuel through Cracked Cladding – 23346. In: WM2023: Waste Management Symposia, February 26 – March 2, 2023, Phoenix, AZ, USA. WM Symposia. ISBN 978-0-9836186-6-9.

Bainbridge, T. O., Hanson, B. C., Hondow, N. S., De La Fontaine, C. 2023. Vacuum Drying of AGR Fuel Through Cracked Cladding. In : TRANSCEND Annual Meeting 2023 – London, April 24-25, 2023, London, UK.

Bainbridge, T. O., Hanson, B. C., Hondow, N.S., De La Fontaine, C. 2023. Drying of Spent AGR Fuel for Storage and Disposal. In: UNTF 2023: Universities Nuclear Technology Forum 2023, July 19-20, 2023, Bristol, UK.

References

1. **Lerner, L.** The First Nuclear Reactor, Explained. [Online] UChicago News. [Cited: 22 March 2025.] https://news.uchicago.edu/explainer/first-nuclear-reactor-explained.

2. **International Atomic Energy Authority.** Atoms for Peace Speech. [Online] [Cited: 22 March 2025.] https://www.iaea.org/about/history/atoms-for-peace-speech.

3. **Institution of Civil Engineers.** Calder Hall Nuclear Power Station. [Online] [Cited: 22 March 2025.] https://www.ice.org.uk/what-is-civil-engineering/infrastructure-projects/calder-hall-nuclear-power-station.

4. **Waste Stream 2S304: Windscale Piles Fuel and Isotopes. [Online] [Cited: 22 March 2025.] https://ukinventory.nda.gov.uk/wp-content/uploads/2019/11/2S304.pdf.**

5. ***Resolving the Technical Uncertainties in the Decommissioning of an Accident Damaged Reactor - Windscale Pile 1.*** **Cross, M. T., et al. Tucson, AZ : s.n., 2005. Waste Management Symposium .**

6. Explore Nuclear. Magnox Reactors. [Online] [Cited: 22 March 2025.] https://explorenuclear.com/magnox-reactors-at-the-forefront-of-a-new-age/.

7. —. Advanced Gas-cooled Reactor. [Online] [Cited: 22 March 2025.] https://explorenuclear.com/advanced-gas-cooled-reactors/.

8. Westinghouse. Advanced Gas-cooled Reactors. [Online] [Cited: 22 March 2025.] https://westinghousenuclear.com/uknuclear/products-services/advanced-gas-cooled-reactors/#:~:text=AGR%20fuel%20is%20a%20type,tubes%2C%20each%20containing%2064%20pellets..

9. ***Corrosion of AGR Fuel Pin Steel Under Conditions Relevant to Permanent Disposal.*** **Anwyl, C., et al. 2016, Procedia Chemistry, Vol. 21, pp. 247-254.**

10. Science Museum Group. AGR fuel pin cut away to show simulated fuel. 1982-1439. [Online] [Cited: 21 March 2025.] https://collection.sciencemuseumgroup.org.uk/objects/co5459/agr-fuel-pin-cut-away-to-show-simulated-fuel.

11. —. AGR Fuel Element, c 1982 1982-1575. [Online] Science Museum Group Collection Online. [Cited: 21 March 2025.] https://collection.sciencemuseumgroup.org.uk/objects/co5473/agr-fuel-element-c-1982.

12. New Era at Sellafield as THORP Reprocessing Ends. [Online] 14 November 2018. [Cited: 27 March 2025.] https://www.gov.uk/government/news/new-era-at-sellafield-as-thorp-reprocessing-ends#:~:text=The%20decision%20to%20cease%20reprocessing,rather%20than%20reprocess%20their%20fuel..

13. World Nuclear Association. Nuclear Fuel Cycle Overview. [Online] 21 March 2025. [Cited: 27 March 2025.] https://world-nuclear.org/information-library/nuclear-fuel-cycle/introduction/nuclear-fuel-cycle-overview.

14. Nuclear Waste Services. What is the Timescale for the GDF Programme? [Online] 27 January 2025. [Cited: 7 May 2025.] https://www.gov.uk/government/publications/finding-a-suitable-site-for-a-geological-disposal-facility/what-is-the-timescale-for-the-gdf-programme#:~:text=The%20current%20planning%20assumption%20is,run%20into%20the%20next%20century..

15. Kyffin, J. and Hillier, A. Technological Development to Support a Change in the Unjted Kingdom's Strategy for Management of Spent AGR Oxide Fuel. [Online] 19 June 2015. [Cited: 21 March 2025.] https://www-pub.iaea.org/iaeameetings/cn226p/Session7/ID37Kyffin.pdf.

16. International Atomic Energy Agency. *IAEA-TECDOC-1771: Spent Fuel Performance Assessment and Research.* Vienna : International Atomic Energy Agency, 2015.

17. Morgan, S., et al. *Post Irradiation Examination of UK Advanced Gas-cooled Reactor Fuel Cladding (post-reactor and post-storage).* 2015.

18. *Vacuum Drying of Advanced Gas Reactor Fuel.* J. B. Goode, D. Harbottle and Hanson, B. C. 2018, Progress in Nuclear Energy, Vol. 109, pp. 145-158.

19. *Technological Development to Support a Change in the United Kingdom's Strategy for Management of Spent AGR Oxide Fuel.* Kyffin, J. and Hillier, A.

Vienna : IAEA, 2015. International Conference on Management of Spent Fuel from Nuclear Power Reactors.

20. Nuclear Decommissioning Authority. *NDARB016: Review of NDA's Spent Fuels R&D Programme.* 2014.

21. —. *Strategy Effective from March 2021.* s.l. : Nuclear Decommissioning Authority, 2021.

22. *Effects of drying and grinding in production of fruit and vegetable powders: A review.* Karam, M. C., et al. 2016, Journal of Food Engineering, Vol. 188, pp. 32-49.

23. Busch Vacuum. Vacuum Drying. [Online] [Cited: 22 March 2025.] https://www.buschvacuum.com/uk/en/applications/drying/.

24. Miller, L., et al. *Overview of Vacuum Drying Methods and Factors Affecting the Quantity of Residual Water after Drying - Public Version.* s.l. : U.S. Nuclear Regulatory Commission, 2013.

25. Goode, J. *Transitioning of Spent Advanced Gas Reactor Fuel from Wet to Dry Storage.* s.l. : University of Leeds, 2017.

26. International Atomic Energy Agency. *Management of Damaged Spent Nuclear Fuel.* Vienna : International Atomic Energy Agency, 2009.

27. World Nuclear Association. Processing of Used Nuclear Fuel. [Online] World Nuclear Association, 23 August 2024. [Cited: 24 March 2025.] https://world-nuclear.org/information-library/nuclear-fuel-cycle/fuel-recycling/processing-of-used-nuclear-fuel.

28. United States Nuclear Regulatory Commission. Backgrounder on Dry Cask Storage of Spent Nuclear Fuel. [Online] 24 June 2023. [Cited: 24 March 2025.] https://www.nrc.gov/reading-rm/doc-collections/fact-sheets/dry-cask-storage.html.

29. *Effect of H2O2 on the Corrosion Behaviour of 304L Stainless Steel.* Song, T. H., Kim, I. S. and Rho, S. K. 4, 1995, Journal of the Korean Nuclear Society, Vol. 27.

30. World Nuclear Association. Nuclear Development in the United Kingdom. [Online] World Nuclear Association, 12 October 2016. [Cited: 03 March 2025.] https://world-nuclear.org/information-library/appendices/nuclear-development-in-the-united-kingdom.

31. ***The Advanced Gas-cooled Reactor: A Case Study in Reactor Choice.*** **Rush, H. J., MacKerron, G. and Surrey, J. 2, 1977, Energy Policy, Vol. 5, pp. 95-105.**

32. Power Technology. Sellafield WAGR. [Online] 10 February 2002. [Cited: 25 March 2025.] https://www.power-technology.com/projects/sellafield/?cf-view.

33. International Atomic Energy Agency (IAEA). General Design and Principles of the Advanced Gas-Cooled Reactor (AGR) . [Online] [Cited: 21 March 2025.] https://nucleus-qa.iaea.org/sites/graphiteknowledgebase/wiki/Guide_to_Graphite/General%20Design%20and%20Principles%20of%20the%20Advanced%20Gas-Cooled%20Reactor%20(AGR).aspx.

34. ***Advanced Gas-cooled Reactors Technology for Enabling Molten-Salt Reactors Design - Estimation of Coolant Impact on Neutronic Performance.*** **Margulis, M. and Shwageraus, E. 2020, Progress in Nuclear Energy, Vol. 125.**

35. EDF Energy. Dungeness B Power Station. [Online] [Cited: 28 March 2025.] https://www.edfenergy.com/energy/power-stations/dungeness-b.

36. —. Hunterston B Power Station. [Online] [Cited: 28 March 2025.] https://www.edfenergy.com/energy/power-stations/hunterston-b.

37. Nonbøl, E. ***Description of the Advanced Gas Cooled Type of Reactor.*** **Roskilde : Risø National Laboratory, 1996.**

38. ***Fuel Pin Failure Modes in the UK's Advanced Gas-cooled Reactors.*** **Barker, M. A., Mayhem, D. and O'Neil, R. 2024, Progress in Nuclear Energy, Vol. 175.**

39. World Nuclear Association. Nuclear Power Reactors. [Online] 21 March 2025. [Cited: 28 March 2025.] https://world-nuclear.org/information-library/nuclear-fuel-cycle/nuclear-power-reactors/nuclear-power-reactors.

40. ***Vacuum Drying of Advanced Gas Reactor Fuel.*** **Goode, J., Harbottle, D. and Hanson, B. C. 2018, Progress in Nucelar Energy, Vol. 109, pp. 145-158.**

41. World Nuclear Association. Nuclear Fuel and its Fabrication. [Online] [Cited: 28 Janruary 2024.] https://world-nuclear.org/information-library/nuclear-fuel-cycle/conversion-enrichment-and-fabrication/fuel-fabrication.aspx.

42. International Atomic Energy Agency. Other Designs of Nuclear Power Stations. [Online] [Cited: 26 March 2025.] https://nucleus.iaea.org/sites/graphiteknowledgebase/wiki/Guide_to_Graphite/Other%20Designs%20of%20Nuclear%20Power%20Stations.aspx.

43. Jensen, S. E. and Nonbøl, E. *Description of the Magnox Type of Gas Cooled Reactor (MAGNOX).* s.l. : NKS, 1998.

44. Thyssenkrupp. Stainless Steel 304 1.4301. [Online] [Cited: 25 March 2025.] https://www.thyssenkrupp-materials.co.uk/stainless-steel-304-14301.html.

45. —. Stainless Steel 316 1.4401. [Online] [Cited: 25 March 2025.] https://www.thyssenkrupp-materials.co.uk/stainless-steel-316-14401.html.

46. *Investigation of Thermally Sensitised Stainless Steels as Analogues for Spent AGR Fuel Cladding to Test a Corrosion Inhibitor for Intergranular Stress Corrosion Cracking.* Whillock, G. O. H., Hands, B. J. and T. P. Majchrowski, D. I. Hambley. 2017, Journal of Nuclear Materials, Vol. 498, pp. 187-198.

47. Howett, E. A. *The Behaviour of Spent Nuclear Fuel in Wet Interim Storage.* s.l. : University of Lancaster, 2019.

48. *The Long Term Storage of Advanced Gas-cooled Reactor (AGR) Fuel.* Standring, P. 1999.

49. United States Nuclear Regulatory Commission. Dry Cask Storage. [Online] 16 June 2023. [Cited: 13 April 2025.] https://www.nrc.gov/waste/spent-fuel-storage/dry-cask-storage.html.

50. World Nuclear Association. How Is Used Nuclear Fuel Managed. [Online] 06 August 2019. [Cited: 13 April 2025.] https://world-nuclear.org/our-association/publications/technical-positions/how-is-used-nuclear-fuel-managed.

51. *Licensing Approach and Progress for the Scottish Nuclear Dry Stores at Torness and Hunterston.* Biglin, C. J., et al. 1995, British Nuclear Energy Society.

52. EDF. Changing the Way We'll Store Used Fuel. [Online] 26 August 2022. [Cited: 13 April 2025.] https://www.edfenergy.com/energy/nuclear-new-build-projects/hinkley-point-c/news-views/changing-way-well-store-used-fuel-hinkley-point-c.

53. McCracken, K. J. *Hanford Spent Nuclear Fuel Cold Vacuum Drying Proof of Performance Test Procedure.* 1998.

54. *ASTM C1553-21: Standard Guide for Drying of Spent Nuclear Fuel.* s.l. : ASTM, 2021.

55. d'Entremont, A., et al. *Drying of Spent Nuclear Fuel: Considerations and Examples.* s.l. : Idaho National Laboratory, 2023.

56. *End Point Determination for Spent Fuel Nuclear Fuel Drying Operations.* Goode, J. B., Hambley, D. I. and Hanson, B. C. 2019, Progress in Nuclear Energy, Vol. 116.

57. *Comparison of Vacuum and Forced Helium Drying Methods for Dry Storage of Spent Nuclear Fuel.* Lee, J., et al. Jeju : s.n., 2017. Transactions of the Korean Nuclear Society Spring Meeting.

58. International Atomic Energy Agency. *IAEA-TECDOC-1771: Final Report of a Coordinated Research Project on Spent Fuel Performance Assessment and Research (SPAR-III) 2009-2014.* Vienna : IAEA, 2015.

59. *A Benchtop Comparison of Drying Methods Relevant to Failed Spent Nuclear Fuel.* Goode, J. B., Hambley, D. I. and Hanson, B. C. 2019, Progress in Nuclear Energy, Vol. 115.

60. *Design and Operation of Used Nuclear Fuel Drying System - 23421.* Fitzpatrick, J. and Bartley, J. Phoenix : WM2023, 2023.

61. Nuclear Decomissioning Authority. *2022 UK Radioactive Material Inventory.* s.l. : NDA, 2022.

62. SKB. The Spent Fuel Repository. [Online] 05 February 2021. [Cited: 05 May 2025.] https://skb.com/future-projects/the-spent-fuel-repository/.

63. Washington State Office of the Attorney General. Yucca Mountain Nuclear Waste Repository. [Online] [Cited: 05 May 2025.] https://www.atg.wa.gov/yucca-mountain-nuclear-waste-repository.

64. Posiva. [Online] [Cited: 05 May 2025.] https://www.posiva.fi/en/.

65. Gov.uk. [Online] Nuclear Waste Services, 31 January 2022. [Cited: 05 May 2025.] https://www.gov.uk/guidance/gdf-geological-disposal-facility.

66. World Nuclear Association . Storage and Disposal of Radioactive Waste. [Online] 30 April 2024. [Cited: 07 May 2025.] https://world-nuclear.org/information-library/nuclear-fuel-cycle/nuclear-waste/storage-and-disposal-of-radioactive-waste.

67. Nuclear Waste Services. GDF Progress as Areas of Focus Identified. [Online] 30 January 2025. [Cited: 30 May 2025.] https://www.gov.uk/government/news/gdf-progress-as-areas-of-focus-identified#:~:text=The%20areas%20are%20within%20the,Cumbria%2C%20and%20in%20East%20Lincolnshire..

68. Penn Stainless Products. 300 Series. [Online] [Cited: 14 April 2025.] https://www.pennstainless.com/resources/product-information/stainless-grades/300-series/.

69. Thyssenkrupp. Stainless Steel 904L 1.4539. [Online] [Cited: 14 April 2025.] https://www.thyssenkrupp-materials.co.uk/stainless-steel-904l-14539.html.

70. *Theory of Sensitisation of Stainless Steel and the Method of Diagnosis.* Umemura, F. 8, 1983, Haikan Gijutsu, Vol. 25, pp. 98-104.

71. *Sensitization and Self-healing in Austenitic Stainless Steel: Quantitative Prediction Considering Carbide Nucleation and Growth.* Kolli, S., et al. 11, 2019, ISIJ International, Vol. 59, pp. 2090-2097.

72. Austral Wright Metals. Application Data Sheet - Stainless Steel. [Online] [Cited: 05 May 2025.] https://www.australwright.com.au/technical-data/advice/stainless-steel/sensitisation-of-austenitic-stainless-steels/#:~:text=Austenitic%20stainless%20steels%20may%20become,range%20500%20%E2%80%93%20850%C2%B0C..

73. *The Effect of Sodium Hydroxide on Niobium Carbide Precipitates in Thermally Sensitised 20Cr-25Ni-Nb Austenitic Stainless Steel.* Clark, R. N., et al. 2020, Corrosion Science, Vol. 170.

74. Davis, J. R. *Corrosion Understanding the Basics.* s.l. : ASM International, 2000. ISBN: 0-87170-641-5.

75. AMPP. Uniform Corrosion. [Online] [Cited: 7 May 2025.] https://www.ampp.org/technical-research/impact/corrosion-basics/group-1/uniform-corrosion.

76. —. Forms of Corrosion. [Online] [Cited: 7 May 2025.] https://www.ampp.org/technical-research/what-is-corrosion/forms-of-corrosion.

77. Cathwell. Cathodic Protection Explained. [Online] [Cited: 7 May 2025.] https://cathwell.com/cathodic-protection-explained/#:~:text=Cathodic%20protection%20is%20one%20of,submerged%20or%20buried%20metal%20structures..

78. AMPP. Pitting Corrosion. [Online] [Cited: 7 May 2025.] https://www.ampp.org/technical-research/impact/corrosion-basics/group-1/pitting-corrosion#:~:text=Pitting%20corrosion%20is%20a%20localized,products%20often%20cover%20the%20pits..

79. ASTM International. G46-94: Standard Guide for Examination and Evaluation of Pitting Corrosion. 2005.

80. Part I: General Aspects of Corrosion, Corrosion Control, and Corrosion Prevention. *Corrosion Atlas Case Studies.* 2019.

81. Corrosion Clinic. Lecture 10: Crevice Corrosion and Pitting. [Online] [Cited: 7 May 2025.] https://www.corrosionclinic.com/corrosion_online_lectures/ME303L10.HTM.

82. AMPP. Galvanic Corrosion. [Online] [Cited: 10 May 2025.] https://www.ampp.org/technical-research/impact/corrosion-basics/group-1/galvanic-corrosion.

83. Corrosionpedia. An Introduction to the Galvanic Series: Galvanic Compatibility and Corrosion. [Online] 12 November 2020. [Cited: 10 May 2025.] https://www.corrosionpedia.com/an-introduction-to-the-galvanic-series-galvanic-compatibility-and-corrosion/2/1403.

84. Water Works. Bimetallic Corrosion: Understanding and Preventing a Common Threat to Metal Structures. [Online] [Cited: 27 March 2025.] https://blog.waterworksnz.co.nz/why-is-stainless-steel-corroding-0.

85. Corrosionpedia. Stress Corrosion Cracking. [Online] 19 July 2024. [Cited: 10 May 2025.] https://www.corrosionpedia.com/definition/1036/stress-corrosion-cracking-scc.

86. *Stress-Corrosion Cracking.* Sieradzki, K. and Newman, R. C. 11, 1987, Journal of Physics and Chemistry of Solids, Vol. 48, pp. 1101-1113.

87. Corrosionpedia. Caustic Cracking. [Online] 19 July 2024. [Cited: 10 May 2025.] https://www.corrosionpedia.com/definition/238/caustic-cracking.

88. The Hendrix Group Inc. Corrosion in Caustic Solutions. [Online] 5 April 1999. [Cited: 10 May 2025.] https://hghouston.com/archive/technical-newsletters/corrosion-in-caustic-solutions#:~:text=Low%20concentrations%20of%20caustic%20can,oF/48oC..

89. Jayasinghe, D. and Gopal, R. Intergranular Corrosion: What Is It and How to Stop It. [Online] Corrosionpedia, 19 July 2024. [Cited: 10 May 2025.] https://www.corrosionpedia.com/intergranular-corrosion-what-it-is-and-how-to-stop-it/2/7229.

90. British Stainless Steel Association. Intergranular Corrosion (IC). [Online] [Cited: 11 May 2025.] https://bssa.org.uk/technical-help/corrosion/intergranular-corrosion/.

91. *Susceptibility to the Intergranular Attack in Austenitic Stainless Steels.* Zatkalíková, V, et al. s.l. : IOP Publishing, 2020. IOP Conference Series: Materials Science and Engineering. Vol. 726.

92. Ford, F. P. and B. M. Gordon, R. M. Horn. 16 - Intergranular Stress Corrosion Cracking (IGSCC) in Boiling Water Reactors (BWRs). *Nuclear Corrosion Science and Engineering.* s.l. : Woodhead Publishing Series in Energy, 2012, pp. 548-580.

93. Stainless Steel Industry of North America. Intergranular Corrosion. [Online] SSINA. [Cited: 12 May 2025.] https://www.ssina.com/education/corrosion/intergranular-corrosion/.

94. *Assessment of Susceptibility to Chloride Stress Corrosion Cracking of Highly Alloyed Stainless Steels. Part II: a New Immersion Test Method.* Drugli, J. M. and Steinsmo, U. New Orleans : NACE, 1997. NACE Corrosion.

95. ***On the Mechanism of Intergranular Stress Corrosion Cracking of Sensitised Stainless Steel in Tetrathionate Solution.*** **Yonezu, A., Kusano, R. and Chen, X. November 2013, Journal of Materials Science, Vol. 48, pp. 2447-2453.**

96. Rahmi, S. ***Behaviour of Short Intergranular Stress Corrosion Crack in Type 304 Austenitic Stainless Steel.*** **s.l. : The University of Manchester, 2009.**

97. ***Effect of Surface Machining on Intergranular Stress Corrosion Cracking (IGSCC) in Sensitised Type 304 Austenitic Stainless Steel.*** **Rahimi, S., Mehrez, K. and Marrow, T. J. 5, 2016, Corrosion Engineering Science and Technology, Vol. 51, pp. 383-391.**

98. ***Can teh Drop Evaporation Test Evaluate the Stress Corrosion Cracking Susceptibility of the Welded Joints of Duplex and Super Duplex Stainless Steels?*** **Pereira, H. B. and Azevedo, C. R. F. 2019, Engineering Failure Analysis, Vol. 99, pp. 235-247.**

99. ***Investigation of Stress Corrosion Cracking of Austenitic, Duplex and Super Duplex Stainless Steels under Drop Evaporation Test using Synthetic Seawater.*** **Pereira, H. B., et al. 2, 2019, Materials Research, Vol. 22.**

100. ***Assessment of Susceptibility to Chloride Stress Corrosion Cracking of Highly Alloyed Stainless Steels. Part 1: Drop Evaporation Test Method.*** **Steinsmo, U. and Drugli, J. M. New Orleans : s.n., 1997. NACE Corrosion. pp. 1-15.**

101. British Standards Institution. BE EN ISO 15324:2008 Corrosion of Metals and Alloys - Evaluation of Stress Corrosion Cracking by the Drop Evaporation Test. 2008.

102. ***Threshold Temperature for Stress Corrosion Cracking of Duplex Stainless Steel Under Evaporative Sea Water Conditions.*** **Hinds, G. and Turnbull, A. 2, 2008, Corrosion, Vol. 64, pp. 101-106.**

103. ***The Chloride Stress Corrosion Cracking Behaviour of Stainless Steels Under Different Test Methods.*** **Jin, L. Z. 1994, Journal of Materials Engineering and Performance, Vol. 3, pp. 734-739.**

104. ***The Chloride Stress-Corrosion Cracking Behaviour of Stainless Steels Under Different Test Methods.*** **Jin, L. Z. 1994, Journal of Materials Engineering and Performance, pp. 734-739.**

105. ***Stress Corrosion Cracking of Austenitic Stainless Steels by the Drop Evaporation Test.*** **Lasek, S., Číhal, V. and Blahetová, M. Nice : s.n., 2004. EUROCORR 2004: Long Term Prediction and Modeling of Corrosion.**

106. ***Pitting Corrosion Mechanism of Type 304 stainless steel under a droplet of chloride solutions.*** **Tsutsumi, Y., Nishikata, A. and Tsuru, T. 3, 2007, Corrosion Science, Vol. 49, pp. 1394-1407.**

107. Edinburgh Instruments. Illumination Techniques in Optical Microscopy. [Online] 6 July 2023. [Cited: 26 March 2025.] https://www.edinst.com/resource/illumination-techniques-in-optical-microscopy/#:~:text=Brightfield%20microscopy%20is%20best%20for,such%20as%20edges%20and%20defects..

108. NanoScience Instruments. Scanning Electron Microscopy. [Online] [Cited: 12 May 2025.] https://www.nanoscience.com/techniques/scanning-electron-microscopy/.

109. nanoScience Instruments. Which Electron Detector is Right for Your Application. [Online] [Cited: 13 May 2025.] https://www.nanoscience.com/blogs/which-electron-detector-is-right-for-your-application/.

110. eurofins EAG Laboratories. The Power of SEM-EDS in Imaging and Elemental Analysis. [Online] [Cited: 14 May 2025.] https://www.eag.com/blog/the-power-of-sem-eds-in-imaging-and-elemental-analysis/.

111. Nanakoudis, A. EDX Analysis with SEM: How Does it Work. [Online] ThermoFisher Scientific, 28 November 2019. [Cited: 15 May 2025.] https://www.thermofisher.com/blog/materials/edx-analysis-with-sem-how-does-it-work/#:~:text=From%20searching%20for%20food%20contaminants,than%20an%20SEM%20can%20alone..

112. diamond. Tomography. [Online] [Cited: 15 May 2025.] https://www.diamond.ac.uk/Instruments/Techniques/Imaging/Tomography.html.

113. Rigaku. X-ray Computed Tomography: A Brief Introduction. [Online] [Cited: 15 May 2025.] https://rigaku.com/products/imaging-ndt/x-ray-ct/learning/x-ray-computed-tomography-brief-

introduction#:~:text=Here%20is%20the%20basic%20idea,and%20size%20of%20the%20sample..

114. ***X-ray micro-computed tomography (µCT): an emerging opportunity in parasite imaging.*** **O'Sullivan, J. B. D., et al. 7, s.l. : Cambridge University Press, 2018, Parasitology, Vol. 145, pp. 848-854.**

115. Bahadori, A. Chapter 3 - Single-Phase and Multiphase Flow in Natural Gas Production Systems. ***Natural Gas Processing.*** **2014.**

116. Resolved Analytics. What are Fluid Flow Regimes? ***An Introduction to Flow Regimes.*** **[Online] [Cited: 15 May 2025.] https://www.resolvedanalytics.com/fluid-dynamics/what-are-flow-regimes.**

117. SIMSCALE. What is Reynolds Number. [Online] [Cited: 15 May 2025.] https://www.simscale.com/docs/simwiki/numerics-background/what-is-the-reynolds-number/.

118. Bronkhorst. Laminar Flow vs Turbulent Flow. [Online] [Cited: 15 May 2025.] https://www.bronkhorst.com/knowledge-base/laminar-flow-vs-turbulent-flow/.

119. SIMSCALE. What is Turbulent Flow. [Online] [Cited: 15 May 2025.] https://www.simscale.com/docs/simwiki/cfd-computational-fluid-dynamics/what-is-turbulent-flow/.

120. Cadence CFD Solutions. Identifying the Types and Classifications of Fluid Flow Regimes. [Online] [Cited: 15 May 2025.] https://resources.system-analysis.cadence.com/blog/msa2022-identifying-the-types-and-classifications-of-fluid-flow-regimes.

121. ***Development of Gas-Solid Fluidization: Particulate and Aggregative.*** **Zhou, Y., Wang, T. and Zhu, J. 2023, Powder Technology, Vol. 421.**

122. SLB. Multiphase Fluid FLow. [Online] [Cited: 15 May 2025.] https://glossary.slb.com/en/terms/m/multiphase_fluid_flow.

123. BS EN ISO 5167-2:2022 - TC: Measurement of Fluid Flow By Means of Pressure Differential Devices Inserted in Circular Cross-Section Conduits Running Full - Orifice Plates. 2022.

124. Bomelburg, H. J. *Estimation of Gas Leak Rates Through Very Small Orifices and Channels.* s.l. : Battelle Pacific Northwest Labs, 1977.

125. *Experimental Data and Theoretical Modeling of Gas Flows Through Metal Capillary Leaks.* Tison, S. A. 1993, Vacuum, Vol. 44, pp. 1171-1175.

126. *The Flow Characteristics of Capillary Leaks.* Ochert, N. and Steckelmacher, W. 11, 1951, British Journal of Applied Physics, Vol. 2.

127. *Experimental Data and Theoretical Modeling of Gas Flows Through Metal Capillary Leaks.* Tison, S. A. 11-12, 1993, Vacuum, Vol. 44, pp. 1171-1175.

128. International Atomic Energy Agency. *IAEA-TECDOC-710: Applicability of the Leak Before Break Concept.* s.l. : IAEA, 1993.

129. *The R6 Procedure: Recent Developments nad Comparison with Alternative Approaches.* Budden, P. J., Sharples, J. K. and Dowling, A. R. 14-15, 2000, International Journal of Pressure Vessels and Piping, Vol. 77, pp. 895-903.

130. *Enhancement of Leak Rate Estimation Model for Corroded Cracked Thin Tubes.* Chang, Y. S., et al. 1, 2010, International Journal of Pressure Vessels and Piping, Vol. 87.

131. *Prediction of Failure Pressure and Leak Rate of Stress Corrosion Cracks.* Majumdar, S., et al. Toronto : s.n., 2002. 4th CNS International Steam Generator Conference.

132. *Gas Flow Through Cracks.* Button, B. L., et al. 4, 1978, Journal of Fluids Engineering, Vol. 100, pp. 453-458.

133. *Air Flow Through Cracks.* Baker, P. H., Sharples, S. and Ward, I. C. 4, 1987, Building and Environment, Vol. 22, pp. 293-304.

134. *Leakage Rates Through Complex Crack Paths Using an ODE Method.* Gill, P., Sharples, J. and Budden, P. Boston, MA : s.n., 2015. Pressure Vessels and Piping Conference. Vol. 6A: Materials and Fabrication.

135. *Explicit Equations for Leak Rates Through Narrow Cracks.* Beck, S. B. M., Bagshaw, N. M. and Yates, J. R. 7, 2005, International Journal of Pressure Vessels and Piping, Vol. 82.

136. ***Leak Before Break: Studies in Support of New R6 Guidance on Leak Rate Evaluation.*** **Taggart, J. P. and Budden, P. J. 1, 2008, Journal of Pressure Vessel Technology, Vol. 130.**

137. ***Air Flow Through Cracks.*** **Baker, P. H., Sharples, S. and Ward, I. C. 4, 1987, Building and Environment, Vol. 22, pp. 293-304.**

138. ***Gas Flow in a Long Microchannel.*** **Hsieh, S-S., et al. 17-18, 2004, International Journal of Heat and Mass Transfer, Vol. 47, pp. 3877-2887.**

139. LibreTexts Chemistry. 9.3.2: Boiling, Evaporation and Condensation. [Online] [Cited: 16 May 2025.] https://chem.libretexts.org/Courses/Madera_Community_College/MacArthur_Chemistry_3A_v_1.2/09%3A_Attractive_Forces/9.03%3A_Phase_Transitions/9.3.02%3A_Boiling_Evaporation_and_Condensation.

140. The Engineering ToolBox. Water- Boiling Points at Vacuum Pressure. [Online] [Cited: 16 May 2025.] https://www.engineeringtoolbox.com/water-evacuation-pressure-temperature-d_1686.html?vA=100&units=B#.

141. Thyssenkrupp. What is the Difference Between 316 and 304 . [Online] [Cited: 14 May 2025.] https://www.thyssenkrupp-materials.co.uk/the-difference-between-stainless-steel-304-and-316.html.

142. TWI. What is Shot Peening and How Does it Work. [Online] [Cited: 14 May 2025.] https://www.twi-global.com/technical-knowledge/faqs/what-is-shot-peening.

143. ***Can the Drop Evaporation Test Evaluate the Stress Corrosion Cracking Susceptibility of the Welded Joints of Duplex and Super Duplex Stainless Steels.*** **Pereira, H. B. and Azevedo, C. R. F. 2019, Engineering Failure Analysis, Vol. 99, pp. 235-247.**

144. Prior, A. ***Determination of an Optimum Method to Simulate Stress Corrosion Cracking of AGR Fuel Stainless Steel Cladding.*** **s.l. : University of Leeds, 2023.**

145. ***Research on the Improvement of Concrete Autogenous Self-Healing Based on the Regulation of Cement Particle Size Distribution (PSD).*** **Yuan, L., et al. 2019, Materials.**

146. ***SCC of 2304 Duplex Stainless Steel - Microstructure, Residual Stress and Surface Grinding Effects.*** **Zhou, N., et al. 2017, Materials, Vol. 10.**

147. ***Assessment of Circumferential Cracks in Hypereutectic Al-Si Clutch Housings.*** **Haghshenas, M. and Jamali, J. 2017, Case Studies in Engineering Failure Analysis, Vol. 8, pp. 11-20.**

148. ***In-Situ SEM Observations of Tensile Deformation of the Lamellar Microstructure in TC21 Titanium Alloy.*** **Shao, H., et al. 559, Materials Science and Engineering: A, Vol. 2013, pp. 515-519.**

149. ***In Situ Scanning Electron Microscope (SEM) Observations of Damage and Crack Growth of Shale.*** **Cui, Z. and Han, W. 2, 2018, Microscopy and Microanalysis, Vol. 24, pp. 107-115.**

150. ***An Investigation of Cracking Causes in an Outlet RTJ Flange in ISOMAX Unit.*** **Delavar, A. N., Shayegani, M. and Pasha, A. 2, 2013, Case Studies in Engineering Failure Analysis, Vol. 1, pp. 61-66.**

151. ***Effect of Low-Temperature Surface Carburization on Stress Corrosion Cracking of AISI 304 Stainless Steel.*** **Peng, Y., et al. 2017, Surface and Costings Technology, Vol. 328, pp. 420-427.**

152. ***Microstructure and Creep Properties of Ni-Base Superalloy IN718 Built up by Selective Laser Melting in a Vacuum Environment.*** **Nagahari, T., et al. 2020, Metals, Vol. 10.**

153. ***On the Mechanistic Difference Between In-Phase and Out-Of-Phase Thermo-Mechnaical Fatigue Crack Growth.*** **Norman, V., et al. 2020, International Journal of Fatigue, Vol. 135.**

154. Edmund Optics. Precision Pinholes. [Online] [Cited: 15 May 2025.] https://www.edmundoptics.co.uk/f/precision-pinholes/12073/.

155. —. Precision Air Slits. [Online] [Cited: 15 May 2025.] https://www.edmundoptics.co.uk/f/precision-air-slits/12136/.

156. ***Drying of Wet Stored Spent Zirconium Fuel Cladding Simulant.*** **Jackson, M. and Hanson, B. 2018.**

157. Lovett, M. ***Vacuum Drying Rig for Use on Spent Nuclear Fuel.*** **s.l. : University of Leeds, 2023.**

158. ***A Global Model for Predicting Vacuum Drying of Used Nuclear Fuel Assemblies.*** **Saha, S., et al. 3, 2020, Nuclear Technology, Vol. 208.**

159. ***P. J. Budden; J. K. Sharples; A. R. Dowling.*** **Approaches, The R6 Procedure: Recent Developments and Comparison with Alternative. 14-15, 2000, International Journal of Pressure Vessels and Piping, Vol. 77, pp. 895-903.**

160. The Engineering Toolbox. Vacuum - Evacuation Time. [Online] 2005. [Cited: 31 May 2025.] https://www.engineeringtoolbox.com/vacuum-evacuation-time-d_844.html.

161. ***The Status of Spent Fuel Storage in the UK.*** **Dunn, M. J. and Topliss, I. R. Vienna (Austria) : s.n., 1998. International Symposium on Storage of Spent Fuel from Power Rreactors. pp. 153-156.**

162. Westinghouse. Advanced Gas-cooled Reactors. [Online] [Cited: 21 March 2025.] https://westinghousenuclear.com/uknuclear/products-services/advanced-gas-cooled-reactors/.

163. Keane, K. Lifespan of four nuclear power stations extended. [Online] BBC, 03 December 2024. [Cited: 21 March 2025.] https://www.bbc.co.uk/news/articles/c33dvekx021o.

164. International Atomic Energy Agency (IAEA). Water Cooled Reactors. [Online] IAEA. [Cited: 21 March 2025.] https://www.iaea.org/topics/water-cooled-reactors.

165. Vickers, J. A. ***Development of a Pre-Treatment process for Magnesium & Magnox Wastes.*** **Leeds : The University of Leeds, 2022.**

166. Gov.UK. What is Thorp? [Online] 25 September 2024. [Cited: 22 March 2025.] https://www.gov.uk/government/case-studies/what-is-thorp.

167. Nuclear Waste Services. ***WPS/240/02: Waste Package Specification and Guidance Documentation: Specification for High Heat Generating Waste Precursor Product.*** **s.l. : Nuclear Waste Services, 2024.**

168. International Standards Organisation. ***ISO 15324:2000 Corrosion of Metals and Alloys - Evaluation of Stress Corrosion Cracking by the Drop Evaporation Test.*** **2000.**

169. ***Threshold Temperature for Stress Corrosion Cracking of Duplex Stainless Steel Under Evaporative Seawater Conditions.*** **Hinds, G. and Turnbull, A. 2, 2008, Corrosion, Vol. 64, pp. 101-106.**

170. ***Assessment of Susceptibility to Chloride Stress Corrosion Cracking of Highly Alloyed Stainless Steels. Part II: A New Immersion Test Method.*** **Drugli, J. M. and Steinsmo, U. 1997, NACE Corrosion.**

171. International Atomic Energy Agency. ***IAEA-TECDOC-944: Further Analysis of Extended Storage of Spent Fuel.*** **Vienna : IAEA, 1997.**

172. Bakirov, M., et al. ***Application Of The "Leak Before Break" Concept On Npp Units of the First Generation with WWER-440 Reactors. Involvement of Leak Detection Systems Considering New Elaborated Approaches.*** **s.l. : IAEA. IAEA-CN-155-033P.**

173. ***Code development and characteristics analysis for Leak Before Break in the pipelines of Sodium-cooled Fast Reactor.*** **Wu, D., et al. 2019, Annals of Nuclear Energy, Vol. 133, pp. 777-794.**

174. Gill, P. ***Investigating Leak Rates for "Leak-before-Break" Assessments.*** **s.l. : University of Manchester, 2014.**